

# Leak Detection for Waterproof Enclosures using Schlieren Optics

Tony Mackenzie

A thesis submitted to Auckland University of Technology in partial  
fulfilment of the requirements for the degree of

Masters of Engineering (ME)

2018

School of Engineering

Primary Supervisor: Dr Michael Gschwendtner

Secondary supervisor: Dr Andrew Lowe

## Abstract

In the search for a method of detecting leak location without danger of damaging the product tested or harming the user, Navico approached Auckland University of Technology (AUT) with the proposition of developing a visual method to detect leaks.

Schlieren optics showed promise when a tracer gas with a different refractive index is used. Helium was chosen for its inertness as well as small molecule size for leak penetration.

A double pass Schlieren optical assembly was built, development of the optical assembly iteratively increased the sensitivity to small leaks until a leak that would pass Navico's production test criteria could be seen.

Once small leaks could be seen the next stage in the development of the Schlieren optical assembly was increasing the range of leak sizes that could be viewed, with the optical assembly tuned to smaller leaks, it caused larger leaks to be less visible.

Automation of the knife edge adjustment allowed for photos with different cut-off amounts and orientations to be captured. These photos were then combined on a computer giving an image with sensitivity to a full range of leak sizes. Full automation was achieved by computer control of the camera, knife edge and a rotating product table that allowed multiple view orientations.

Finally, artificial intelligence was used to increase the ease of detection by inexperienced users, region detection neural networks and Semantic Segmentation networks showed good success at identifying and highlighting leaks from video taken from the Schlieren optical assembly.

# Table of Contents

|       |   |    |
|-------|---|----|
| 1     | Introduction .....  | 1  |
| 1.1   | Current Techniques Employed by Navico .....                       | 2  |
| 1.2   | Project Objectives.....   | 3  |
| 2     | Literature Survey.....  | 4  |
| 2.1   | Refractive Indexes Methods.....                                   | 4  |
| 2.1.1 | Direct Shadowgraph.....   | 4  |
| 2.1.2 | Schlieren Optics.....   | 5  |
| 2.1.3 | Interferometry .....  | 12 |
| 2.2   | Colour Methods.....   | 15 |
| 2.2.1 | Infrared Imaging.....   | 15 |
| 2.3   | Non-visual Methods - Ultrasonic Leak Detection.....               | 19 |
| 2.3.1 | Passive Ultrasound Leak Detection.....                            | 19 |
| 2.3.2 | Active Ultrasound Leak Detection .....                            | 19 |
| 2.4   | Summary of Leak Detection Methods.....                            | 20 |
| 2.4.1 | Interferometry .....  | 20 |
| 2.4.2 | Infrared imaging.....   | 20 |
| 2.4.3 | Schlieren Optics.....   | 21 |
| 2.4.4 | Chosen method .....   | 21 |
| 2.5   | Image Processing.....   | 22 |
| 2.5.1 | Contrast Adjustment.....  | 22 |
| 2.6   | Computer Vision .....   | 23 |
| 2.6.1 | Convolutional Neural Networks.....                                | 24 |
| 2.6.2 | Classification with Convolutional Neural Networks.....            | 26 |
| 2.6.3 | Region-Based Convolutional Networks.....                          | 26 |
| 2.6.4 | Stochastic Gradient Descent with Momentum .....                   | 27 |
| 2.6.5 | Training Options and their effect on Network training .....       | 27 |
| 2.6.6 | Pre-trained networks .....  | 28 |
| 3     | MATLAB Raytracing of Schlieren Optics.....                        | 30 |
| 3.1   | 2D Ray Tracing .....  | 30 |
| 3.2   | 3D Ray Tracing .....  | 32 |
| 3.3   | Lessons in Schlieren Optics from Basic 3D Ray Tracing.....        | 35 |
| 4     | Development of Schlieren Optical Setup for Leak Detection .....   | 38 |
| 4.1   | AUT's Existing Schlieren Optical Setup.....                       | 41 |
| 4.2   | Double Pass Schlieren Optics .....                                | 42 |
| 4.3   | Initial Improvements to the Existing Schlieren Optical Setup..... | 42 |

|        |   |     |
|--------|---|-----|
| 4.3.1  | White Light Source for Colour Schlieren .....                         | 44  |
| 4.3.2  | Knife Edge.....   | 47  |
| 4.3.3  | Beam Splitter.....  | 49  |
| 4.3.4  | Colour Schlieren .....  | 50  |
| 4.4    | Refining the Schlieren Optical Setup for Leak Detection .....         | 55  |
| 4.4.1  | Finding the Appropriate Lens for the Schlieren Optical Assembly ..... | 55  |
| 4.4.2  | Automating the Knife edge and Remote Camera Shutter.....              | 57  |
| 4.4.3  | Rotating Platform.....  | 59  |
| 4.4.4  | Lens .....  | 62  |
| 4.4.5  | Light Source.....   | 63  |
| 4.4.6  | Optical Base.....   | 65  |
| 4.4.7  | Light Trap.....   | 71  |
| 4.4.8  | Mirror Base.....  | 72  |
| 4.4.9  | High Sensitivity Range imaging (HSR) .....                            | 73  |
| 4.4.10 | Overview of Improved Optical Assembly Operation .....                 | 77  |
| 5      | Testing of Schlieren optics to locate leaks on a Navico product ..... | 78  |
| 5.1    | Improved Schlieren Optical Assembly.....                              | 81  |
| 5.1.1  | Sensitivity to Leak 3.....  | 83  |
| 6      | Image Processing.....   | 84  |
| 6.1    | Adobe Lightroom Creative Cloud .....                                  | 84  |
| 6.2    | MATLAB .....  | 87  |
| 6.3    | Local contrast .....  | 87  |
| 7      | Computer Vision.....  | 89  |
| 7.1.1  | Region-Based Convolutional Networks.....                              | 89  |
| 7.2    | Semantic Segmentation Convolutional Networks .....                    | 90  |
| 7.2.1  | Training Networks for Semantic Segmentation.....                      | 90  |
| 7.3    | Performance of Computer Vision.....                                   | 92  |
| 7.3.1  | Accuracy .....  | 92  |
| 7.3.2  | Speed.....  | 96  |
| 8      | Conclusion .....  | 98  |
| 9      | Future work.....  | 100 |
| 9.1    | Upscaling the optical assembly for use with bigger products .....     | 100 |
| 9.2    | Feasibility and cost .....  | 100 |
| 10     | Appendices.....   | 101 |
| 11     | References.....   | 125 |



## Table of Figures

|   |    |
|---|----|
| Figure 1 - Direct Shadowgraph(Settles, 2001, p. 30) .....   | 5  |
| Figure 2 - The Foucault knife-edge mirror test. ....  | 5  |
| Figure 3 - Toepler's single-field-lens Schlieren arrangement (Settles, 2001, p. 41).....  | 6  |
| Figure 4 - Dual field lens Schlieren arrangement (Settles, 2001, p. 33) .....   | 6  |
| Figure 5 - Z-type Schlieren arrangement(Settles, 2001, p. 42) .....   | 7  |
| Figure 6 - Double-pass Schlieren arrangement (Settles, 2001, p. 47) .....   | 7  |
| Figure 7 - Off axis single mirror assembly (Settles, 2001, p. 48).....  | 8  |
| Figure 8 - Lens and Grid technique (Settles, 2001, p. 89).....  | 9  |
| Figure 9- The effect of cut-off on sensitivity.....   | 10 |
| Figure 10 - Rayleigh Interferometer (Hariharan, 2007) .....   | 13 |
| Figure 11 - Michelson interferometer (Hariharan, 2007) .....  | 14 |
| Figure 12 - Mach-Zehnder Interferometer (Hariharan, 2007) .....   | 14 |
| Figure 13 - Schematic of the improved point diffraction interferometer (Bachalo & Houser, 1985).....                                      | 15 |
| Figure 14 - Camera Sensor Absolute Quantum Efficiency Versus Wavelength (National Instruments, 2017).....                                 | 17 |
| Figure 15 - Transmittance of Atmosphere Over 1 NM Sea Level Path (Infrared Region) (Naval Air Warfare Center Weapons Division, 2013)..... | 18 |
| Figure 16- light absorption of gases between 100 nm and 1000nm (Gordon et al., 2017) .....  | 19 |
| Figure 17 - Contrast Adjustment: Original Image (left), Contrast Adjustment (Right) ...   | 23 |
| Figure 18- ImageNet Top-5 Classification Error Over Time(Shawn & Christiaan, 2017). .....   | 24 |
| Figure 19 - The Input Layer .....   | 25 |
| Figure 20 -The ReLU Layer.....  | 25 |
| Figure 21 - The Pooling Layer .....   | 26 |
| Figure 22 Edmund Optics Z-type Schlieren assembly (Edmund Optics Inc, 2017) .....   | 30 |
| Figure 23 - Comparing spherical and parabolic mirrors for focusing collimated light ...   | 31 |
| Figure 24 - Comparing Spherical and Parabolic mirrors for focusing diverging light from a point .....                                     | 32 |
| Figure 25 – The two STL files used for testing the 3D ray tracing program.....  | 32 |
| Figure 26 - Star STL file with a 10mm radius cut-off shifted up 1mm (right) and down 1mm (left).....                                      | 33 |
| Figure 27 - Star STL file with a 10mm radius shifted up 0.5 mm(left) and shifted up 1.5 mm (right) .....                                  | 34 |
| Figure 28 - Star STL file with extended light source with a 5mm radius(left) 10mm radius(right).....                                      | 34 |
| Figure 29 - Testing the light source pin-hole (right) and without (left) .....  | 35 |
| Figure 30 - Light from the point light source hitting the mirror with a very low number of rays.....                                      | 35 |
| Figure 31 - Internal refraction inside a chamfered octagon .....  | 36 |
| Figure 32 - First pass of light rays traveling through the test section and hitting the mirror .....                                      | 36 |
| Figure 33 - Returning rays passing cut-off, the diverging rays are removed but the unaffected rays in orange pass by .....                | 37 |
| Figure 34 – Double Pass (left) compared to Z-Type (right) showing isobutane gas escaping from a lighter .....                             | 38 |

|  |    |
|--|----|
| Figure 35 - 60" Focal Length, 6" Schlieren System (Edmund Optics Inc, 2017)  | 41 |
| Figure 36 - Solidworks rendering of the supplied knife edge  | 41 |
| Figure 37 - Green Light source with pinhole  | 43 |
| Figure 38 - Comparison of Extended and Point Light Sources   | 44 |
| Figure 39 – Using a diffuser on the light source before (left) after (right)   | 45 |
| Figure 40 - Rendering of the LED stand and heat sink   | 46 |
| Figure 41 - 3D-printed round dissection filter   | 46 |
| Figure 42- Blunt Knife Edge  | 47 |
| Figure 43- Sharp Knife Edge  | 47 |
| Figure 44 - Rendering of 3D printed knife edge stand   | 48 |
| Figure 45- Blade mounted in the stand at 45 degrees  | 49 |
| Figure 46 - beam splitter and 3D printed stand   | 50 |
| Figure 47 - Colour filter on light source  | 51 |
| Figure 48 - Lighting a small spirit burner and then blowing it out imaged using double pass Schlieren with colour filter                   | 51 |
| Figure 49- Adjusting the three colours for the Round Dissection filter   | 52 |
| Figure 50 - Methylated spirits evaporating from a small container  | 52 |
| Figure 51 - Colour Schlieren cut-off: the three colours need individual adjustment   | 53 |
| Figure 52 - Leaks with Colour Schlieren with different adjustments of cut-off  | 54 |
| Figure 53 - Leak 4 & 5 with Monochrome Schlieren (right) show much clearer results than colour Schlieren (left)                            | 54 |
| Figure 54 - Image taken with the Soligor 135mm   | 55 |
| Figure 55- Crop from the Sony 70-200 mm shot at 151 mm showing blue fringing   | 57 |
| Figure 56 - Solidworks rendering of the DVD drive sliding assembly   | 58 |
| Figure 57 - User interface for control of the rotating base and camera   | 59 |
| Figure 58 - Arduino Mega and Adafruit Motor Driver wiring  | 60 |
| Figure 59 - Equation-driven sketch of the belt and pulleys   | 61 |
| Figure 60 - Rotating Platform Design 1 top view  | 61 |
| Figure 61 - Solidworks rendering of the rotating base with the multi-function display in portrait orientation                              | 62 |
| Figure 62 - Comparison on the field of view of the Opteka 420-800mm at 450 mm (left) and the Soligor 135 mm (right)                        | 63 |
| Figure 63 - Effect of the blue translucent LED stand on the Schlieren image produced   | 64 |
| Figure 64 - White ABS LED stand with black tape sealing light leaks  | 65 |
| Figure 65 - Approximate size requirements for base and approximate rail path (dotted lines)  | 66 |
| Figure 66- Edmund Optics 13 mm thick aluminium breadboard (left) (Edmund Optics, 2017b), Newport 25 mm breadboard (right) (Newport, 2017b) | 67 |
| Figure 67 - Edmund Optics Dovetail Optical Rail (Left) (Edmund Optics, 2017a), Newport Optical Rail(right) (Newport, 2017a)                | 67 |
| Figure 68 - Concept one, using pipe for optical rails  | 68 |
| Figure 69 - Solidworks rendering of T-Slot   | 69 |
| Figure 70 - Base Made with 4040 prototyping extrusion  | 70 |
| Figure 71 - OnEquip 40 x 160 SlotPro base with 40 x 80 corner brackets   | 70 |
| Figure 72 - A fraction of light hitting the beam splitter will be reflected the wrong way (small red arrow)                                | 71 |
| Figure 73 - Light reflecting deeper into the light trap  | 71 |
| Figure 74 - With light trap (left) without light trap (right)  | 72 |
| Figure 75 - Spring loaded adjustment knobs   | 73 |

|  |    |
|--|----|
| Figure 76 – Original mirror stand (left) Improved mirror stand with 3 contact points (right).....                    | 73 |
| Figure 77 - MATLAB GUI for High Sensitivity Range imaging.....   | 75 |
| Figure 78 - Movement of the two knife edges. Note a pinhole was normally used in front of the light source lens..... | 75 |
| Figure 79 - Overview of Optical Components.....  | 77 |
| Figure 80 - Test product held in rotating base.....  | 78 |
| Figure 81- Leak 3 .....  | 79 |
| Figure 82 - Vacuum testing production criteria .....   | 79 |
| Figure 83 - Vacuum testing at R&D criteria .....   | 80 |
| Figure 84 - All leaks uncovered, beam splitter is not used and knife edge is at 45 degrees.....                      | 81 |
| Figure 85 - Double Pass with Soligor 135 mm (note each leak is seen twice due to the lack of a beam splitter).....   | 81 |
| Figure 86 - Colour Schlieren with small disturbances.....  | 82 |
| Figure 87- Double Pass with Sony 70-200 mm lens and beam Splitter .....  | 82 |
| Figure 88 - Leak 3 (Left) Leak 4 & 5 (Right) .....   | 83 |
| Figure 89 - Leak 3 detected (left) Leak 3 is no longer detectable with Leak 4 & 5 uncovered (right) .....            | 83 |
| Figure 90 - low sensitivity image of a leak before Lightroom adjustment .....  | 85 |
| Figure 91 - Near full cut off .....  | 85 |
| Figure 92 - low sensitivity image of a leak after basic Lightroom adjustment .....                                   | 86 |
| Figure 93 - low sensitivity image of a leak after basic and tone curve Lightroom adjustment .....                    | 86 |
| Figure 94 - MATLAB Contrast adjustment using localcontrast () with an edge threshold of 0.4 and an amount of 1.....  | 87 |
| Figure 95 - Large Region Proposed by An RCNN that contains 2 leaks.....  | 90 |
| Figure 96 - Pixel labelling training data for Semantic Segmentation.....   | 91 |
| Figure 97 – Average Precision for VGG19 over 15 epochs with different learn rates....                                | 93 |
| Figure 98 - Test and Training Accuracy for VGG19 over 100 epochs.....  | 93 |
| Figure 99 - Results from the best performing network .....   | 95 |
| Figure 100 - Hybrid Regional + Semantic Segmentation .....   | 97 |

## List of Abbreviations

|                |   |
|----------------|---|
| <b>ABS</b>     | Acrylonitrile Butadiene Styrene               |
| <b>AP</b>      | Average Precision                             |
| <b>ARW</b>     | Sony Alpha Raw                                |
| <b>AUD</b>     | Australian Dollar                             |
| <b>AUT</b>     | Auckland University of Technology             |
| <b>B&amp;G</b> | Brookes and Gatehouse                         |
| <b>CCD</b>     | Charge-coupled device                         |
| <b>CMOS</b>    | Complementary metal oxide semiconductor       |
| <b>COB</b>     | Chip on board                                 |
| <b>CPU</b>     | Central Processing Unit                       |
| <b>DVD</b>     | Digital Versatile Disc                        |
| <b>FDM</b>     | Fused Deposition Modelling                    |
| <b>FE</b>      | Full Frame E-Mount                            |
| <b>FLIR</b>    | Forward Looking Infrared Systems              |
| <b>GB</b>      | Gigabyte                                      |
| <b>GPU</b>     | Graphics Processing Unit                      |
| <b>HD</b>      | High definition                               |
| <b>HSR</b>     | High Sensitivity Range                        |
| <b>LED</b>     | Light emitting diode                          |
| <b>LPG</b>     | Liquid Petroleum Gas                          |
| <b>NEMA</b>    | National Electrical Manufacturers Association |
| <b>PETG</b>    | Polyethylene Terephthalate                    |
| <b>ReLU</b>    | Rectified linear unit                         |
| <b>RCNN</b>    | Region-Based Convolutional Neural Network     |
| <b>RGB</b>     | Red Green Blue Colour Model                   |
| <b>STL</b>     | Standard Triangle Language                    |
| <b>USD</b>     | United States Dollar                          |
| <b>VGG</b>     | Visual Geometry Group                         |

## Attestation of Authorship

I hereby declare that this submission is my own work and that, to the best of my knowledge and belief, it contains no material previously published or written by another person, nor material which to a substantial extent has been submitted for the award of any other degree or diploma of a university or other institution of higher learning.

Tony Mackenzie

Signature:

Date:

6/6/2018

## Acknowledgements

I would like to express my sincere gratitude to Dr Michael Gschwendtner and Dr Andrew Lowe for their guidance throughout this project.

Callaghan Innovation and Navico for a R&D Student-Fellowship Grant.

Thank you to my parents Paul and Jo Mackenzie for inspiring me to embark on higher education.

I would also like to thank my partner Danielle Yang for her support.

# 1 Introduction

Navico is the world's biggest leisure marine electronics producer, created in 2006 from the merger of Simrad Yachting and Lowrance Electronics. Navico offers many different types of marine electronics devices in their product range under the brands of Simrad for powerboat owners, Lowrance for fishing, and B&G for sailing. The devices under these brands are made to be used in a marine environment so they are designed and tested to be waterproof to the IPX7 standard.

To test water-tightness, Navico uses a vacuum decay test to determine if a product will leak during IPX7 testing; while this works well for a pass or fail it gives no indication of the leak location. Navico performs testing for location by submersion in a bucket of water; location is indicated by air bubbles escaping the product when pressurised air is applied to the product internally via the purge plug.

Submersion of expensive electronics into water is obviously not ideal when any water ingress into the product can destroy the sensitive electronics within. Navico has previously tested gas sniffing equipment to find leaks when acetylene gas was injected into the product but decided against it due to safety concerns over flammability and toxicity.

In the search for a method of detecting leak location without danger of damaging the product tested or harming the user, Navico approached Auckland University of Technology (AUT) with the proposition of developing a visual method that is easy to use while still being sensitive enough to find leaks that would cause a product to fail Navico's vacuum decay leak test.

The proposed direction for this project was to explore two different detection methods, the first being the use of optical systems that detect changes in refractive index and the second being the use of different spectrum imaging techniques such as infrared to detect a trace gas.

By pressurising the test product with a tracer gas with a different refractive index to that of the surrounding air, it was proposed leaks could be detected using Schlieren Optics.

Helium gas was chosen because of its inertness and small molecule size, giving it the ability to easily penetrate leaks.

## 1.1 Current Techniques Employed by Navico

Electronic marine devices produced by Navico come with IPX7 waterproof rating, meaning that they must be able to withstand submersion in water 1 m deep for up to 30 minutes.

The first approach used by Navico to test the seals on a waterproof enclosure is to pull a vacuum on the product; a higher vacuum is used for R&D testing, and a slightly lower one for production tests. The pressure difference simulates the force on the product's seals caused by submersion into water 1 m deep.

The decay in internal vacuum caused by leaks is measured over time using a high accuracy pressure gauge; if the vacuum decay stays above a specified target gradient, the product passes. While this approach is fast at diagnosing if a product is leaking, it gives no indication of the location of the leak if one occurs.

Diagnosing the location in which leaks occur is especially important feedback for the mechanical design team so that they can improve product seal design for later models of the products. In the case that an enclosure develops a leak during testing, the next step Navico takes in finding the leak location is to pressurize the enclosure and submerge it in coloured water. Bubbles emitted by the seals are used to find the location of the leak. While this method is adequate for some leaks, small leaks are very difficult to detect and larger leaks allow water into the enclosure, destroying the expensive internal electronic components.



## 1.2 Project Objectives

This project aims to find a visual method to locate leaks so that the products can be used for further testing after being tested for water tightness, ideally the method should have the following qualities.

- Easy to use with little training.
- Cost-effective: the method should not cost more than \$10,000 to implement.
- Sensitive: able to detect leaks that would cause a product to fail.
- Safe: the method should not put the user at significant risk of harm.

## 2 Literature Survey

There are two types of leak detection methods covered in this literature review, the first type is visual methods that use a change in refractive index due to density changes, the second is changes of colour due to a different gas.

To detect leaks visually, a tracer gas is generally used to give a visual clue to where the leak occurs. There are two ways to detect this tracer gas: the first way is using a gas with a different refractive index to the surrounding environment so that a method of detecting inhomogeneous refractive indexes can be employed such as Schlieren optics or interferometry. The second way is by using a gas with a different colour (in the visible range or in the infrared range) and then using a camera sensitive to the range that its visible in to detect it.

Historically, there has also been the use of an acoustic method, this employs a speaker to emit an ultrasonic tracer noise from inside the product. This can then be detected and converted to the audible range by a special microphone.

All of the above-mentioned techniques are traditionally hard to use, because of this Image Processing and Artificial Intelligence are also covered in the search of a way to better identify leaks that an untrained user might miss.

### 2.1 Refractive Indexes Methods

#### 2.1.1 Direct Shadowgraph

A direct shadowgraph is the simplest way of seeing the differences in refractive indexes in an inhomogeneous media. This was first described by Robert Hooke (famous for his study in elasticity) when he noticed stars viewed through his telescope distorted in a fluctuating motion near the horizon. He later went on to conduct experiments viewing a small round light source through mixtures of fresh water and brine as well as different clear liquors (Hooke, 1665).

When a single light source is used, parallel light from the source travels at a slightly different angle,  $\epsilon$ , through a medium when it encounters areas with density changes that cause a difference in refractive indexes shown as S, in Figure 1. The beams of light

that get refracted at a different angle cause areas of shadow and higher illumination on the viewing screen,  $\Delta\alpha$  (Settles, 2001).

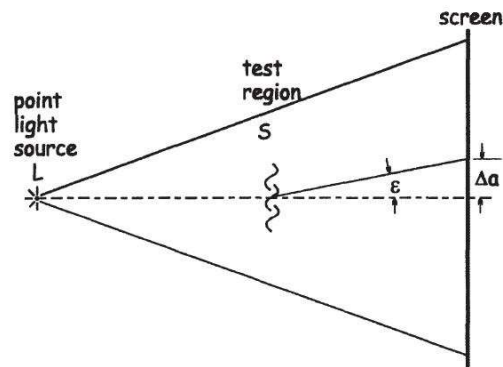


Figure 1 - Direct Shadowgraph(Settles, 2001, p. 30)

### 2.1.2 Schlieren Optics

The difference between a shadowgraph and Schlieren optics is the inclusion of a knife edge to partially cut off some of the light to increase the sensitivity and contrast of the image. The use of a knife edge was first documented by Jean Bernard Léon Foucault for testing of the optical mirrors used in telescopes. This method is shown in Figure 2 where the user checks the pattern made by the illuminated mirror. Even though Foucault never noticed the effect his knife edge had on Schlieren methods, many still refer to the knife edge as 'Foucault's knife' (Settles, 2001).

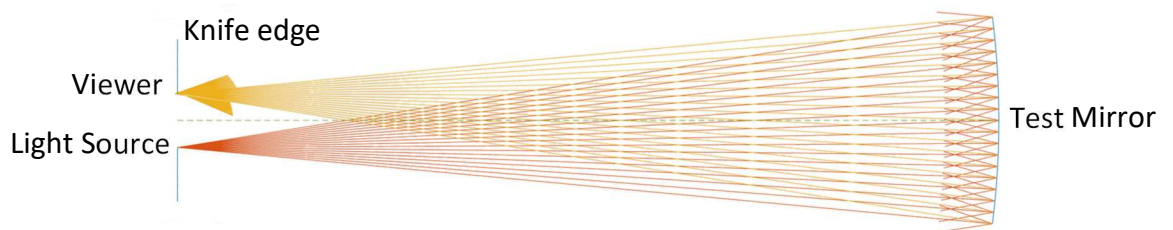


Figure 2 - The Foucault knife-edge mirror test.

### Single Field Lens Schlieren Assembly

Toepler's single field lens assembly is widely considered to be the first Schlieren apparatus. It uses a single lens to focus diverging light from a point source through a test section onto a focal point at the knife edge, and then onto a camera, as shown in Figure 3. Toepler used this to become the first person to visualise shock waves that he created using a spark (p. Krehl & Engemann, 1995).

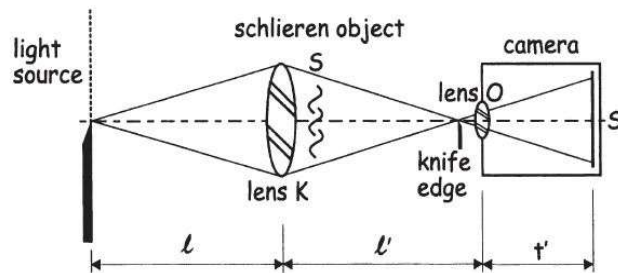


Figure 3 - Toepler's single-field-lens Schlieren arrangement (Settles, 2001, p. 41)

### Dual Field Lens Schlieren Assembly

The dual field lens Schlieren assembly is very similar to Toepler's original Schlieren assembly. However, it uses two lenses so that the light traveling through the test section is parallel. This helps by keeping everything within the area of parallel light at the same magnification and focus. The dual lens Schlieren assembly also uses a condenser lens on the light source to focus the light into a more intense beam. Apart from these two changes, the layout of the dual field lens Schlieren assembly in Figure 4 is essentially the same as the single field lens arrangement in Figure 3.

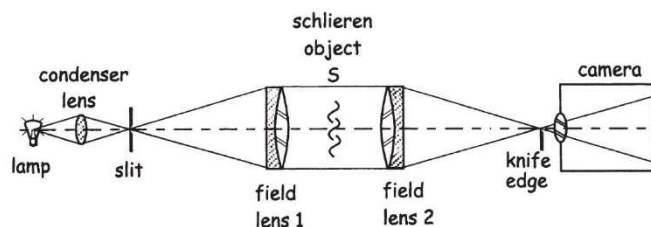


Figure 4 - Dual field lens Schlieren arrangement (Settles, 2001, p. 33)

### Z-Type Schlieren Assembly

The Z- type Schlieren assembly is one of the most common Schlieren arrangements used, because it can be easily constructed from two parabolic telescope mirrors. These are more commonly available and come in larger sizes than spherical mirrors due to the demand from astronomy for ever bigger telescopes. If common symmetrical parabolic mirrors are used, they suffer from off-axis aberrations (Settles, 2001, p. 42). Most of the off-axis aberrations are cancelled out by having the camera and light source on opposite sides in a Z-shaped layout, such as in **Figure 5**.

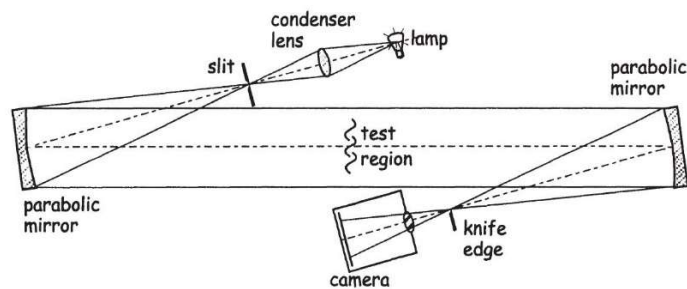


Figure 5 - Z-type Schlieren arrangement(Settles, 2001, p. 42)

### Single Mirror Coincident Schlieren Assembly

The single mirror coincident or double pass system uses one spherical mirror in the layout shown in **Figure 6**. In appearance, the layout is very similar to Foucault's knife edge test. Ideally, both the light source and camera are on-axis by use of a beam splitter. This system has the advantage of double the sensitivity, because the light passes the test area twice (Settles, 2001, p. 46). Only requiring one mirror also has cost benefits.

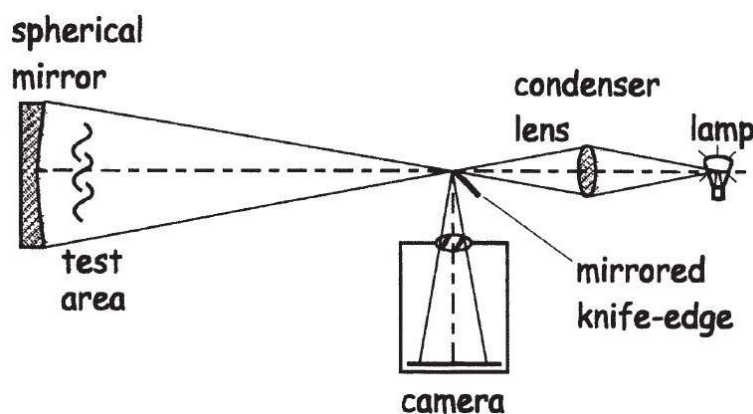


Figure 6 - Double-pass Schlieren arrangement (Settles, 2001, p. 47)

### Off Axis Single Mirror Schlieren Assembly

The off-axis single mirror Schlieren assembly has the light source and camera offset from the mirror's axis as demonstrated in Figure 7.

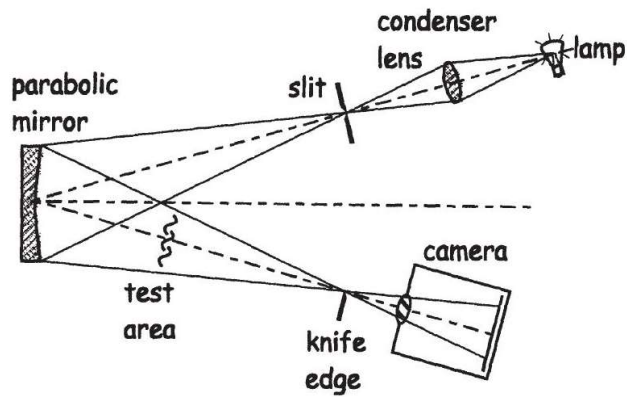


Figure 7 - Off axis single mirror assembly (Settles, 2001, p. 48)

The Off-Axis Single Mirror Schlieren Assembly has the same advantages as the coincident one. However, if the test section is too close to the mirror, image ghosting occurs due to the way that the light deflects from the mirror at an angle. It also encounters the same off-axis aberrations as the Z-type, but worse, because the equal and opposite offset angle of the Z-type cancel some aberrations (Settles, 2001, p. 48).

### Schardin's Background-Grid-Distortion Schlieren Method

Schardin proposed a range of different methods for Schlieren photography. One of the most notable of these he named Schlieren Method Number 4 (Schardin, 1942). Method Number 4 uses an illuminated source grid and a matching cut-off grid as seen in Figure 8. This eliminates the need for a mirror. When the source grid and cut-off grid are correctly positioned, they cancel out unaffected light traveling to the image plane from the illumination source. Light refracted by disturbances in the test area is able to be viewed because it passes the cut-off grid.

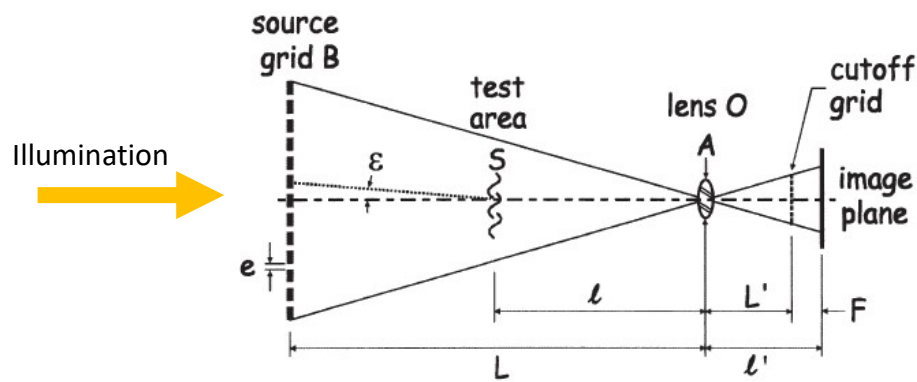


Figure 8 - Lens and Grid technique (Settles, 2001, p. 89)

### Zebra Schlieren

Peale and Summers revisited Schlieren Method Number 4 in 1996. Inspired by the simplicity of the source and cut-off grids, they developed a similar method to allow for larger objects to be leak-tested naming the method as Zebra Schlieren. They noted that the technique can be scaled to much larger sizes than traditional Schlieren optics without a significant increase in cost. Unfortunately, this technique is unable to compete with the sensitivity of other traditional Schlieren methods that use a mirror (E Peale & L Summers, 1996).

### Colour Schlieren Imaging

Since the human eye is more sensitive to changes in colour rather than illumination intensity, there has always been an incentive to change Schlieren systems from a monochrome to a colour system (Ben-Dor, Igra, & Elperin, 2001; P. O. K. Krehl, 2009). The simplest form of this exists by swapping out the knife edge used in traditional Schlieren methods with a set of coloured filters (Settles, 2001).

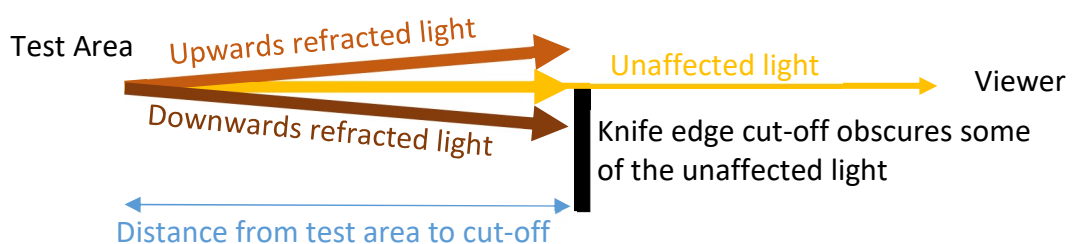
Many consider the origin of colour Schlieren as the ring lattice developed by Julius H. Rheinberg for use with his microscope for creating colour contrast between different parts of a transparent object. Several incarnations of the colour Schlieren system have been developed, originally using a filter at the cut-off as Schardin suggested as a modification of his Schlieren method 7 (Oren, Durrett, & Ferguson, 1988; Rheinberg, 1896; Settles, 2001).

Later developments in colour Schlieren used filters to split up colours at the light source combined with a matching cut-off in place of the knife edge (Settles, 2001). This method has been recently used in the detection of very small Liquid Petroleum Gas (LPG) leaks where a 'Round Dissection filter' developed by (Settles, 2001) was used by Ting & Chen (2013). They named it microcolor Schlieren (Ting & Chen, 2013). While their application of colour Schlieren was successful in finding LPG leaks, the images they presented had very little colour intensity. This may be due to small alignment errors or weak colour filters. Improvements in sharpness and colour contrast can be achieved by using greater strength colour filters. Greater sensitivity may also be achieved by changing the Z-type Schlieren configuration used to a Double Pass arrangement.

### Sensitivity of the Schlieren System

Assuming a simple Z-Type Schlieren assembly, the sensitivity of the instrument is the ratio of change in illuminance caused by the test object to the background illuminance. The influencing factors are the mirror focal length and portion of knife edge cut-off. This is commonly referred to as contrast sensitivity (Settles, 2001).

Figure 9 shows a basic diagram of how light traveling from the test area in a Schlieren optical assembly is affected by the knife edge cut-off. The background illuminance is set by the proportion of unobscured light that passes the test area without being affected by disturbances. Light that is affected by a disturbance in such a way that it is refracted above the cut-off shows the disturbance as an area of increased light in the Schlieren image. Affected light that is refracted below the cut-off by a disturbance shows the disturbance as a dark area.



**Figure 9- The effect of cut-off on sensitivity**



The distance between the test area and the knife edge cut-off is determined by the mirror focal length. With a longer distance, light refracted by a specific angle gains a greater displacement when compared to the unaffected light and hence is easier to detect.

Disturbances that cause only a small amount of refraction require a high amount of knife edge cut-off to give enough contrast to be seen. With high cut-off and consequently low background illuminance, light that is refracted below the cut-off becomes harder to detect because of the lack of background illumination. A high brightness light source can help with this because it gives higher background illumination for a given proportion of cut-off.

At near to full cut-off, details are lost from the Schlieren image because disturbances that deflect below the cut-off are no longer detectable. Disturbances that cause a large angle of refraction also suffer when there is little background illuminance from high cut-off because they can cause the refracted light to miss the viewer completely.

From this understanding of the sensitivity of Schlieren optics, a balanced knife edge position is needed if one wants to view both small disturbances that need high cut-off and larger disturbances that require lower sensitivity.

#### **Previous Attempts at using Schlieren Optics for Detecting Leaks**

Previous studies to employ Schlieren optics for leak detection have been carried out in areas such as space flight, and the pipeline and gas industry. In these attempts, the main two problems that occurred were that the objects being tested were large (such as entire rocket boosters and gas lines), making the employment of traditional Schlieren optics impractical. The second problem was achieving a high enough contrast to visualise very small leaks. Modifying the traditional Schlieren technique with filters showed promise to resolve this (E Peale & L Summers, 1996).

Gary Settles showed propane leaking at 1 ml per second very clearly using a benchtop Schlieren assembly. He also proposed a portable leak testing setup using a modification of traditional Schlieren optics with a scanning fluorescent tube mounted between two posts (Settles, 1999).

In 2013, leaks of LPG from holes as small as 27.5  $\mu\text{m}$  in diameter with a pressure difference of 5 torr were visible with the use of colour Schlieren imaging experiments carried out by the National Taipei University of Technology (Ting & Chen, 2013). However, these tests produced images that had very faint details that are difficult to identify as well as little colour saturation.

### **2.1.3 Interferometry**

Interferometry works by splitting light from a single monochromatic source into two beams. These two beams then pass through the section of interest; one path contains data from the test subject and the other is used for reference to the original phase of the light source. When the beams of light are then recombined, phase differences between parts of the beam that experienced inhomogeneities in the test area and the reference beam cause areas of light and dark interference (Hariharan, 2007).

Interferometry has multiple modes of operation, the two most common of these are:

#### *Infinite*

In the infinite fringe setting, the optical path difference between the two beams is initially zero. When a disturbance is introduced in the path of the test beam, a set of fringes on which the difference in refractive index is constant is seen (Srivastava, Muralidhar, & Panigrahi, 2004).

#### *Wedge fringe*

In the wedge fringe setting, the optics is slightly misaligned to produce a set of straight fringes. When exposed to a disturbance, the fringes are displaced to an extent depending on the change in refractive index (Srivastava et al., 2004).

Interferometry suffers from the need of very accurate alignment; alignment error should be kept less than the wavelength of the light source (Lindsay, Anderson, & Sandercock, 1981).

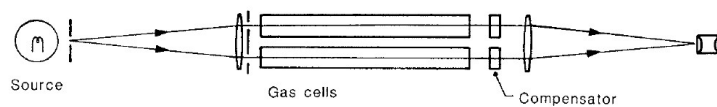
## Double path interferometry

Double path interferometry is a category of interferometry that uses separate optical paths for the reference and test beams from the source of the monochromatic light. This means that the reference beam will not encounter the test section and instead will be an accurate representation of the original light source.

Some notable examples of this style of interferometry include: Rayleigh, Michelson and Mach-Zehnder interferometry.

### *Rayleigh Interferometer*

A Rayleigh interferometer uses wave front division in the form of a double split or double aperture to split the source light into two beams, the beams then travel through the test section (generally two gas cells as in Figure 10) before being recombined. Two identical pieces of glass are placed in the beams and one is tilted to achieve calibration. Rayleigh interferometers are primarily used to measure the difference in refractive indexes of the two gases that are housed in the gas cells (Hariharan, 2007).

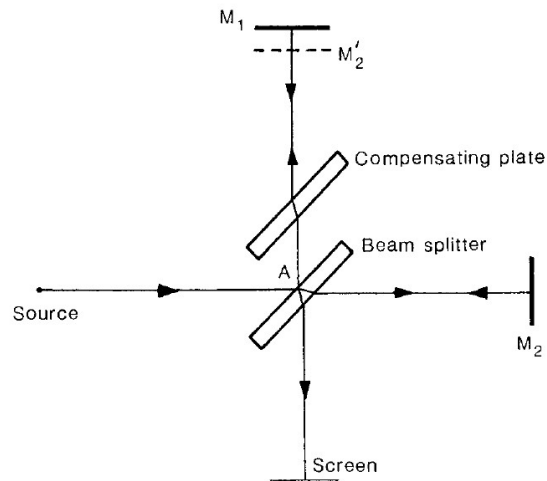


**Figure 10 - Rayleigh Interferometer (Hariharan, 2007)**

The biggest drawback of the Rayleigh interferometer is that the interference fringes produced are very close together, meaning that magnification is needed to see them (Hariharan, 2007).

### *Michelson Interferometer*

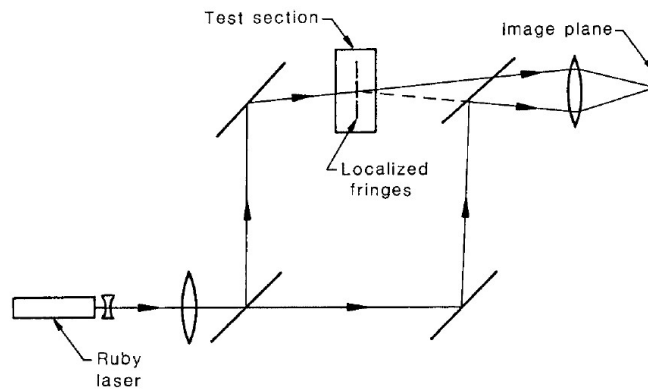
Michelson interferometers use a half-silvered mirror as a beam splitter to divide and recombine the beams. The movement of one of the mirrors allows the Michelson interferometer to be calibrated in a way that it can be used for spectrometry. In a Michelson interferometer, the two beams travel perpendicular to each other, as shown in Figure 11 (Block Engineering, 2017).



**Figure 11 - Michelson interferometer (Hariharan, 2007)**

### *Mach-Zehnder Interferometer*

Similar to the Michelson interferometer, the Mach-Zehnder interferometer uses a half-silvered mirror to split the source light into two beams. However, its layout, as shown in Figure 12, is much more complicated than the Michelson interferometer in Figure 11.



**Figure 12 - Mach-Zehnder Interferometer (Hariharan, 2007)**

Mach-Zehnder interferometry is the most common type used for visualizing fluid flows, and has been used since the end of the 19<sup>th</sup> century for use in the study of ballistics. More recently it has been used in both sub and supersonic wind tunnels (Chevalier, Latron, & Veret, 1957).

Unfortunately, the Mach-Zehnder interferometer has a reputation of being difficult to align with the two beams needing to be both parallel and the two paths must be near to

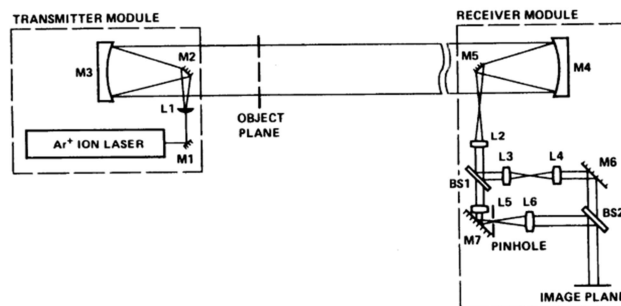
equal length within a wavelength of the light being used (Chen & Bird III, 1971). Chen & Bird developed an iterative method of aligning a Mach-Zehnder Interferometer using a red laser in an attempt to reduce the difficulty of alignment (Chen & Bird III, 1971).

### Common-path interferometry - Point Diffraction Interferometers

Point diffraction interferometers work by splitting a test beam into two beams by using a pinhole in a partially absorbing film. Part of the test beam is transmitted through the film and interferes with a spherical wave that is diffracted by the pinhole in the film if it is appropriately small enough (Smartt & Steel, 1975).

This technique was later modified with the use of a beam splitter so that a simpler pinhole without a transmitting film could be used, the assembly is aligned in the same way to a common Mach-Zehnder interferometer. This approach was called the improved point diffraction interferometer (Bachalo & Houser, 1985).

This approach shares similarities with the test section of a Z-type Schlieren assembly. The receiver module in Figure 13 that includes the beam splitters and pinhole can be made very compact allowing for fixed mounting that mitigates the effects of vibration (Bachalo & Houser, 1985).



**Figure 13 - Schematic of the improved point diffraction interferometer (Bachalo & Houser, 1985).**

## 2.2 Colour Methods

### 2.2.1 Infrared Imaging

Multiple studies have been carried out on the application of Infrared thermography to detect differences in temperature between escaping gas and the surroundings. These studies were particularly targeted at gas pipelines as vehicle mounted systems could check large areas in a relatively short time (Zhang, 1996).

### Currently available products

Commercial products exist from Forward Looking Infrared FLIR systems with two Infrared cameras that are calibrated for detecting gas leaks across a range of different industries. The Long Wave Gas Detection Camera is targeted at the electrical industry. Its sensor has a spectral range of 10-11  $\mu\text{m}$  making it especially helpful for detecting Sulphur Hexafluoride that is used for electrical insulation. The Mid Wave Gas Detection Camera is targeted at the Oil Refining and Petrochemical industry, with a wider range of detectable gases, including most fuels. Its InSb detector sensor has a spectral range of 3-5  $\mu\text{m}$ . Both cameras use a 320 x 240-pixel sensor (FLIR®, 2017). The cheapest of the FLIR leak detection cameras is the G300a with a 24 mm lens. This retails for \$130,347.38 Australian Dollar (AUD) (Industrial Monitoring and Control Pty Ltd, 2017).

Another company making cameras for this purpose is Opgal with their range of ruggedized handheld Infrared leak detection cameras designed for detection of volatile gases, but they share the same low 320 x 240-pixel resolution (Opgal, 2017).

### Sensors

The high cost of these imaging Infrared cameras is due to the sensor technology they use. Detectors with high sensitivity to mid and long range infrared light require expensive materials and complex cooling such as cryogenic coolers to keep the sensor operating at low temperatures (Rogalski, 2002), so that the sensor itself will not emit Infrared light in the form of heat (Ciupa & Rogalski, 1997).

Generally, these Infrared sensors are not manufactured in resolutions higher than 320 x 240 pixels. Higher resolution sensors are available, but are reserved for higher end maritime and military systems. Unfortunately, price lists for these imaging systems are not generally published. However, the price list for FLIR systems to the General Services Administration of the United States government is published online. From this list, a system with a High Definition (HD) thermal sensor, such as the FLIR Star SAFIRE 380 HD with a 1280 x 720 pixel Infrared sensor, costs in excess of \$780,000 USD (FLIR Systems Inc, 2015).

Sensors used in common digital cameras are normally limited to two types; Complementary Metal Oxide Semiconductor (CMOS) and Charge-coupled device (CCD)

sensors. Both have a very limited spectral response in the Infrared spectrum, however, they can be produced with very high resolution for relatively low cost. Most high-end consumer cameras now have CMOS sensors approaching 50 megapixels for less than \$2700 USD. An example of this is the Sony a7R ii with a resolution of 7952 x 5304 pixels (B & H Foto & Electronics Corp, 2017).

The graph in Figure 14 shows the approximate spectral range of common digital camera sensors of 300 to 1000 nm. This is far below mid wave Infrared used for leak detection, but still more than visible light that can be sensed by the human eye from 400 to 700 nm (Beeson & Mayer, 2007).

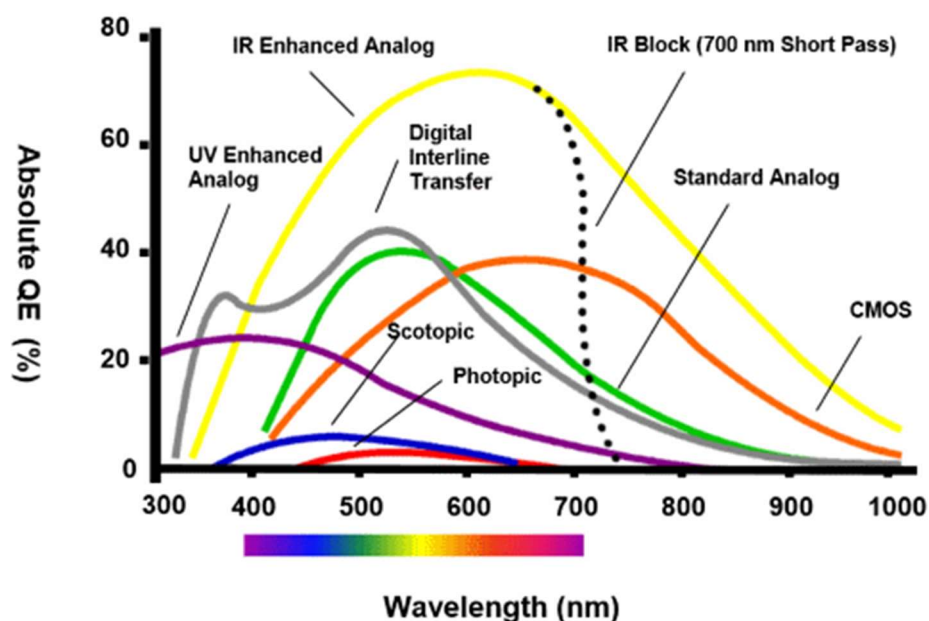
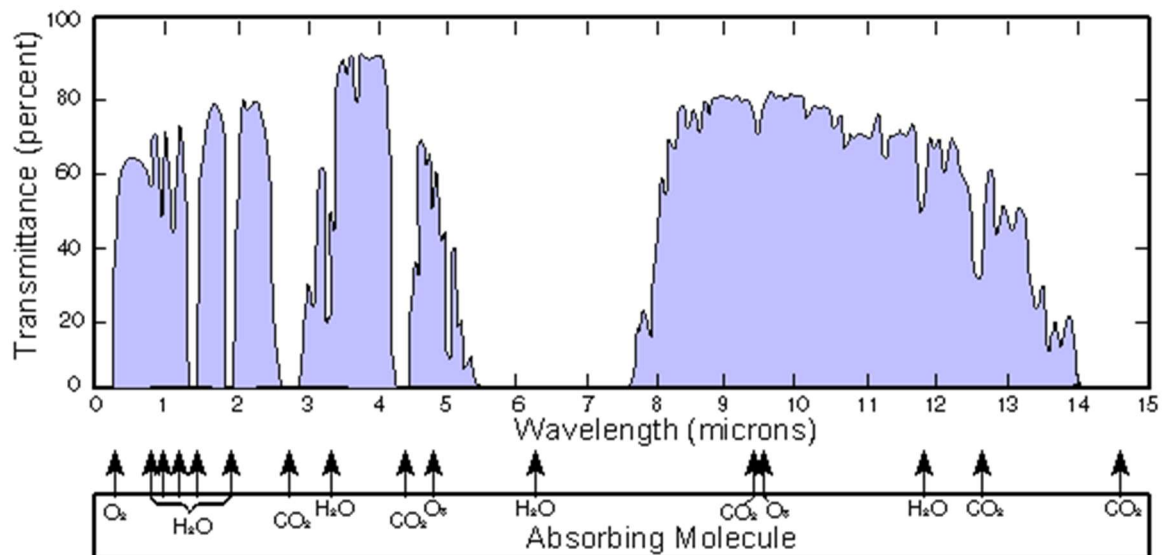


Figure 14 - Camera Sensor Absolute Quantum Efficiency Versus Wavelength (National Instruments, 2017)

#### Gases detectable by light

The plot in Figure 15 of the Infrared atmospheric window shows common gases in the atmosphere that can absorb specific frequencies of light. Oxygen and ozone block out ultraviolet light, while carbon dioxide and water vapour block out mid-range Infrared. Both these spectral ranges can be sensed by infrared cameras. However, the wavelength of the light source required to illuminate it so that a camera can sense it, is very dangerous to humans, specially for oxygen and ozone. Both have peak absorption at approximately 250 nm, which is the most dangerous frequency of cancer causing light to humans (World Health Organization, 2018).



**Figure 15 - Transmittance of Atmosphere Over 1 NM Sea Level Path (Infrared Region) (Naval Air Warfare Center Weapons Division, 2013)**

To get a better overview of gases that absorb wavelengths capable of being picked up by CMOS sensors, all gases with absorbance between 100 and 800 nm were downloaded from the free online Hitran Database and plotted in Figure 16 (Gordon et al., 2017). Of the gases in the Hitran Database, the most absorbent of light between 100 nm and 800 nm are Bromine monoxide, Nitrogen trioxide, Chlorine dioxide, Ozone, and Benzene. It should be noted that both Bromine and Benzene have boiling points higher than room temperature, so both are in vapour phase at room temperature. This would make them unsuitable for leak testing as they would condense inside the electronics enclosure being tested, leaving pools of toxic liquid. Unfortunately, the rest of the gases are also toxic to humans, even ozone, which has been shown to cause lung cancer in humans (World Health Organization, 2003).



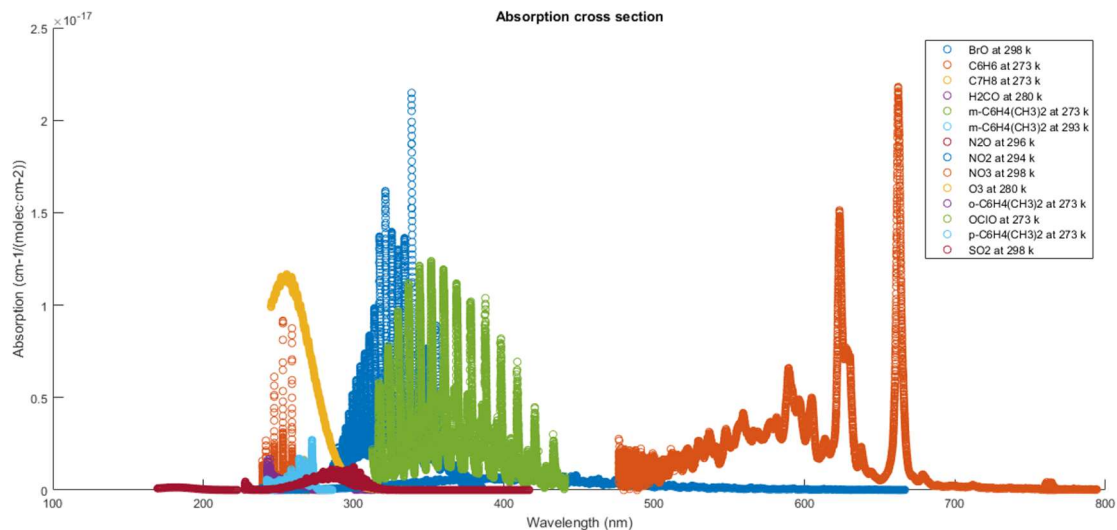


Figure 16- light absorption of gases between 100 nm and 1000nm (Gordon et al., 2017)

## 2.3 Non-visual Methods - Ultrasonic Leak Detection

All the above methods use differences in images for visual detection. By contrast, ultrasonic leak detection focuses on using differences in sound, specifically in the ultrasonic range. An ultrasonic microphone is used to detect the differences in sound and then this is converted to the audible range in real time so that the user can interpret the results. Unfortunately, the sensitivity of this method has been shown to be limited with the ultrasonic sound created by applying a vacuum to holes of 1 mm in diameter being barely detectable over ambient noise (D. Holland, Roberts, Chimenti, & Strei, 2005).

### 2.3.1 Passive Ultrasound Leak Detection

Passive ultrasonic leak detection is carried out by pressurising the test container with a test gas such as nitrogen or helium. Turbulent flow from the gas escaping at the location of a leak emits ultrasonic waves. By passing a microphone sensitive to ultrasonic sound over the test container, the leak can be found by a change in sound intensity and frequency (Moon, C. Brown, Mellen, & Lovelace, 2008).

### 2.3.2 Active Ultrasound Leak Detection

Active ultrasound leak detection is used when pressurising the test container is not possible due to safety concerns, or the leaks being tested are too slow or too small to cause turbulent flow. In this case, an ultrasonic wave emitter is placed inside the test container and escaping ultrasonic waves are detected by the microphone. Because the

frequency level is set by the emitter leaks can be detected by searching for peaks in intensity (Moon et al., 2008).

## **2.4 Summary of Leak Detection Methods**

### **2.4.1 Interferometry**

Interferometry offers high sensitivity to disturbances due to detecting the change in phase of light beams. This means that disturbances that cause changes of a fraction of a wavelength can be seen. Interferometry has multiple modes of operation, these include infinite fringe and wedge fringe modes. In the infinite fringe mode, disturbances cause the fringes to be visible. In wedge fringe mode, fringes are visible due to intentional misalignment. Disturbances cause the alignment and shape of these fringes to change.

The disadvantages of interferometry include high complexity due to the high number of optical elements needed to deal with multiple beams and consequently high price. Because of such high sensitivity and multiple beams being used, Interferometry needs very accurate calibration, so much in fact that the optical assembly needs to be kept in a relatively constant temperature environment because of thermal expansion due to change in temperature throughout the day.

### **2.4.2 Infrared imaging**

Infrared imaging offers a very compact and simple assembly to use, because it comprises of only a camera. However, it lacks the resolution necessary for detecting small leaks due to the cameras available having very low-resolution sensors (320 x 240 pixels is considered good). This only makes it suitable for larger leaks such as that of the gas and petroleum processing industry where it is currently used as well as aerial surveying of oil pipelines.

The gases detectable by infrared imaging are mostly hydrocarbons, meaning that they are generally very flammable and toxic. Another factor is price, with units costing more than \$100,000 USD each due to the complexity of the cooling system used to cool the sensors so that they do not radiate infrared light. The requirement of specialised lenses that do not have infrared blocking coatings is another contributor to cost.

### **2.4.3 Schlieren Optics**

The biggest differences between Schlieren optics and interferometry is the principle that they use to detect change. Schlieren optics detects inhomogeneities that cause differences in the angle of light due to refraction. Interferometry, on the other hand, detects difference in phase between two light beams which can be affected by distance and speed.

Double pass Schlieren optics offer one of the strongest points of Schlieren optics over interferometry by only requiring a single mirror. In contrast, interferometry needs many mirrors or lenses for the two beams used. This makes Schlieren optics simpler to align due to the lower number of optical components needing alignment. The lower optical component count of double pass Schlieren photography also helps to keep costs down in comparison to interferometry.

Schlieren optics' main disadvantage is a large assembly size; for a double pass setup the distance between the light source, and the mirror needs to be twice the mirror focal length). For a 6-inch f/10 mirror, this becomes more than 3 meters. For a 12-inch f/10 mirror, it needs to be over 6 meters.

Schlieren optics also can offer the ability to convert magnitudes and orientation into different colours using a colour filter, allowing the user a more intuitive way to distinguish between different disturbances.

### **2.4.4 Chosen method**

Schlieren optics was chosen over the other two methods for a variety of reasons (Table 1). In comparison to interferometry, Schlieren optics is cheaper and less complex with near to the same sensitivity. Compared to infrared imaging, it is also cheaper and much safer as it does not require dangerous tracer gases or light sources. Schlieren optics' main disadvantage over the other two options is its large size.

**Table 1 - advantages and disadvantages of different methods**

|                  | Uses a tracer gas that is non-toxic | Illumination by a light source that is at a safe frequency | Low-complexity | Low-cost | Small form factor | High sensitivity | Score |
|------------------|-------------------------------------|--|----------------|----------|-------------------|------------------|-------|
| Interferometry   | Yes                                 | Yes  | No             | No       | No                | Yes              | 3     |
| Schlieren Optics | Yes                                 | Yes  | medium         | Yes      | No                | Yes              | 4     |
| Infrared imaging | No                                  | No   | low            | No       | Yes               | No               | 2     |

## 2.5 Image Processing

Modern cameras offer the ability to capture a much greater range of image information than the human eye can see. Processing of the raw data in the images produced by these cameras is required to ensure that fine details that would normally be indistinguishable can be made visible.

### 2.5.1 Contrast Adjustment

Contrast adjustment is the expansion of image intensity across the colour range. Part of an image one is trying to emphasize may be in a very narrow range of a particular colour; to add contrast to this image, this detail is spread across the full range of colour.

An example of this can be seen in Figure 17, where an image taken from the peak of Hong Kong Island has very little contrast in the original image on the left-hand side due to smog. This can also be seen in the histogram below it, with all the image intensity (Y Axis) grouped in the centre of the colour range (X Axis). The image with contrast adjustment on the right-hand side shows far more noticeable detail; when viewing the histogram, it is apparent that the colour intensity has been spread out across the full range of colour.

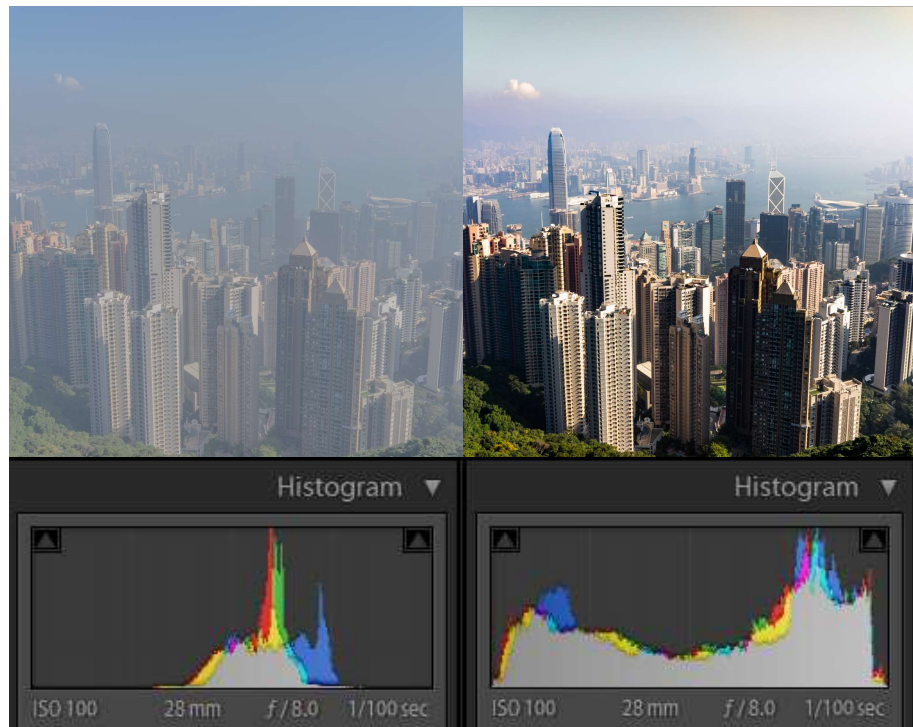


Figure 17 - Contrast Adjustment: Original Image (left), Contrast Adjustment (Right)

## 2.6 Computer Vision

Computer Vision expands upon image processing to a new level with a more automated approach of distinguishing objects of interest. Given a training dataset, a neural network can be trained to recognise and classify if an image contains an object of interest and outline the location of that object at a Regional or even pixel level.

In recent years, interest in computer vision has boomed, in part due to the creation of the ImageNet database (Fei-Fei, 2009). Since the creation of the ImageNet database, the ILSVRC competition has shown a rapid increase in image classification accuracy of convolutional neural networks, with the 2015 winner exceeding the accuracy of a human (Shawn & Christiaan, 2017).

The plot in Figure 18 shows the progression of neural network accuracy since the creation of the ImageNet competition, notable winners are: Alexnet 2012 with a top 5 classification error of 15.3%, GoogLeNet 2014 with a top 5 classification error of 6.63%, and ResNet 2015 with a top 5 classification error of 3.57%, even with a couple of days' training, the best human result was 5.1% (Schlag, 2016).

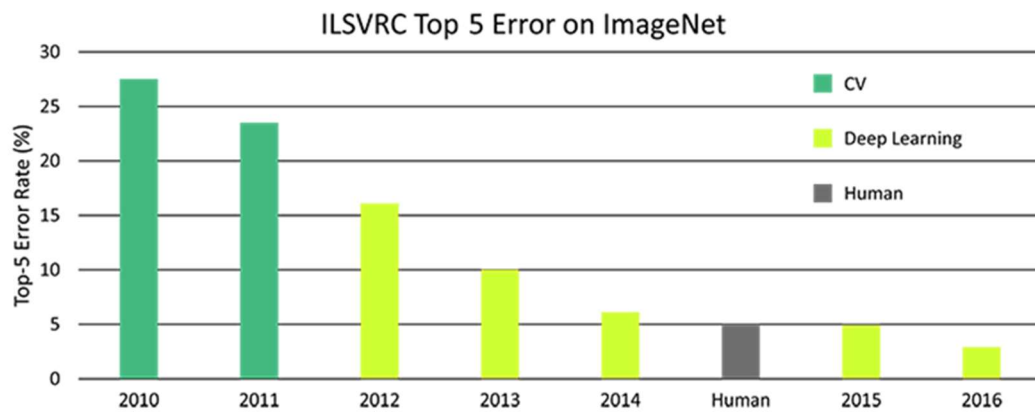


Figure 18- ImageNet Top-5 Classification Error Over Time(Shawn & Christiaan, 2017).

### 2.6.1 Convolutional Neural Networks

Convolutional neural networks are built up of layers that react to an input image in a way that is inspired by the way biological visual processing occurs in animals (Lecun & Bengio, 1995). Convolutional neural networks take input data in the form of pixel data (when used for images) and, through a range of layers and activation functions, predict an output based on previously learned data. Each cell of data in each layer's matrix is called a neuron, because it is designed to act in a similar way to neurons in the brain.

#### *Input layer*

Convolutional neural networks start with an input layer, this layer passes the pixel data on to the first convolutional layer. In the convolutional layer, feature maps with different weightings are moved over the input data by a set number of pixels, called a stride. At each stride, the dot product of the feature map and the area of the input layer it currently covers is calculated (Mathworks, 2018b). This process is shown in Figure 19 when the feature map (in orange), is overlaid on top of the input layer, the dot product is calculated and inserted into a single cell of the output layer.

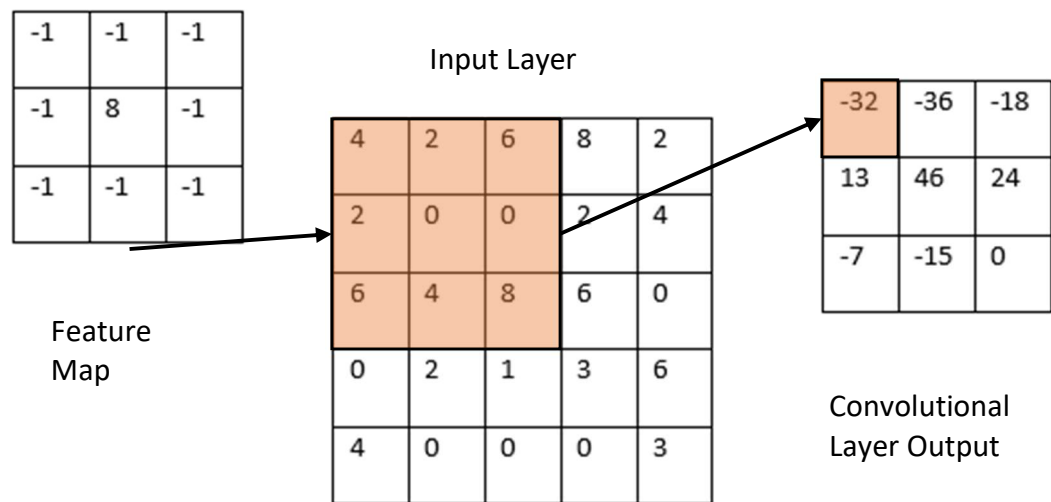


Figure 19 - The Input Layer

### ReLU

The next layer that normally follows a convolutional layer is a rectification layer, usually called a rectified linear unit (ReLU). This introduces non-linearities into the neural network by applying a pixel wise operation that changes any negative value to zero as demonstrated in Figure 20. The ReLU layer helps by adding sparsity to the networks. This is favourable for computational efficiency and has also been shown to increase training accuracy (Glorot, Bordes, & Bengio, 2011).

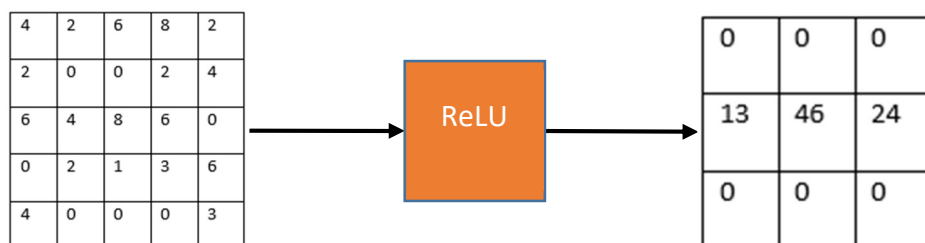
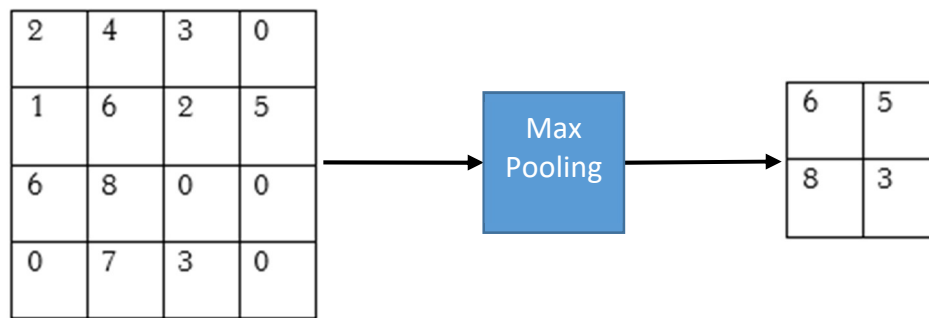


Figure 20 -The ReLU Layer

### Pooling

Pooling is a form of down sampling that reduces the size of the layers later in the network. Normally, a maximum or average is used to condense multiple inputs to the pooling layer to a smaller number of outputs. In Figure 21, max pooling is used to reduce a 4 by 4 input to a 2 by 2.



**Figure 21 - The Pooling Layer**

### *Fully Connected and Output Layers*

The last few layers in convolutional neural networks are made up of fully connected layers that (as the name implies) have connections between every neuron in the past layer to every neuron in the fully connected layer. The last fully connected layer in the network passes the data onto a 'softmax' layer that calculates the probability of the image containing the one of the classes of objects that the network was trained to find.

### **2.6.2 Classification with Convolutional Neural Networks**

Classification is one of the simplest uses of Convolutional Neural Networks. Given an image, it will give a prediction of the most dominant feature that the image contains.

In terms of the application for detecting leaks in the Schlieren images, this type of neural network would only be able to tell if a leak was present or not. This is not that useful for Navico as, during the testing procedure, a product can be quickly tested by applying a vacuum to it and measuring vacuum loss over a few seconds.

### **2.6.3 Region-Based Convolutional Networks**

Region-Based Convolutional Networks are a form of object detector that uses convolutional neural networks to classify regions inside an image that are likely to contain an object (MathWorks 2017). For the application of finding leaks in Schlieren images, Region-Based Convolutional Networks are far more suited than classification networks because, instead of just classifying an image as having a leak or not, they also are able to predict location. Once this location is detected, the network can be used to draw a box around the predicted region.



#### 2.6.4 Stochastic Gradient Descent with Momentum

To train a network in MATLAB, the `trainNetwork` function is called upon; this function uses stochastic gradient descent with momentum shown in (1) for increasing the accuracy of the neural network during training by adjusting the weighting of each connection:

$$(1) \quad \theta_{l+1} = \theta_l - \alpha \nabla E(\theta_l) + \gamma(\theta_l - \theta_{l+1})$$

The parameter vector  $\theta$  is essentially a vector of the weighting of each connection in the network and a given iteration  $l$ . Initially, it is given a random value following a Gaussian distribution (or sometimes, in the case of pre-trained networks, they are inherited from the previous network).

Stochastic gradient decent uses the gradient of the loss function  $E(\theta_l)$  which is the sum of the difference between the output of the neural network and the expected output (HU, 2017). This is multiplied by the learning rate  $\alpha$ . Minimising the loss function gives a network with an output close to the expected values from the training data.

The momentum term  $\gamma(\theta_l - \theta_{l+1})$  is added in an attempt to reduce oscillations in the error gradient by adding the difference from the previous iteration multiplied by a momentum coefficient  $\gamma$  (MathWorks, 2018c).

#### 2.6.5 Training Options and their effect on Network training

There are many different settings and values that must be selected before a network can be trained. These settings directly affect the performance of training by changing the parameters within the Stochastic Gradient Descent algorithm.

##### Execution Environment

Networks can be trained using a computer's Central Processing Unit (CPU) or Graphics Processing Unit (GPU). For most cases, the GPU is chosen due to its much higher speed at training networks because of its ability to run many tasks in parallel efficiently (Avinash Nehemiah, 2017).

### MaxEpochs

An epoch is the period the training algorithm takes to go through all the training images once. Setting the maximum epoch limits the training time and stops training once this point is reached.

### Minibatch Size

A minibatch is a small batch of the training images that the training algorithm uses for each iteration; the whole training data set is not normally used as it would require more video memory than modern GPUs have available. Minibatch sizes that are too small result in the loss function oscillating and in very long training times and, possibly, no improvement of the network.

### Learn rate

The network learn rate is a set constant that controls how quickly the Stochastic gradient decent algorithm changes the network. If the learn rate is too low then it takes many epochs to train the network, but if it is set to high, then overfitting and low-quality training results.

### Momentum

The momentum coefficient  $\gamma$  is the factor in which the gradient from the previous iteration affects the current iteration.

## 2.6.6 Pre-trained networks

Instead of developing a neural network from scratch, most modern applications of convolutional neural networks rely on retraining existing networks that have already been trained on large data sets, such as the ImageNet database.

In this project, the pre-trained Alexnet, VGG16 and VGG19 networks are used. These networks have already learned feature representations from training on over a million images in the ImageNet database (Mathworks, 2018a) and have shown high accuracy in the ILSVRC competition. Alexnet won the ILSVRC competition in 2011 with a Top-5<sup>1</sup> error of: 15.3% and a Top-1<sup>2</sup> error of: 36.7% (Krizhevsky, Sutskever, & E. Hinton, 2012).

---

<sup>1</sup> Top 5 error means that 1 of the top 5 predictions by the network was correct.

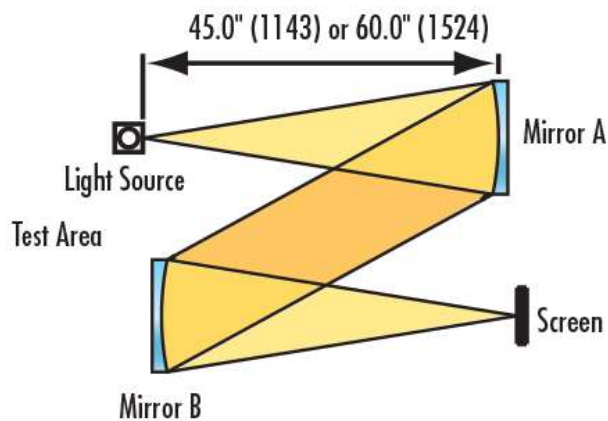
<sup>2</sup> Top 1 error means that the top prediction by the network was correct.

The VGG network scored well in the 2014 ILSVRC competition with a with a Top-5 error of: 7.3% and a Top-1 error of: 24.7%. Shortly after the competition, the network was improved upon giving a Top-5 error of: 6.8% and a Top-1 error of: 23.7% (Simonyan & Zisserman, 2014).

### 3 MATLAB Raytracing of Schlieren Optics

#### 3.1 2D Ray Tracing

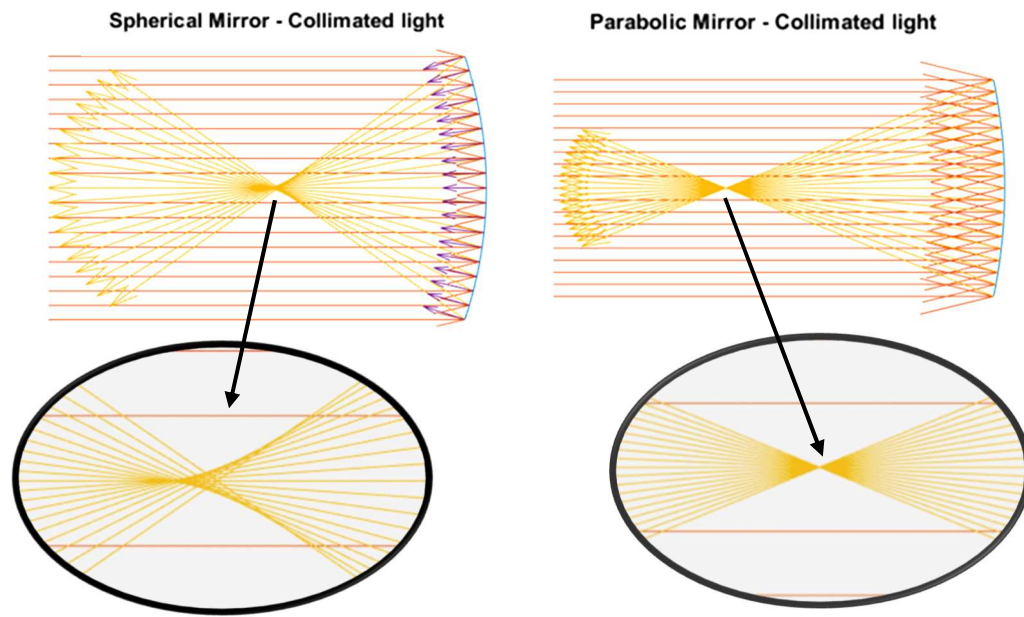
Surprisingly, the Schlieren optical kit purchased by AUT contains two spherical mirrors instead of parabolic mirrors that would normally be used in a Z-type Schlieren assembly. To make sure this was not a mistake, Edmund Optics was contacted via email. The reply given for the use of spherical mirrors was that they were substituted for parabolic mirrors to cut cost. The layout Edmund Optics recommends is shown in Figure 22.



**Figure 22 Edmund Optics Z-type Schlieren assembly (Edmund Optics Inc, 2017)**

To understand the effect this would have on the operation of the Schlieren system, a 2D MATLAB ray tracing program was created using an assumption of regular reflection to simulate how spherical and parabolic mirrors reflect collimated and diverging light.

The Z-type Schlieren system requires the first mirror to turn the light from the point source into parallel beams that then travel to the second mirror to be focused to a point at the knife edge, the second part of this is demonstrated in Figure 23 comparing spherical and parabolic mirrors for focusing parallel light to a point.

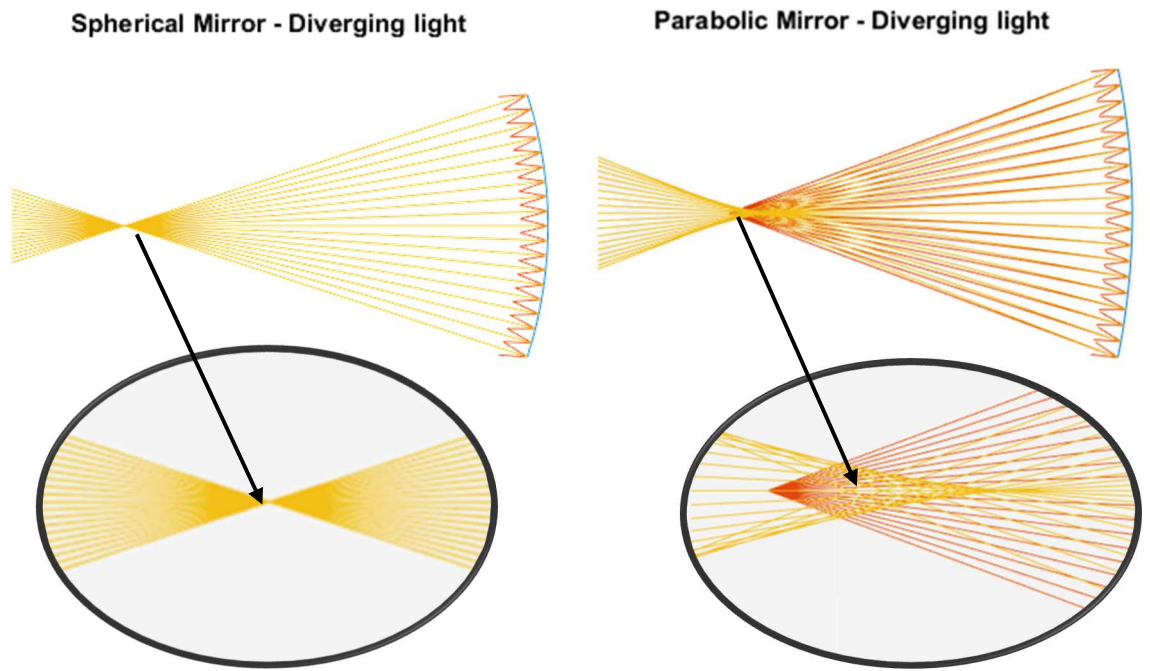


**Figure 23 - Comparing spherical and parabolic mirrors for focusing collimated light**

The results from the MATLAB program show that, while a spherical mirror can partially focus parallel light, it fails to do so at a singular focal point in the way a parabolic mirror can. The inability for the spherical mirror to focus the light to a single point means that images taken with a Z-type Schlieren system will not have even focus across the mirror, resulting in out-of-focus images.

Nevertheless, a spherical mirror can be used with a double pass-type Schlieren setup where a single spherical mirror is used to reflect light from a point light source back to the knife edge located in the same place as the light source. To demonstrate this, the same program is used to compare spherical to parabolic mirrors for focusing light from a point source back into a point.

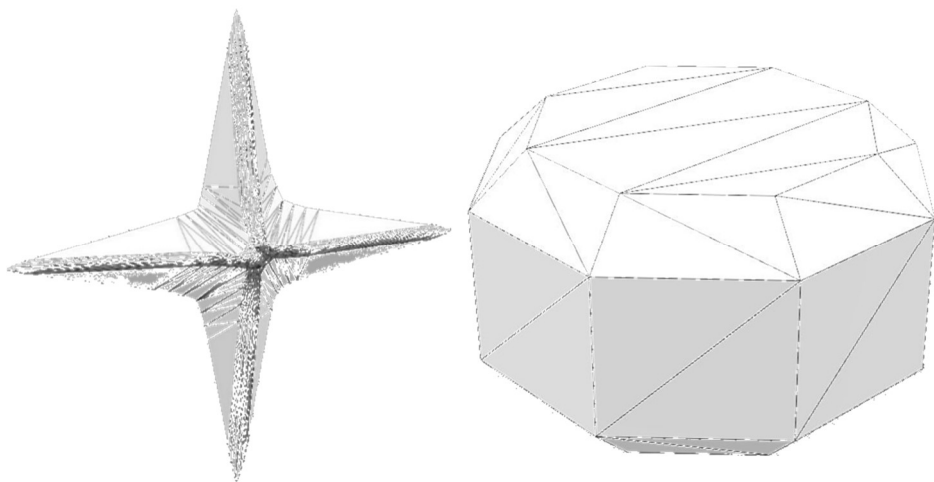
As the basic ray tracing in Figure 24 shows, a spherical mirror is better suited to a double pass Schlieren assembly. Even with a slight offset between the light source and focus point, a spherical mirror focusses the light to a sharp point reasonably well. However, a beam splitter could be used to minimise all off-axis aberrations by changing the layout from an Off-Axis Single Mirror Schlieren to Single Mirror Coincident Schlieren.



**Figure 24 - Comparing Spherical and Parabolic mirrors for focusing diverging light from a point**

### 3.2 3D Ray Tracing

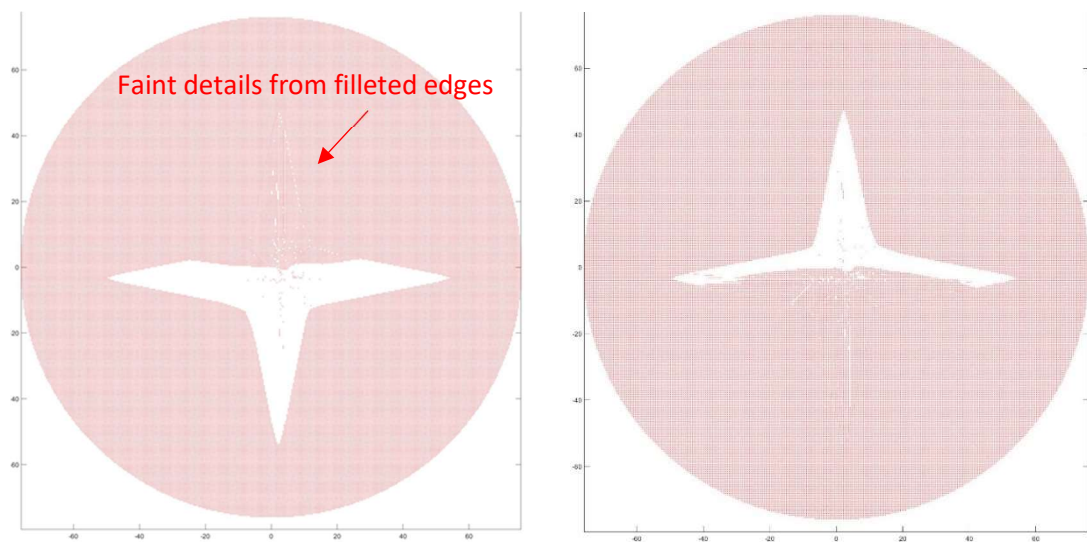
The 3D ray tracing program was tested on two different Standard Triangle Language (STL) files shown in Figure 25, an octagon with chamfered edges as well as a 4-point star with fillets. These two shapes were chosen for their simplicity, which results in less computational requirements and causes refraction to occur in many different directions.



**Figure 25 – The two STL files used for testing the 3D ray tracing program**

The star had the highest number of faces, so it took significantly longer for the ray tracing program to compute than when the much simpler octagon was used. However, the high number of faces was advantageous when the ray tracing program was used to test the limits of sensitivity, because the faint details of the fillets could be seen.

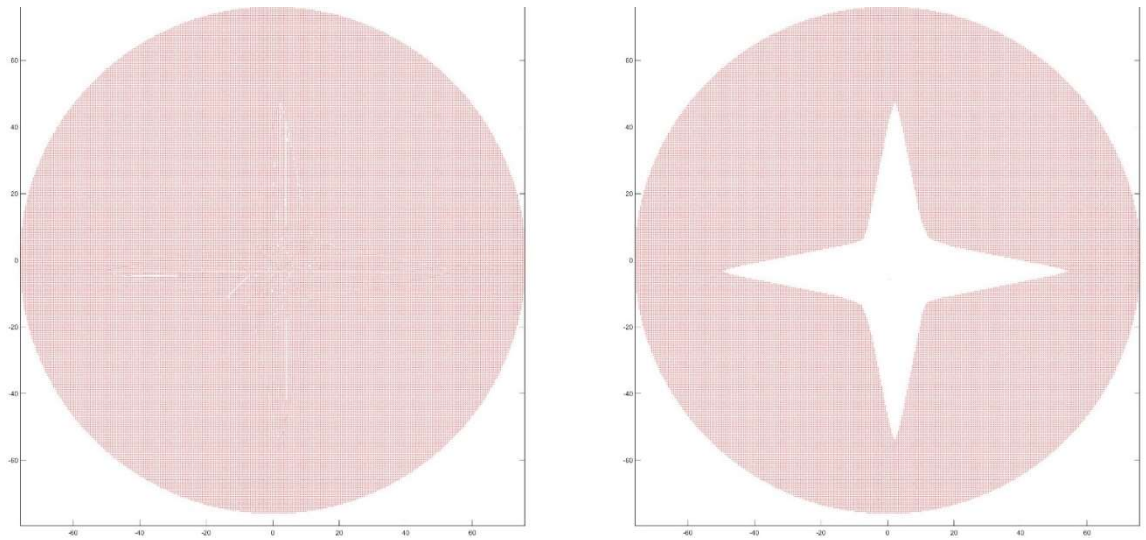
One of the first things to become apparent when testing the virtual Schlieren optical assembly is that, if a single knife edge is used, only one direction of refracted light is cut off. This means that when a single blade position is used, it gives an incomplete picture of the inhomogeneities. This is shown by the two different cut-off directions in Figure 26.



**Figure 26 - Star STL file with a 10mm radius cut-off shifted up 1mm (right) and down 1mm (left)**

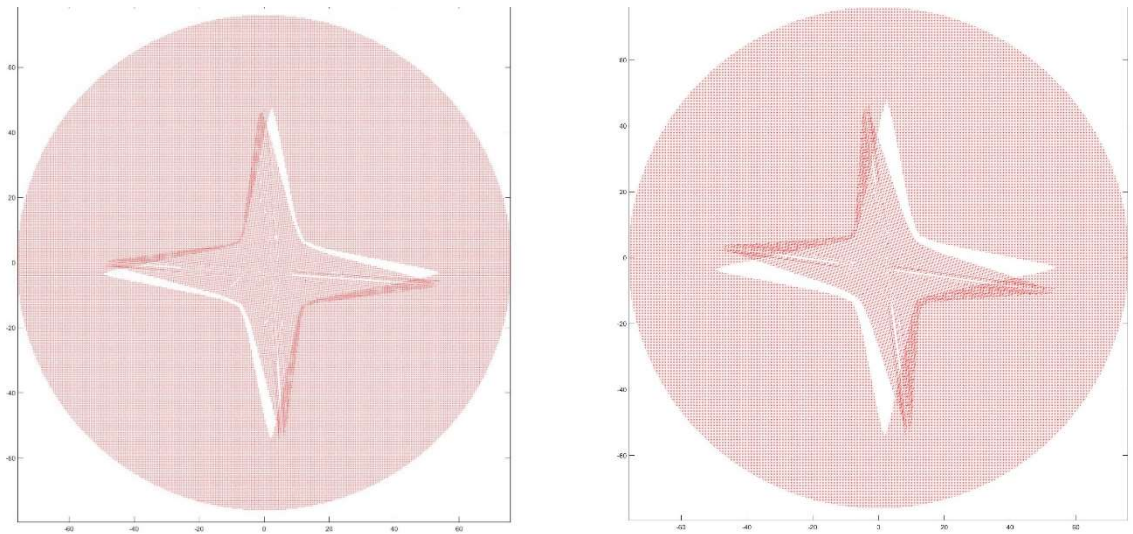
By varying the amount of cut-off in the virtual optical assembly, the different parts of the inhomogeneities become visible. With slight 0.5 mm movement of the cut-off edge, the faint details around the fillets and edges are visible (left). When the cut-off is moved further to 1.5 mm, the entire inhomogeneity of the star becomes cut-off and the detail around the fillets and edges are lost (right). Figure 27 shows the effect that higher amounts of cut-off has upon sensitivity. With the smaller 0.5 mm shift in cut-off, details in the centre of the star are visible; with the larger 1.5mm shift in cut-off, these details are lost, but the overall sensitivity of the system increases to the rest of the star.





**Figure 27 - Star STL file with a 10mm radius shifted up 0.5 mm(left) and shifted up 1.5 mm (right)**

The effect of the light source pinhole size is shown in Figure 28. Increasing the size of the light source from a single point to a 20 mm diameter disk causes significant 'ghosting' to occur in the image. The effect was less noticeable when the diameter of the light was reduced to a 10 mm diameter.



**Figure 28 - Star STL file with extended light source with a 5mm radius(left) 10mm radius(right)**

The result from the ray tracing program was verified with AUT's improved Schlieren optical setup using a green light source in Figure 29. When the pin hole was not used, 'ghosting' was seen on the image (left) as was expected from the ray tracing program.



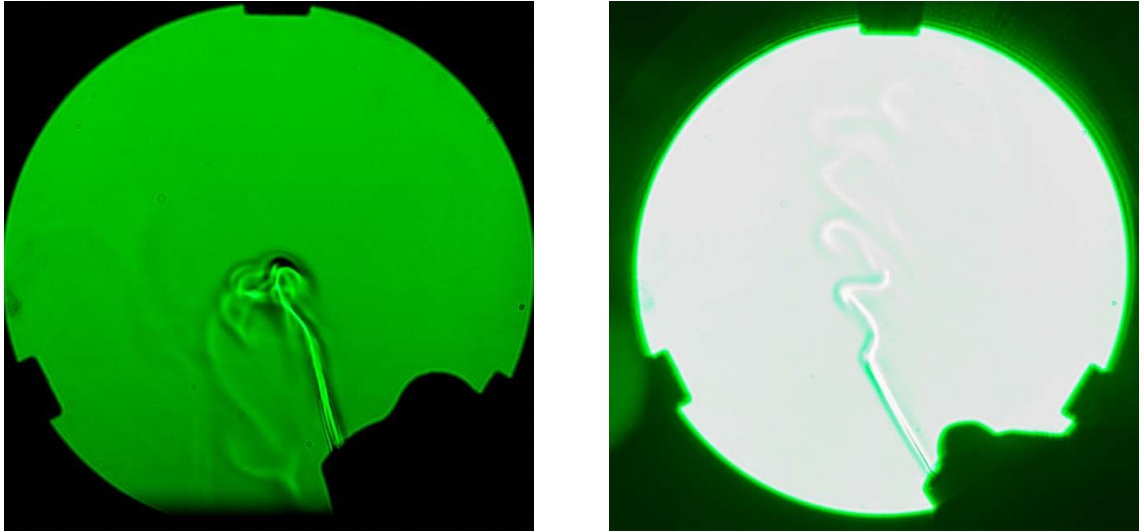


Figure 29 - Testing the light source pin-hole (left) and without the light source pin-hole (right)

### 3.3 Lessons in Schlieren Optics from Basic 3D Ray Tracing

To better understand the way that differently-shaped cut-off filters affect the sensitivity and image quality of the Schlieren image, a 3D MATLAB ray tracing program was written to simulate a double pass Schlieren optical assembly. To simulate a double pass Schlieren assembly, the program needs to be able to calculate reflection and refraction, as well as find where rays intercept the surface of the Schlieren object. The object can be imported from a STL file by reading the location of the nodes of each face using a string read.

The light from the source is projected towards the mirror at even increments using a mesh-grid as per Figure 30. This is to ensure that the Schlieren object is evenly illuminated to give a Schlieren image with even illumination across the frame.

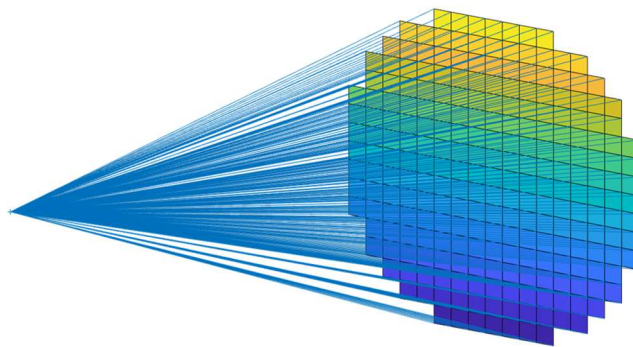
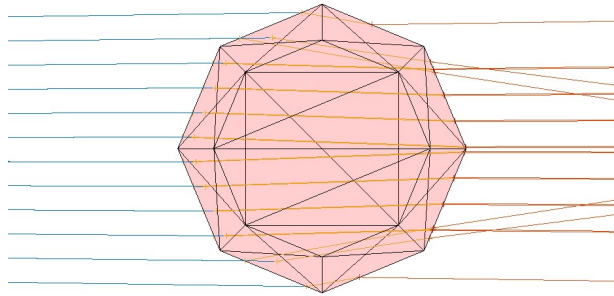


Figure 30 - Light from the point light source hitting the mirror with a very low number of rays

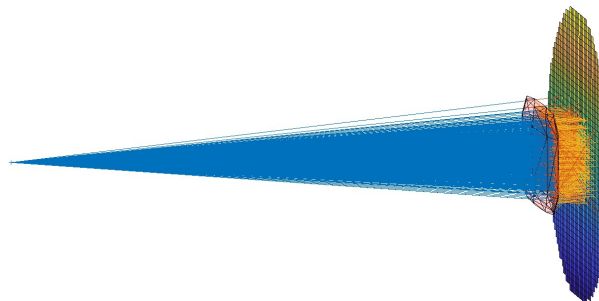
To find where the rays first intercept the Schlieren object, a separate function is used that finds all the locations of intercept with the Schlieren object between where the ray would hit the mirror and the light source. Each ray that hits the object has two points of intercept, the one nearest to the origin of that ray is kept.

Using the intercept of the Schlieren object and the direction of the impacting ray, the exiting ray's direction can be calculated using Snell's law. This means that the way light travels through a transparent object due to refraction can be modelled as shown in Figure 31.



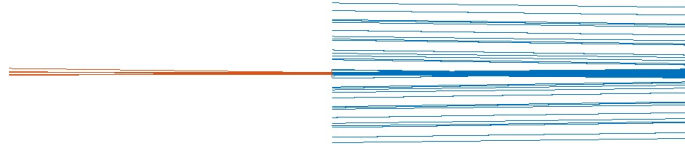
**Figure 31 - Internal refraction inside a chamfered octagon**

Once the programme has modelled the rays completing the first pass of the Schlieren object, the rays then hit the mirror and are reflected, passing once again through the Schlieren object where refraction occurs once again on the light's way back to the cut-off point at the focal point of the light rays (Figure 32).



**Figure 32 - First pass of light rays traveling through the test section and hitting the mirror**

The final part of the model is the cut-off, where returning rays that are focused to a point by the mirror encounter a cut-off point. Rays that are significantly affected by refraction are not reflected to the same point as less affected rays, so they do not pass through the cut-off, whereas the less affected rays pass through to the image plane (Figure 33).

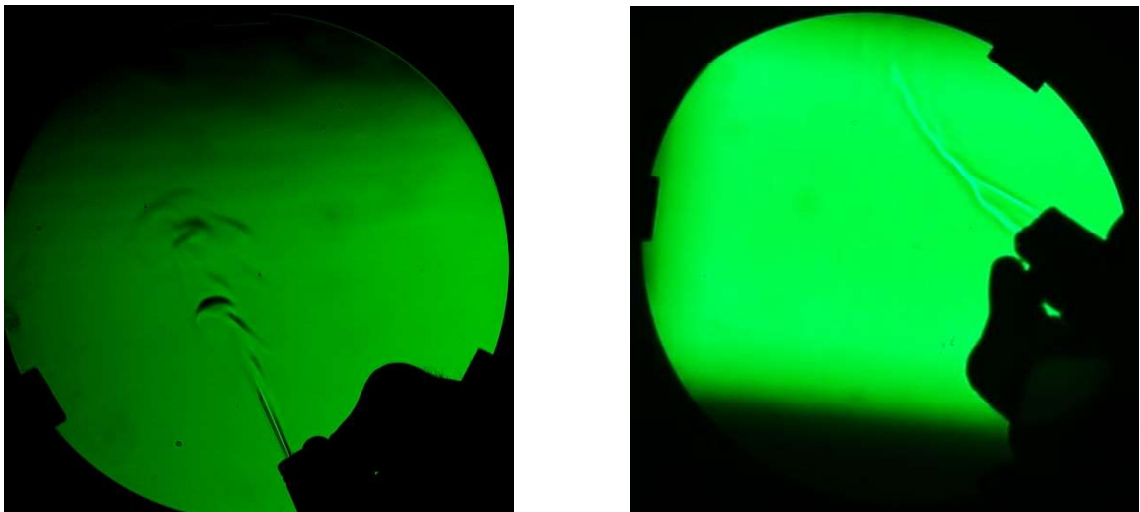


**Figure 33 - Returning rays passing cut-off, the diverging rays are removed but the unaffected rays in orange pass by**

## 4 Development of Schlieren Optical Setup for Leak Detection

The testing and development of Schlieren optics was carried out in three distinct stages; at each stage limitations of the optical assembly were assessed and the next stage of development was used to attempt to improve upon these limitations.

In the first stage, existing equipment that AUT used on previous projects was used to assemble both a Z-type and Double Pass Schlieren Optical setup. Both setups were tested to find the limitations in resolution and sensitivity to small disturbances, as well as any limitations in the ease of use. Testing of the Double Pass and Z-type configurations in Section 4.2 showed that the Double Pass configuration was much more sensitive when detecting a jet of gas from an isobutane lighter. This is demonstrated in Figure 34.



**Figure 34 – Double Pass (left) compared to Z-Type (right) showing isobutane gas escaping from a lighter**

During testing of these two Schlieren configurations, it was found that the green light source that AUT used with their previous experiments had a very short run time before overheating and shutting down. This short run time made it very difficult to align the optical assemblies, when halfway through alignment the light would shut off, and a large amount of time was required for it to cool down enough to restart. Upon restarting the light, the action of pressing the switch would bump it back out of alignment.

In the second stage, improvements were made upon the existing optical setup in terms of the main limitations found in Section 4.2. Since double pass Schlieren optics showed superior sensitivity, this configuration was chosen for further experiments. To improve upon the double pass optical configuration, the light source was changed to a higher intensity white LED with focusing lens and heatsink capable of extended run times. The development of this light source is documented in Section 4.3.1. The choice of white light allowed for the same light source to also be used for experimentation of Colour Schlieren as described in Section 4.3.4.

The knife edge was changed from the blunt plate provided by Edmund Optics to a sharp blade from a utility knife mounted in a 3D-printed stand. This proved to be much easier to focus than as described in Section 4.3.2. This allowed the testing of different angles of cut-off, and it was found that easier cut-off adjustment was attainable with the knife edge at 45 degrees.

Testing after the second stage of development as described in Section 4.3.4 found that monochromatic Schlieren optics were a lot more user-friendly to align and adjust when compared to colour Schlieren. The images returned by monochromatic Schlieren were also easier to interpret because they had a more uniform background.

Obtaining repeatable results proved to be problematic with all the different components on the lab bench; adjustment of one part or movement of the user around the lab occasionally caused enough vibration to put the rest of the optical assembly out of alignment. It was also of note that a longer focal length lens could be used on the camera to better frame the test area and make use of the full resolution of the camera's sensor.

To improve repeatability of testing the camera, light source, light trap and beam splitter were mounted onto a heavy aluminium base that significantly helped with maintaining and adjusting alignment. This is described in Section 4.4.6. The lens was changed for a longer focal length, manual focus lens that allowed for better use of the full frame of the camera's sensor but provided a tighter crop of the test area.

The ease of use of the optical assembly was improved by motorising the knife edge on a linear slide and controlling it via a MATLAB-generated user interface as described in Section 4.4.2. The test section was also updated with a rotary platform that allows for

automated movement of the test piece via the same interface as the knife edge. (Section 4.4.3). This helped to minimise disturbance to the air from the heat of the user while they were moving the product.

Smaller improvements were made in the form of a light trap to stop unwanted light from the beam splitter escaping into the surrounding environment (Section 4.4.7) and a more stable base for the mirror (Section 4.4.8).

All testing of Schlieren optical setups on Navico's products was conducted using helium at a maximum pressure of 50 mbar in order to avoid the risk of the product rupturing. Each time a test was conducted, the enclosure was given one minute to fill with helium, however, leaks located at the top of the enclosure started to become visible after less than a few seconds of pressurizing the enclosure.

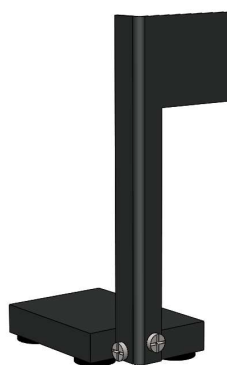
## 4.1 AUT's Existing Schlieren Optical Setup

AUT previously purchased a Z-type Schlieren optical kit from Edmund Optics for use in the thermodynamics laboratory for visualising convection currents in air. The kit as shown in Figure 34 includes two 6" diameter 60" focal length spherical mirrors with a  $\lambda/8$  surface accuracy.



**Figure 35 - 60" Focal Length, 6" Schlieren System (Edmund Optics Inc, 2017)**

The knife edge supplied with the kit is a piece of black anodised 1.5 mm aluminium plate with a simple base made from aluminium and four felt feet. The overall height of the knife edge is 150 mm. Available components of the optical setup were modelled in Solidworks at the beginning of the project before any changes were made; the model of the knife edge can be seen in Figure 36.



**Figure 36 - Solidworks rendering of the supplied knife edge**

## 4.2 Double Pass Schlieren Optics

From the review of literature in Section 2.1.2 it was suggested that Double Pass Schlieren optics should yield higher sensitivity than Z-type Schlieren Optics due to the light passing the test section twice. Simple 2D raytracing in MATLAB as carried out in Section 3.1 showed that for a spherical mirror, focusing of the Z-type setup to a fine point would not be possible. To confirm this, AUT's optical components were used to set up both configurations using the spherical mirrors from the kit to see if the difference in focus between the two mirrors seen in the ray tracing had a tangible effect on the focusing performance of the Schlieren assembly.

The two assemblies were focused on the retaining bracket that holds the edge of the mirror using the same 135 mm manual focus lens. To test the performance of the optical assemblies, an isobutane lighter was held in the test section with the valve held open without lighting it to release a jet of gas. Isobutane is a vapour at room temperature with a density of  $2.452 \text{ kg/m}^3$  compared to the  $1.198 \text{ kg/m}^3$  density of air. For comparison, the density of helium is  $0.1641 \text{ kg/m}^3$  under the same conditions. While density is not the only factor that determines the refractive index, it is an approximate indication of the difference in refractive indexes, given that there are very few published values for the refractive index of isobutane in vapour form.

The results from this test in Figure 34 shows that the Z-Type configuration suffers from poor focus that worsens from the edges of the mirror inwards. This uneven focus across the frame can be explained by Figure 23 where the ray tracing results show that collimated light cannot be focused to a perfect point by a spherical mirror.

## 4.3 Initial Improvements to the Existing Schlieren Optical Setup

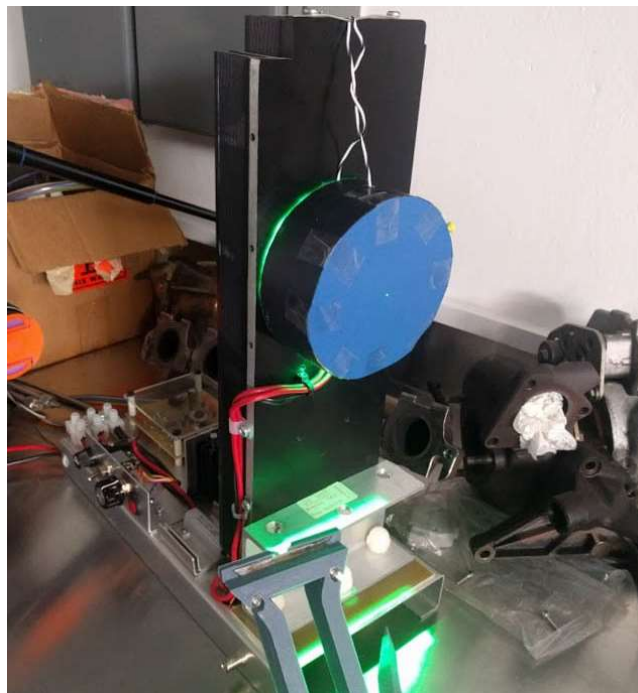
Initially the kit from Edmund Optics came with a small incandescent light bulb for the light source shown in Figure 35. This was destroyed during previous use of the Schlieren assembly when the light source was run on standard 230 V New Zealand power supply instead of the 120 V it was designed to run at. Before the commencement of this project, the original light source from Edmund Optics was replaced with a Luminus Devices CBT-120 LED mounted to a large heatsink. The green led chosen is capable of outputting over



2000 lumens constantly or nearly 3000 lumens in pulsed mode (Luminus Devices Inc, 2016).

Since the Luminus Devices LED was of moderate expense, a controller board was made with built-in protection by using automatic over-temperature shutoff as well as limiting the voltage at which the LED would turn on. This became a disadvantage when operating the light source for more than a few minutes, because the heatsink used could not effectively cool the LED. This would cause the LED controller to enter thermal shutdown, taking a long period to cool down before the controller would allow operation again.

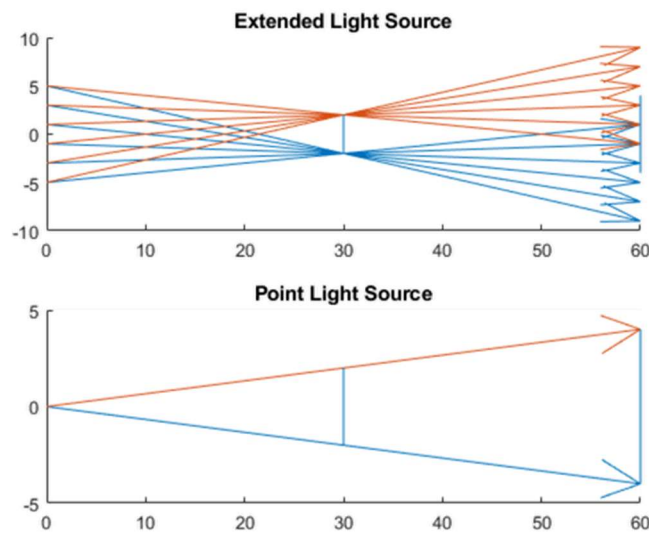
Previously, the light source has been used without any form of focusing as an extended light source. This greatly reduces the ability of the Schlieren optics to focus and produce sharp images. Adding a cardboard tube with thick paper stock and a pinhole in it as shown in Figure 37 allowed the light source to be focused on the mirror, reducing the amount of image ghosting and increasing sharpness.



**Figure 37 - Green Light source with pinhole**

To understand why the light source needs to be focused to a point, one needs to compare the way that a shadow forms from a point light source compared to that of an extended light source. This is done in the MATLAB plot in Figure 38; when a point light source is used, the edges of the shadow are sharp due to the light originating from a

single point, passing the edge of the object and then converging on a point in line with the light's origin and the object's edge. However, when an extended light source is used, the light does not originate from a single point. This means that for the same point along the edge of the object, there are many different angles in line with the light source. This in turn creates areas of overlap, known as penumbra, at the edges of the shadow, turning what should be a sharp line into a blurred edge.

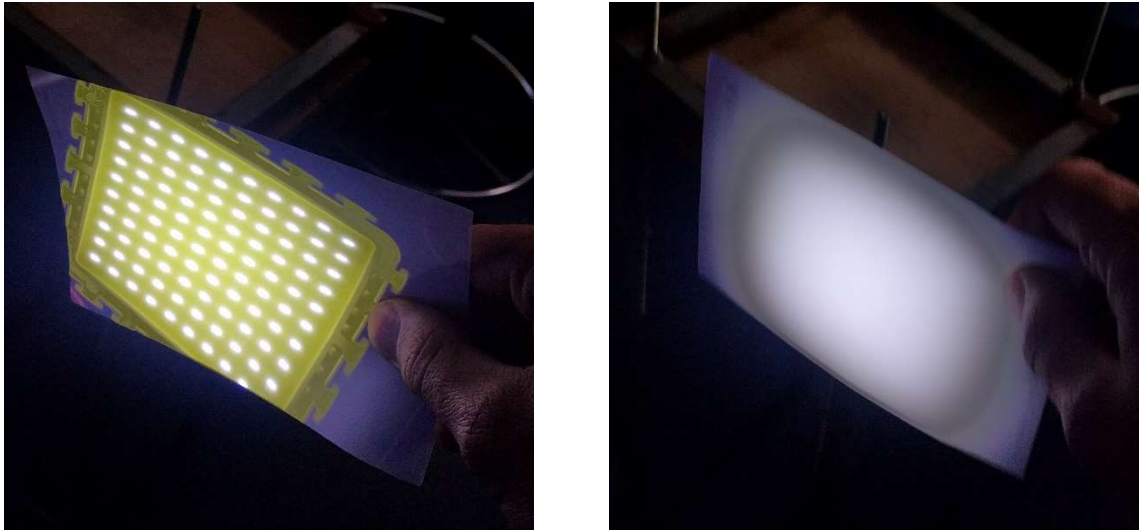


**Figure 38 - Comparison of Extended and Point Light Sources**

#### **4.3.1 White Light Source for Colour Schlieren**

For colour Schlieren images, a white light source was required so that the red blue and green wavelengths could be separated out. To do this, a cheap high power white light LED was chosen, rated at 100 W and only costing \$8.50 USD apiece. Similar to many high-power LEDs, including the CBT-120, the 100 W white LED is made using a chip on board (COB) design. This means that the LED is not a single LED but many smaller LEDs joined together.

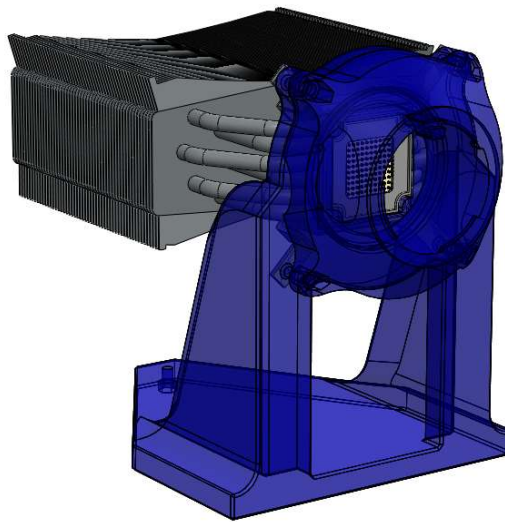
The COB design of the 100 W white led means that the illumination from the light source is not even across the field of view. Using diffuser material from a LCD screen supplied by Navico greatly reduced this problem. After the diffuser, a lens and pinhole was used to focus the light again; the effect of this can be seen in Figure 39.



**Figure 39 – Using a diffuser on the light source before (left) after (right)**

To keep the LED cool allowing for longer run times than the previous green light source, a passive computer CPU heatsink with much higher cooling performance was chosen. This heatsink allows for much better cooling by using heat pipes to allow for heat to move from the back of the LED out to the large area of cooling fins. The use of a fan could greatly improve the cooling ability of the heatsink, however, it was kept passive to minimize vibration caused by the fan being out of balance, and disturbances to the air that could be seen by Schlieren optics.

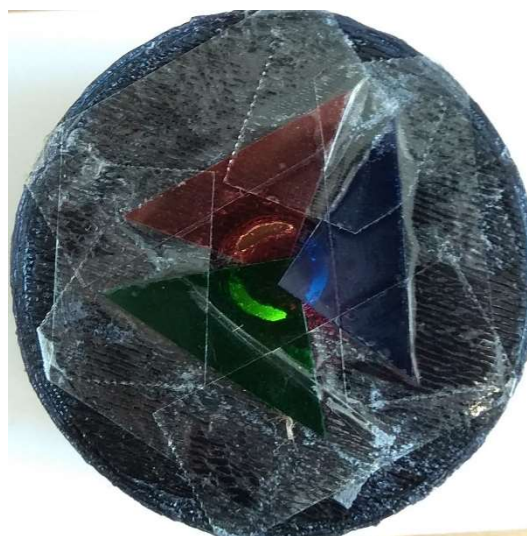
The LED was mounted in a 3D-printed stand shown in Figure 40 together with the heatsink. The stand is designed to be printed without overhangs to minimize the use of support structure. It also features a lens mount on the front that is compatible with a Minolta A-Mount lens that is used for focusing the light into a more intense beam and a screw at the rear for fine adjustment of the angle for the light beam.



**Figure 40 - Rendering of the LED stand and heat sink**

The colour filter shown in Figure 41 was 3D-printed to screw into the front of the lens in place of the pinhole to the same principle as the ‘Round Dissection filter’ developed by Gary Settles (Settles, 2001) mounted to the front of the focusing lens.

The sizing of the slots in the filter are identical to that used by Ting and Chen in their promising detection of very small LPG leaks (Ting & Chen, 2013). The colour filters are made from photographic flash filter material layer to give more colour saturation than what Ting and Chen achieved.



**Figure 41 - 3D-printed round dissection filter**

### 4.3.2 Knife Edge

The knife edge supplied with the Edmund Optics kit was very hard to focus. This was found to be due to the blunt edge of the aluminium plate used instead of a sharp edge. The blunt edge of the plate unevenly obscures some of the beam of light that returns from the mirror shown in Figure 42.

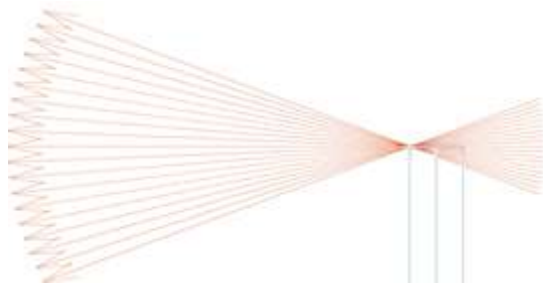


Figure 42- Blunt Knife Edge

With a sharp edge, the focal point of the returning beams of light that were not affected by inhomogeneities are able to be cut-off evenly. This is demonstrated in Figure 43.

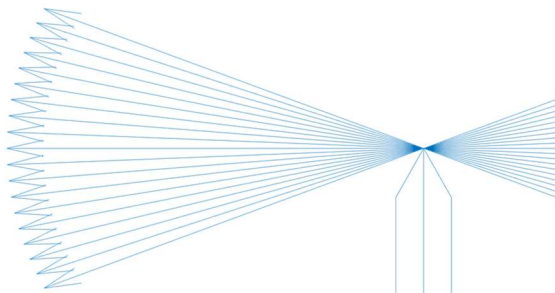


Figure 43- Sharp Knife Edge

### 3-D-printing stand for a disposable knife blade cut-off

The original stand from the Edmund Optics kit was not very stable because it was made with 4 small feet. These feet were not perfectly level, so at any one time only three of them were in contact with the bench. With the mass of the stand balanced over two of them, someone walking down the hall beside the lab was enough disturbance to cause the stand to oscillate between different feet being in contact.

To reduce the chance of oscillation caused by outside excitation, the new stand was designed with three points of contact, spaced further apart. Because of the large

spacing of the feet, the stand was designed so that the legs can fit around the camera mount without interference; a rendering of stand is showed in Figure 44.



**Figure 44 - Rendering of 3D printed knife edge stand**

Taking into consideration that Fused deposition modelling (FDM) 3D-printing is limited to overhang angles of up to approximately 45 degrees without support material, the stand was designed to be printed in a shape and orientation that conserved the use of plastic and printing time.

The area in which the blade was housed was designed in such a way to minimise the chances of users being able to cut themselves by only having a small area of blade exposed. The stand was originally made to hold a standard Stanley utility knife blade horizontally at the height of the centre point of the mirror in the same way as the knife edge supplied in the kit. Upon use of the stand, it was found that fine adjustment of the cut-off was much easier with the blade held at 45 degrees shown in Figure 45. Cut-off adjustment was then achieved by sliding the whole stand perpendicular to the light path.



**Figure 45- Blade mounted in the stand at 45 degrees**

### **4.3.3 Beam Splitter**

The addition of a beam splitter at the light source changes the off-axis single mirror Schlieren assembly to a single mirror coincident Schlieren assembly. This has the advantage of removing the off-axis alignment of the single mirror Schlieren assembly, and in doing so, removes off-axis optical aberrations.

The two most common variations of beam splitters are half-silvered mirrors and cube beam splitters. Half-silvered mirrors are significantly cheaper, but they can be optically hindered by off-axis internal reflection. Cube beam splitters avoid this issue by having the outer layer of glass normal to the beam that is being split, but they are much more expensive, with cheaper models costing hundreds of dollars. Because of its low cost, a half-silvered mirror was originally selected with the intention of replacing it with a cube beam splitter if aberrations were noticeable, however the change to a cube beam splitter proved to be unnecessary. The beam splitter was mounted in a 3D-printed base shown in Figure 46, with three threaded holes in the base so that screws can be used for angular adjustment.



**Figure 46 - beam splitter and 3D printed stand**

#### **4.3.4 Colour Schlieren**

As discussed in Section 2.1.2, the use of colour Schlieren optics is attractive as it shows promise to make disturbances in test section easy to detect by the human eye, due to showing a change in colour instead of just a change in light intensity. To test colour Schlieren, a high power white LED purchased with a greater colour spectrum allowing for both colour and monochrome Schlieren optics to be tested. The colour filters can be quickly added by use of a clip on Round Dissection filter that can be swapped out for a clip-on pinhole for when monochrome Schlieren is used.

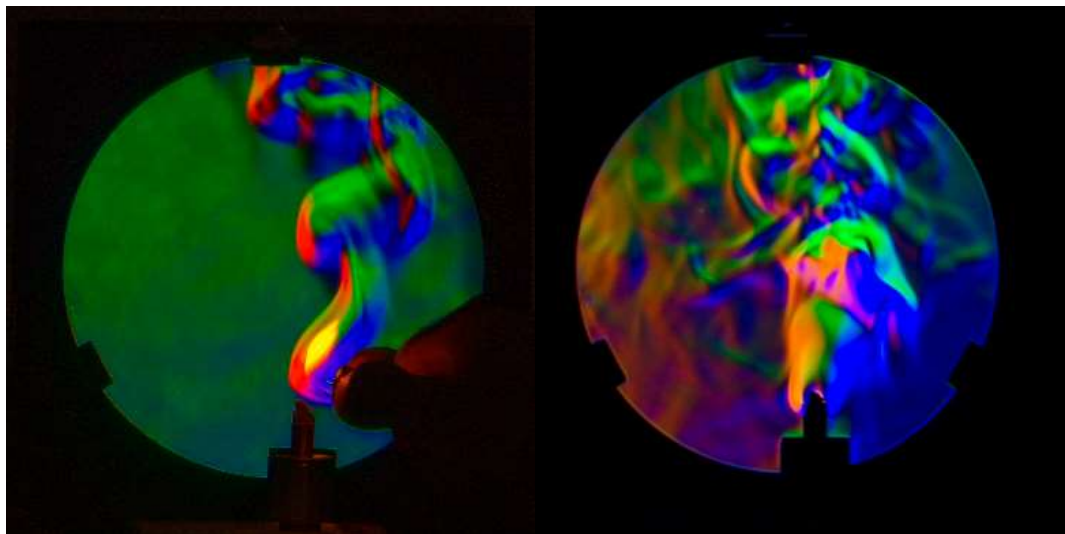
The clip-on filter shown in Figure 47 uses the existing bayonet mount that the lens hood would normally be connected to. The filter uses red, green and blue gel filters cut from filters used for photographic flashes. The strength of each filter can be adjusted by layering multiple filters of the same colour on top of each other - this allows each colour to be adjusted individually to maintain a balance of the intensity for each colour in the Schlieren image.





**Figure 47 - Colour filter on light source**

Initial setup of the colour Schlieren optics was done with the help of a small spirit burner shown in Figure 48. All three colours can be seen from large disturbances such as that from the convection generated by the heat of a flame giving a very vivid and colourful image.



**Figure 48 - Lighting a small spirit burner and then blowing it out imaged using double pass Schlieren with colour filter**

Difficulties were encountered when adjusting the round cut-off that sits in front of the camera and lens. After some experimentation it was found that using the manual aperture of the Soligor 135 mm lens as an adjustable diameter cut-off was much easier to align, giving better sensitivity.

Figure 49 shows the aperture of the lens at the focal point of the mirror. The three independent colours come into focus, and the aperture of the lens should be centred in the dark patch between the three colours (here it needs to be moved towards the green).



**Figure 49- Adjusting the three colours for the Round Dissection filter**

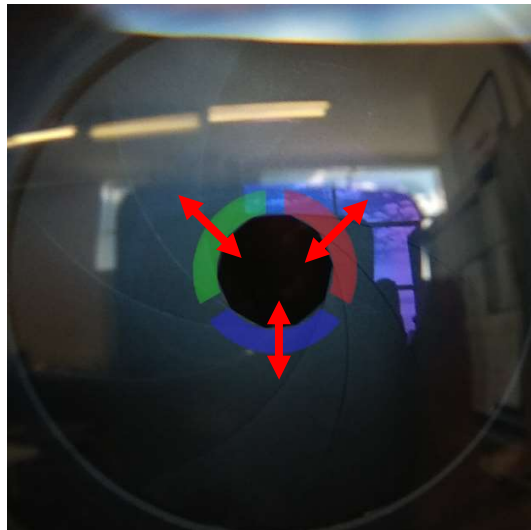
Once larger disturbances could be detected, the assembly was fine-tuned on a small container that contained methylated spirits. As the methylated spirits evaporated, the vapour could be seen as a small purple plume (Figure 50). However, it was very hard to accurately adjust the colour filter to a high enough accuracy to maintain a constant background colour.



**Figure 50 - Methylated spirits evaporating from a small container**

### *Results from colour Schlieren*

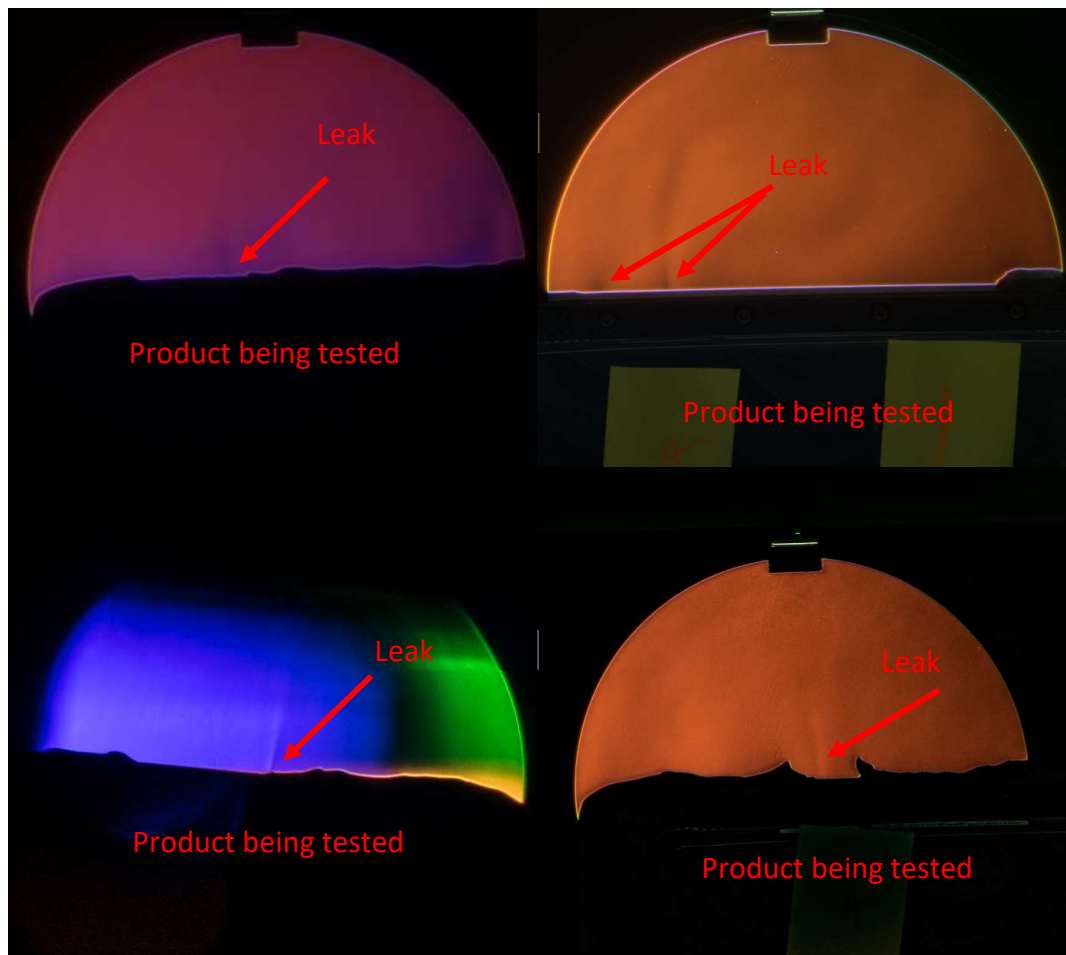
Following the calibration of the colour Schlieren optical assembly on larger disturbances, the next logical step was to test out colour Schlieren on the leaking enclosure. With fine adjustment of the position of the lens and camera, leaks could be seen, however it was much more difficult to achieve high sensitivity as the images returned by the setup deteriorated in sensitivity and sharpness with the slightest misalignment of the cut-off for any of the three colours as well as cut-off hole size. Figure 51 shows an overlay of the RGB colour pattern on the aperture diaphragm of the Soliger 135 mm. The arrows show how each colour can individually be adjusted; because of the extra 2 degrees of adjustment, it is far more complex to adjust the cut-off of 3 colours than it is to adjust the single knife edge of monochrome Schlieren.



**Figure 51 - Colour Schlieren cut-off: the three colours need individual adjustment**

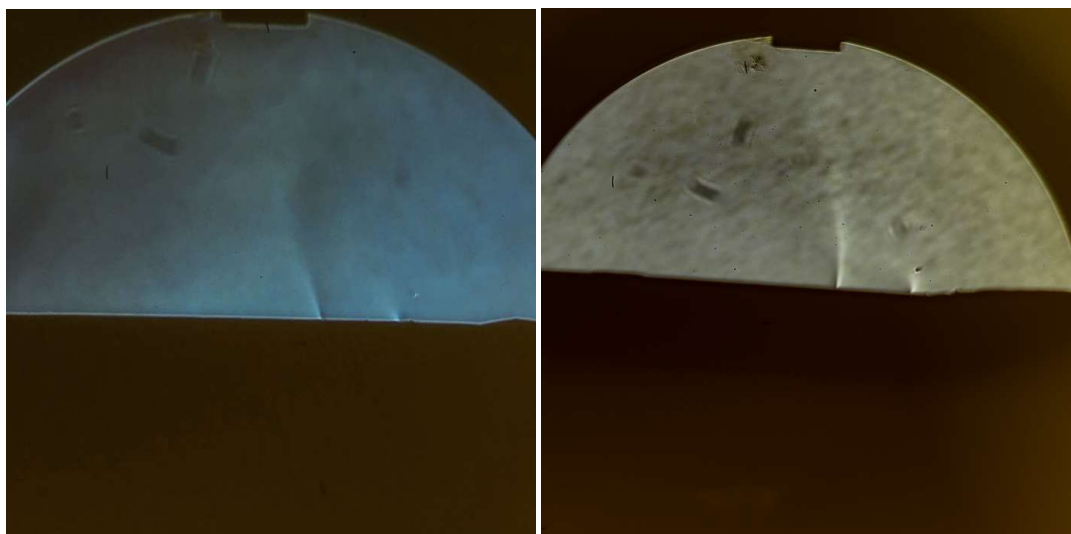
### *Comparing colour Schlieren optics to Monochrome Schlieren optics*

The results from the colour Schlieren images in Figure 52 show that leaks can be identified but, when compared to monochrome Schlieren images, they lack sharpness. This is clear when they are compared to the images in Figure 53, taken shortly afterwards with the only change to the optical assembly being the exchange of the colour filter for a pinhole. The difference in sharpness could be due to the colour filter increasing the area of the light source in effect, causing the filter to act like an extended light source.



**Figure 52 - Leaks with Colour Schlieren with different adjustments of cut-off**

The disturbances from the leak are small, so only a change in light intensity is seen instead of a change in colour, as was observed in the tests with larger disturbances from the burner in Figure 48.



**Figure 53 - Leak 4 & 5 with Monochrome Schlieren (right) show much clearer results than colour Schlieren (left)**

## 4.4 Refining the Schlieren Optical Setup for Leak Detection

The Monochrome Schlieren optical assembly showed the potential to detect leaks in one of Navico's products. This warranted further exploration into the use of Monochrome Schlieren optics for leak detection. This was carried out by investigation into different improvements to the optical assembly to increase sensitivity.

From the MATLAB ray tracing results, the sensitivity of the optical assembly relies on accurate alignment of each optical component as well as fine-adjustment of the knife edge for the required sensitivity level. For best results, as close to a point light source as possible should be used.

### 4.4.1 Finding the Appropriate Lens for the Schlieren Optical Assembly

The camera used throughout the experiments was a full-frame Sony A7 camera combined with a very old manual focus Soligor 135 mm lens. The lens mount that the lens had was not suitable for the Sony FE lens mount, so a M42 Lens mount to Sony Full Frame E-mount (FE) adaptor was used.

The Soligor 135 mm lens had a too short focal length to give a view that concentrates on the mirror - most of the picture was of the blank background surrounding the mirror (Figure 54), resulting in the need for a lot of cropping, which caused the area of interest to be of low resolution.

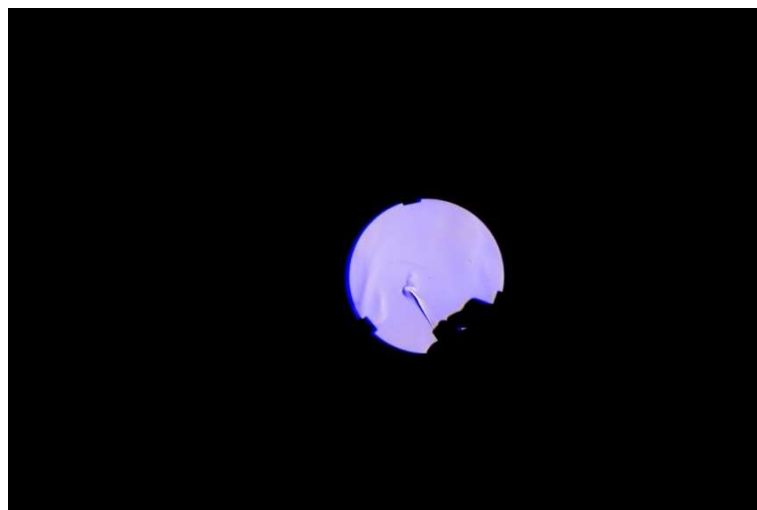


Figure 54 - Image taken with the Soligor 135mm

The required focal length of the lens to match the field of view of the mirror can be calculated knowing the camera's sensor dimensions. As the sensor is wider than it is high, the height is used to give minimum field of view. In the case of a full-frame camera such as the Sony A7, the sensor height is 24 mm. This means that the lens' vertical field of view should be 2.86 degrees and that its focal length should be 480 mm, as calculated in Appendix B.

Unfortunately, lenses with a focal length greater than 200 mm are normally reserved for specialist sports and wildlife photography, and are uncommon for normal photographic use. This makes them hard to find; the most common lens with a focal length longer than 135 mm is the 70-200 mm zoom lens, available in a range of makes and apertures. Two 70- 200 mm zoom lenses were hired, one being the Canon 70-200 f/2.8l adapted to the Sony FE lens mount with a Metabones speed booster 0.71x, making the equivalent focal length 140 mm with an aperture of f/2.2. This lens was tested because it was the longest focal length available. Unfortunately, with the adaptor available, the maximum focal length was only 140 mm. To account for this, the camera was used in aps-c mode that automatically reduces the used area on the sensor to 22 by 15 mm, giving a full frame equivalent focal length of 227 mm. This is calculated in Appendix B.

The next lens tested was a Sony FE70-200 mm F/2.8 G-Master zoom. This lens could use its full focal length on the Sony A7 camera body, resulting in a slightly tighter crop of the test section. This lens was also used to test out the performance of autofocus on a Schlieren optical setup; the autofocus on the camera failed to achieve focus, even when the cameras focus points where selected on the high contrast region where the frame holds the mirror. The Sony lens also showed a blue tinge around the edges of the mirror (Figure 55) when tested at some focal lengths below 200 mm. This is suspected to be due to coating on the lens to reduce optical flaws, such as sun flare, during normal photographic use.



**Figure 55- Crop from the Sony 70-200 mm shot at 151 mm showing blue fringing**

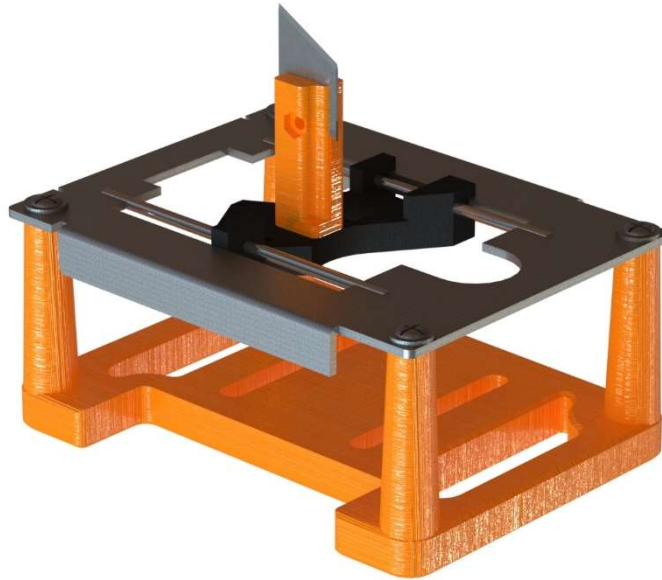
Of the lenses tested, the most repeatable in focusing and sharpness was from the fully manual focus 135 mm originally tested. The issue with the other two lenses was that autofocus was not able to operate at all and, instead of focusing on the test area, chose to focus on the background behind the mirror, even when the focal point was set on the mirror bracket or the enclosure being tested. The two autofocus lenses could focus when switched over to manual focus mode, however, the throw of the focusing ring was very short (less than a full turn) making fine focus adjustment very hard to achieve.

#### **4.4.2 Automating the Knife edge and Remote Camera Shutter**

With the first generation Double Pass Schlieren optical assembly, adjustment of the knife edge proved to be a very tedious task. To improve the repeatability and ease of adjusting the knife edge cut-off adjustment, some form of linear rail was needed. Initial concepts included the use of a manual linear rail used for macro photography. At the time, these concepts were being worked out, four partially disassembled Digital Versatile Disc (DVD) drives were acquired. Of these four, two drives used a smaller stepper motor to move the sensor along a pair of linear rails. For each step of the motor,

the linear slide moves 0.4 mm. With 8 bit micro stepping, the slide can be controlled in increments of approximately 0.05 mm.

Using two 3D-printed parts, the knife can be mounted onto the sliding assembly from the DVD drive and the sliding assembly is then able to be mounted onto the base of the Schlieren assembly via a 3D-printed base shown in Figure 56.



**Figure 56 - Solidworks rendering of the DVD drive sliding assembly**

Control of the knife edge is achieved with the use of an Adafruit Motor Shield V2 shield on an Arduino mega 2560, using the MATLAB Support Package for Arduino. This simplifies the writing of a user interface to control knife edge position. The user interface is shown in Figure 57, and the source code can be found in Appendix A. The use of the Adafruit motor shield also opens the ability to control other motors and servos, which means that an infrared camera trigger can be controlled via the servo port to take images at each movement of the knife edge.



## HSR Test

Choose port, center the knife edge them hit start to test hdr

Arduino connection

Port ▼

connect to Arduino

Refresh Ports

Knife start position (steps) 0

Camera setup

images 10

Delay(s) 1

steps per image 1

camera test

Turntable Setup

Steps 10

Total Angle Range 5

Turntable position (steps) 0

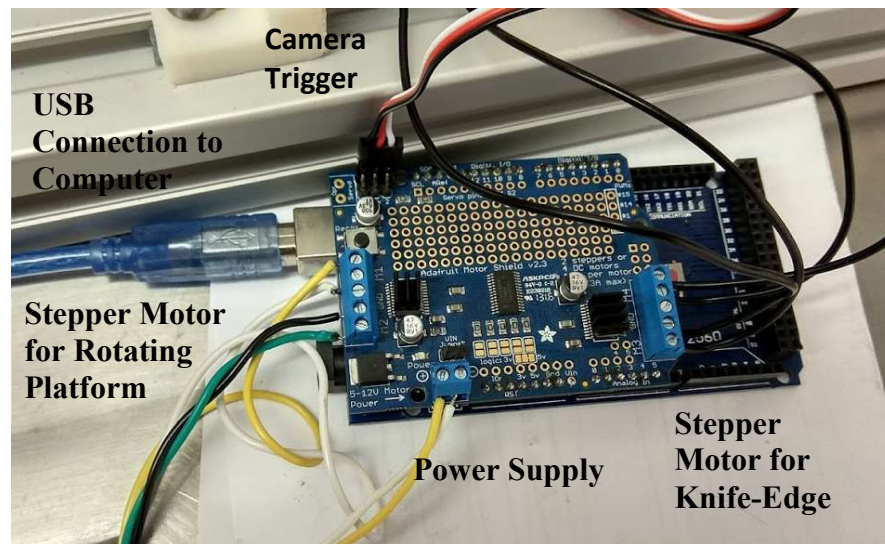
Turntable position (deg) 0

start

**Figure 57 - User interface for control of the rotating base and camera**

### 4.4.3 Rotating Platform

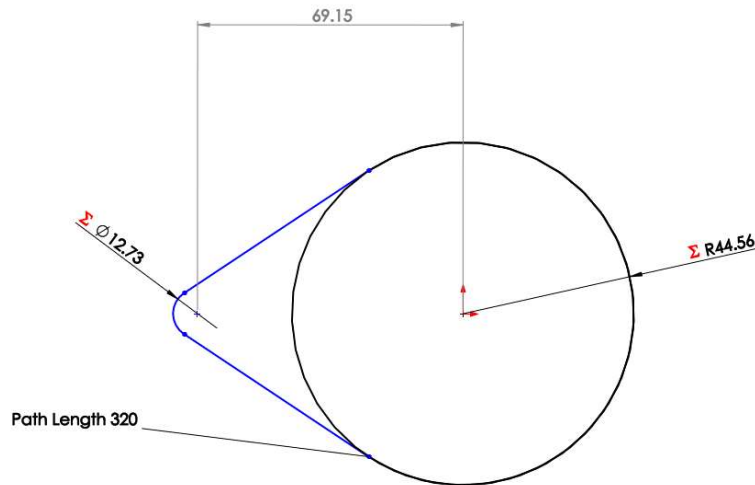
Schlieren optics gives a 2D view of the enclosure that is being tested. To pinpoint the location of the leak in 3D space, multiple views are needed. Manually moving the enclosure for each image consumes a lot of time and disturbs the air around the test area, meaning that one must wait for the air to settle before taking the next image. Using a motorised platform to move the enclosure to different orientations reduces disturbances that would otherwise be created by an operator moving the enclosure, it also allows for more precise adjustment of angle. To control the motor on the platform, the spare stepper motor port on the motor driver can be used as shown in Figure 58.



**Figure 58 - Arduino Mega and Adafruit Motor Driver wiring**

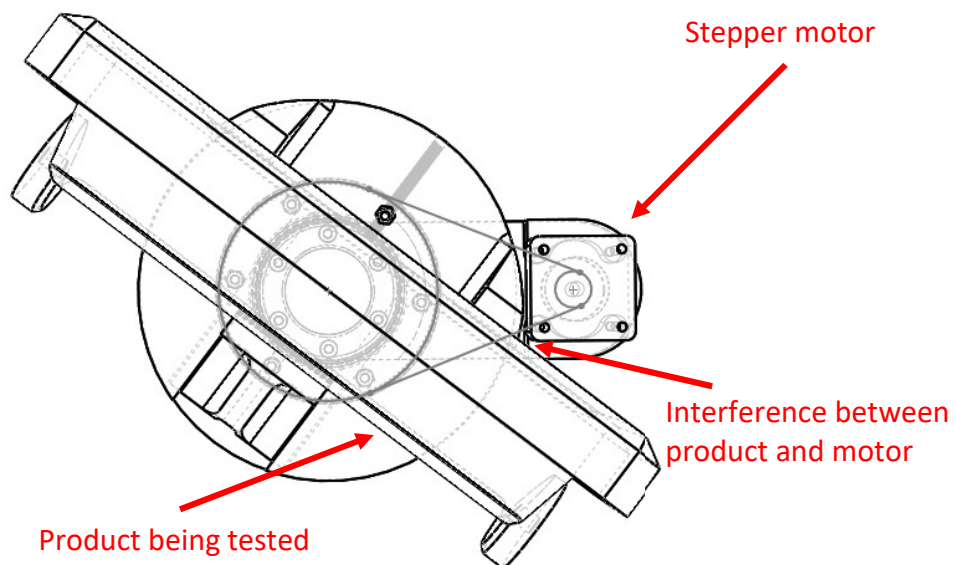
A small stepper motor, GT2 belt and pulley were utilised from a previous personal project. The motor is an National Electrical Manufacturers Association (NEMA) 14 stepper motor with a rated voltage of 5 V and current of 0.8 A, the belt is a 160 tooth GT2 belt and the pulley that fits the motor has 20 teeth.

To design the second pulley and clamping assembly, a Solidworks sketch shown in Figure 59 was used to show the driven pulley size and its effect on clearance of the motor. By varying the tooth number on the driven pulley, the whole Solidworks assembly could be updated to show motor clearance from the platform. The rotating platform was sized so that it could clamp onto the enclosure being tested in both portrait and landscape orientations.



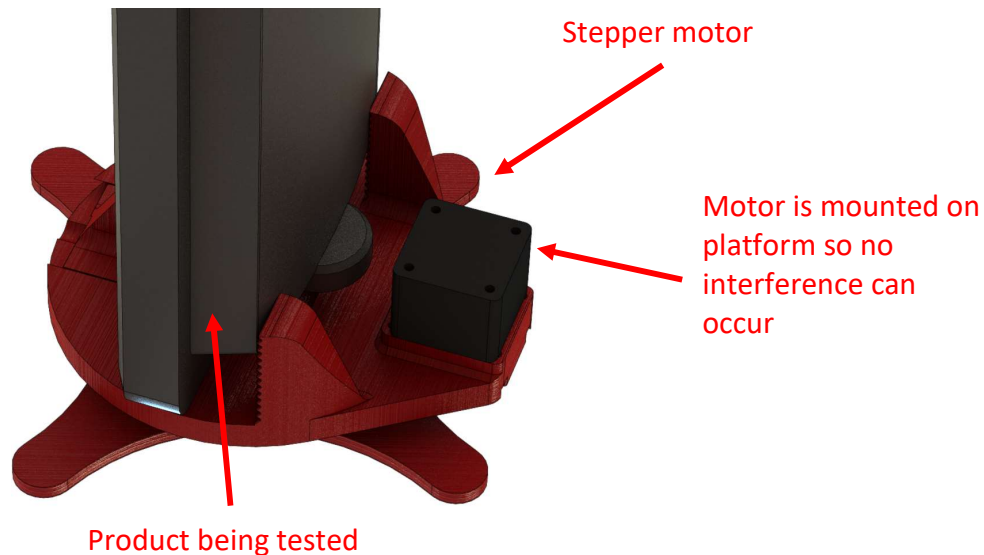
**Figure 59 - Equation-driven sketch of the belt and pulleys**

The first design iteration of the rotating platform had the stepper motor attached to the base of the assembly; a slew bearing was designed to be combined with the driven pulley and uses common steel 4.5 mm (.177 calibre) airgun pellets.



**Figure 60 - Rotating Platform Design 1 top view**

A flaw in the first design iteration is that when the enclosure protrudes out too far from one end of the rotating platform, interference will occur between the enclosure and the motor at some angles as shown in Figure 60. In order to solve this, the motor was moved onto the rotating platform (Figure 61). So long as the rotation is kept lower than several rotations, an electrical slip ring is not needed, and the wires from the motor can be left to move with the platform.



**Figure 61 - Solidworks rendering of the rotating base with the multi-function display in portrait orientation**

In the next generation of the design, the centre distance was reduced between the two pulleys. With the motor on the rotating platform, the centre distance could be reduced. The limiting factor was the clearance between the motor and the mounting boss on the enclosure when it is mounted vertically.

The size of the driven gear was maximised to minimise the velocity fluctuation due to the discrete steps of the stepper motor that would cause excess vibration, which could affect the optical system. This also has the added advantage of increasing the torque capacity of the rotating platform with the increased ratio.

#### **4.4.4 Lens**

It was obvious from previous testing that a lens with a larger focal length was needed to match the lens' field of view to the size of the test section. Previous calculations from Section 4.4.1 found that a full frame equivalent focal length of 480 mm was needed to do this. Testing of two different autofocus lens found that autofocus performed very poorly for Double Pass Schlieren optics, while manual focusing achieved much more consistent focus; the longer focus throw of a manual focus only lens helped with fine-focus adjustment.

To meet these needs, a comparatively inexpensive Opteka 420-800 super telephoto lens was purchased with a T-mount to Sony FE adaptor. The lens has a fixed aperture size, meaning that the aperture is dependent on the focal length chosen; at 500 mm, the aperture is f/10, meaning that it has a 50 mm diameter. Most photographers would dismiss a lens like this as it does not let in enough light to allow a shutter speed fast enough to stop blurring when hand-held, but for this application it is fine due to the light entering the lens is limited by what the f/10 mirror reflects from the light source.

A comparison of the new Opteka lens to the old Soligor lens is shown in Figure 62. The field of view of the Opteka at its 500 mm focal length is much better at unitizing the full resolution of the image sensor.



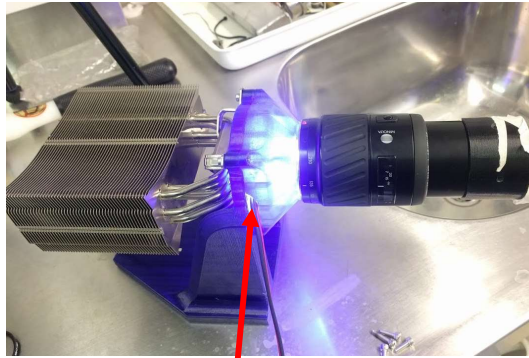
**Figure 62 - Comparison on the field of view of the Opteka 420-800mm at 450 mm (left) and the Soligor 135 mm (right)**

#### **4.4.5 Light Source**

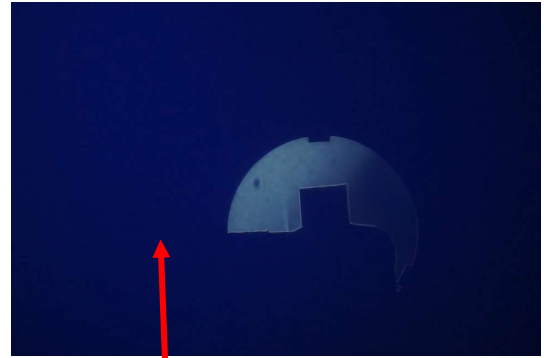
The original 3D-printed light source stand was printed in blue Polyethylene Terephthalate (PETG) filament. While it was strong and able to withstand the heat from the 100 W LED, it was also partially translucent. This meant that it created a strong blue background light that was visible in some images, especially when a light trap was not used.

The overall design of the first light source worked well to hold the lens steady as well as support the weight from the light source. This was kept the same apart from adding mounting points for use with the T-slot rail base. The major design change was moving to opaque white Acrylonitrile butadiene styrene (ABS) 3D-printing filament.

Unfortunately, the only colour available was white (ideally it should be black for greater absorption of the light spectrum), but it was still a big improvement on the PETG previously used. The transparent blue PETG plastic caused the entire room to be illuminated in blue; the effect of the on the images can be seen in Figure 63.



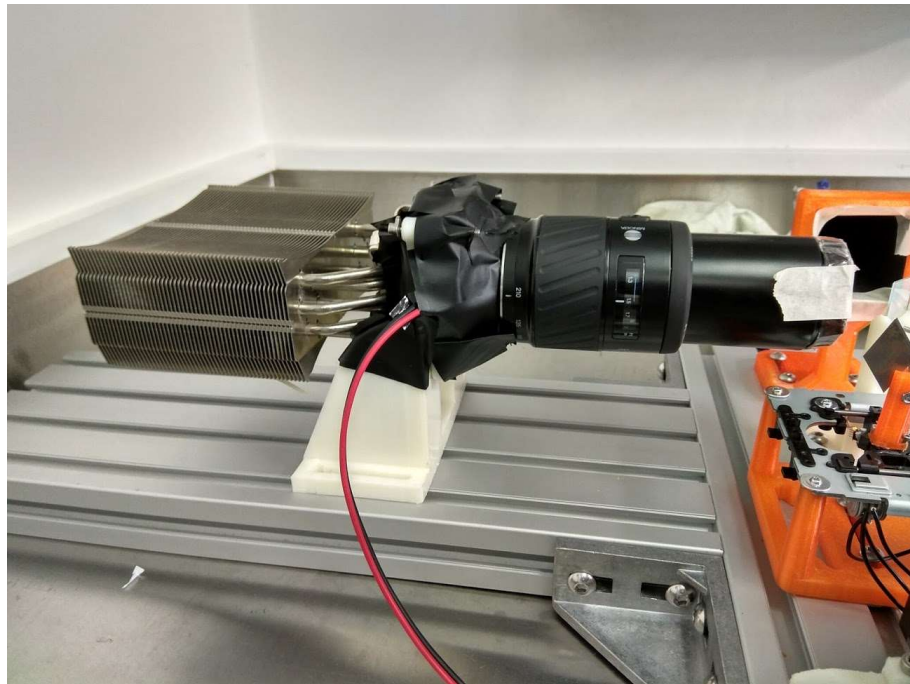
Blue PETG allowed light to escape the LED stand



Entire Schlieren image tinted blue from LED stand

**Figure 63 - Effect of the blue translucent LED stand on the Schlieren image produced**

Black tape was used to seal all the joints in the light source base where the LED is clamped and where the lens mounts on. This helped to get rid of most light leaks (Figure 64).



**Figure 64 - White ABS LED stand with black tape sealing light leaks**

#### **4.4.6 Optical Base**

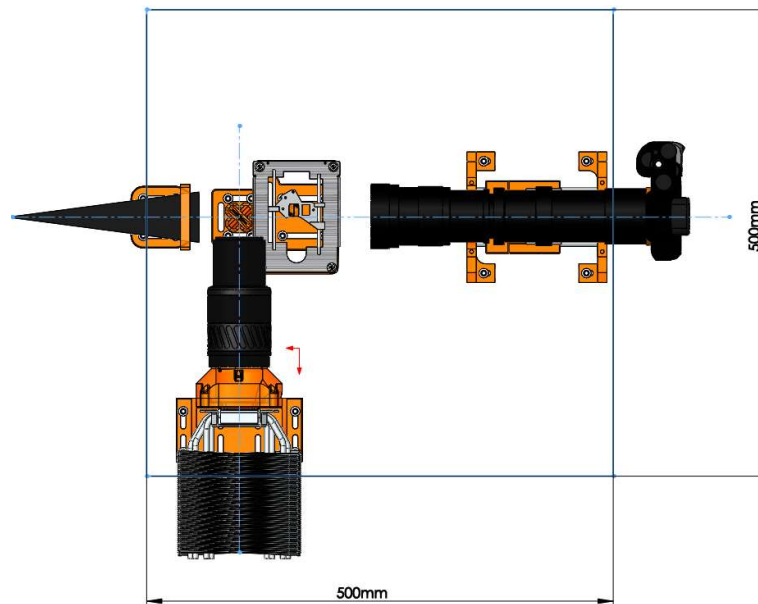
Alignment of the knife edge, camera and light source is important for Schlieren optics to function well and produce clear images. This becomes even more important when the added complexity of a beam splitter is introduced. Early testing with all the components on separate mounts on the bench top showed that the vibration from someone running down the hall next to the lab was enough to ruin this alignment. A base that allows for these components to be held in alignment in a more permanent manner greatly simplifies setting up the Schlieren optical setup between consecutive days of testing. To achieve this, it needs to be able to hold the camera, lens and light source perpendicular to each other so that a beam splitter can be used.

While there are commercially available optical bread boards available from optics manufacturers such as Newport and Edmund Optics, they have very high prices and are not available in New Zealand, which requires expensive shipping from overseas.

The area needed for all components, excluding the mirror, is approximately 500 mm squared. Ideally, the components should be placed on two rails set at 90 degrees to each other in a layout similar to Figure 65. This would allow for focal distances of the light



source and camera/lens to be adjusted while remaining in alignment with the beam splitter and knife edge.



**Figure 65 - Approximate size requirements for base and approximate rail path (dotted lines)**

#### Commercially available optical bases

Even though the use of a commercially available optical breadboard is unattractive due to price, some available products are discussed here for a quick overview of the available options and how they are assembled.

#### *Breadboards*

Currently available solutions for mounting optical components generally consist of the combination of an optical breadboard with rails mounted onto it to hold both rails in alignment. These components are available from Edmund Optics and Newport. They come in a range of thicknesses and are comprised of an aluminium or steel sheet with many holes drilled and tapped at regular intervals to allow secure mounting of optical components and rails shown (Figure 66). Optical components are then attached to the bread board with their own rail system for fine adjustment.





**Figure 66- Edmund Optics 13 mm thick aluminium breadboard (left) (Edmund Optics, 2017b), Newport 25 mm breadboard (right) (Newport, 2017b)**

These optical breadboards vary in price for a 500 x 500 mm square from the comparatively cheap Edmund Optics breadboard for \$325 USD excluding shipping (Edmund Optics, 2017b) to the more expensive Newport breadboard for \$542.30 USD excluding shipping (Newport, 2017b).

### *Optical rails*

Optical rails shown in Figure 67 are made to match the bread boards available from Edmund Optics and Newport. These cost \$239 USD per 900 mm length excluding shipping from Edmund Optics (Edmund Optics, 2017a) and \$112 USD per 600 mm length from Newport (Newport, 2017a).



**Figure 67 - Edmund Optics Dovetail Optical Rail (Left) (Edmund Optics, 2017a), Newport Optical Rail(right) (Newport, 2017a)**

### Alternative Optical Base design

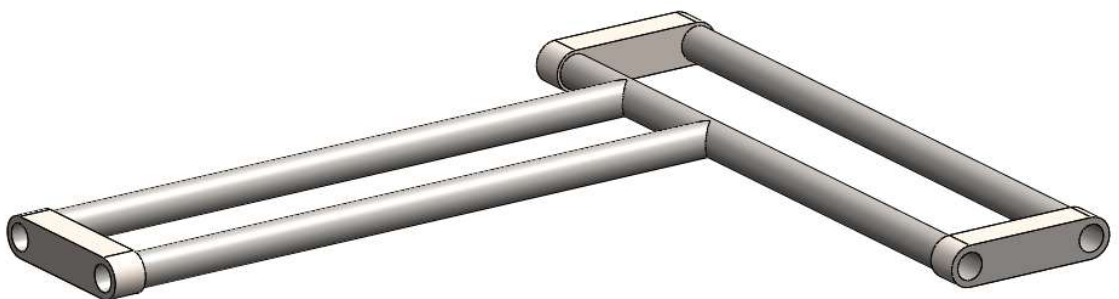
The commercially available optical bases from Newport and Edmund Optics offer an easy to use solution. However, their high price and expensive shipping costs to New Zealand are big drawbacks. The need of both a breadboard and rail system could be avoided with the use of an alternative design where the rails are the only components.

The following concepts use tube and later T-slot extrusion to provide the structure of the base as well as sliding attachment point for adjustment of the optical components. This reduces amount of material needed for the base which in turn reduces cost. An added advantage is the reduction in the footprint of the base so that the power supply can be kept closer to the light source.

#### *Concept One*

Concept one uses four pieces of tube as rails for the optical components to clamp on to. Joined at each end with a block, the two set of tubes would be joined at a 90-degree angle as shown below. The joint between the two sets of rails could be bolted or welded together, or some form of clamp could be used so that the distance that they are joined at could be adjusted.

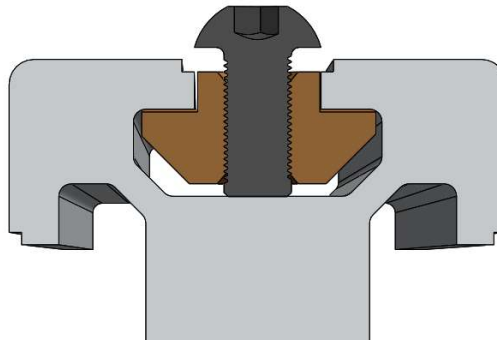
The downfalls of this design are that it is difficult to make it torsionally rigid at the connection between the two sets of rails because of the complexity of cutting and joining tubes perpendicularly. The connecting rails could extend through the other set, but this would make it difficult to clamp on components in this area.



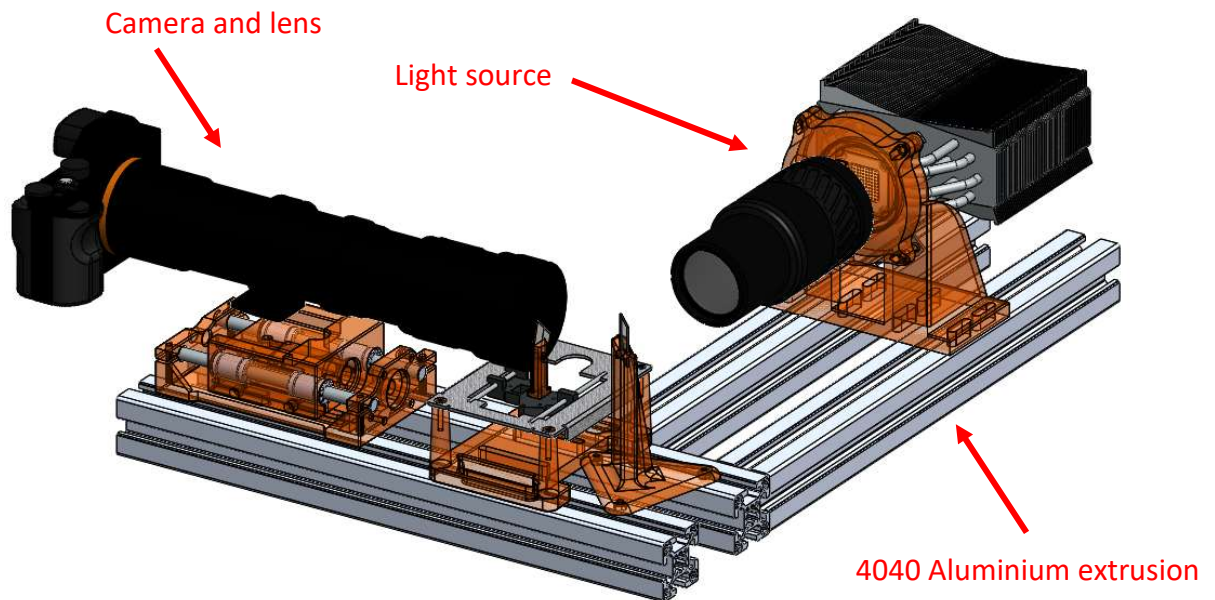
**Figure 68 - Concept one, using pipe for optical rails**

### *Concept Two*

Replacing the tubes from concept two with 4040 T-slot prototyping extrusion as shown in Figure 70 greatly simplifies mounting of the optical components, because T-slot nuts shown in Figure 69 can be added to the extrusion at any distance along it, making it very versatile for testing out different optical components. When the bolts are not tensioned, the nuts are able to slide, making it possible to carry out adjustments as are needed for different lenses with varying focal distances. T-slot extrusion also makes joining the two sets of rails together much easier, because the flat sides can be mounted together with the use of corner brackets, shown in Figure 71.



**Figure 69 - Solidworks rendering of T-Slot**



**Figure 70 - Base Made with 4040 prototyping extrusion**

### *Refinement of Concept Two*

Concept two can be simplified and made a lot more rigid by changing the four pieces of 40 mm T-slot extrusion to two pieces of 40 x 160 mm extrusion with two 40 x 80 mm corner brackets as the joint between the two extrusions. The extra two T-slot channels gained by using the larger extrusion gives more room for mounting components.



**Figure 71 - OnEquip 40 x 160 SlotPro base with 40 x 80 corner brackets**

Using 40 mm x 160 mm T-slot extrusions, the base can be constructed from parts available in New Zealand for substantially less cost than commercially available optical bases. The cost for 1 m of extrusion is \$150 NZD and the corner brackets, T-slot nuts, bolts and shipping bring the entire material cost for the base to \$218.20 NZD. The combination of the Edmund Optics rails and bread board would have cost closer to \$800 NZD, plus shipping.

#### 4.4.7 Light Trap

A disadvantage of using a beam splitter is that a small amount of light that should pass through the half-silvered mirror is reflected in the opposite direction to the camera as shown in Figure 72. This means that whatever is directly in front of the camera's field of view becomes illuminated and shows up in the images taken. To reduce this effect, a black body that absorbs light can be placed behind the beam splitter to collect this beam. To simulate the effect of a black body, a simple cone shaped light trap was made using a piece of black card folded in a way that achieves a fine angle.

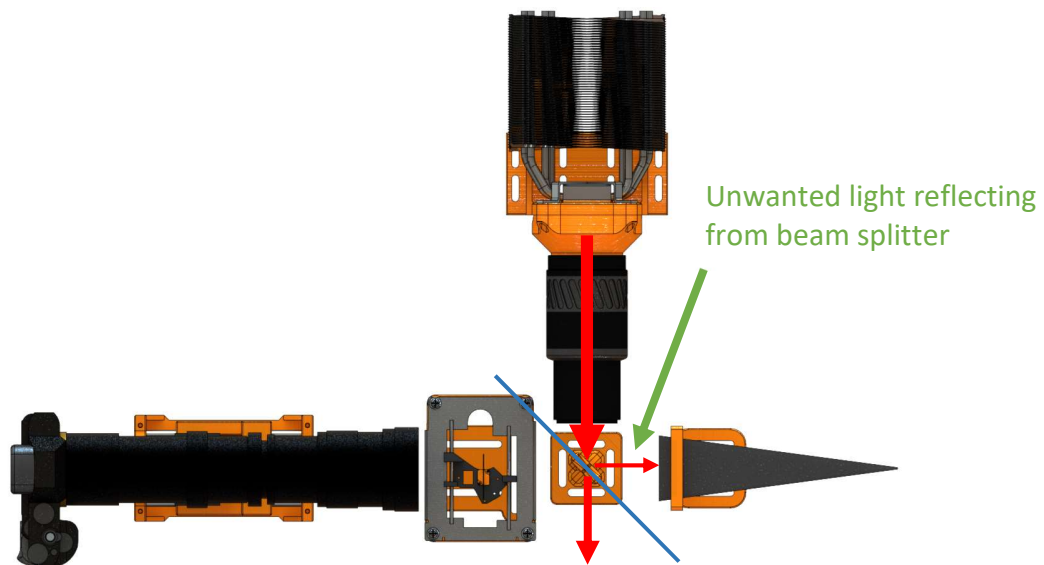


Figure 72 - A fraction of light hitting the beam splitter will be reflected the wrong way (small red arrow)

The idea behind the cone shape is that light entering the cone will partially be absorbed by the black card walls. The light that is not absorbed will be repeatedly reflected deeper into the cone to finally be absorbed; this is demonstrated by the blue arrow in Figure 73.

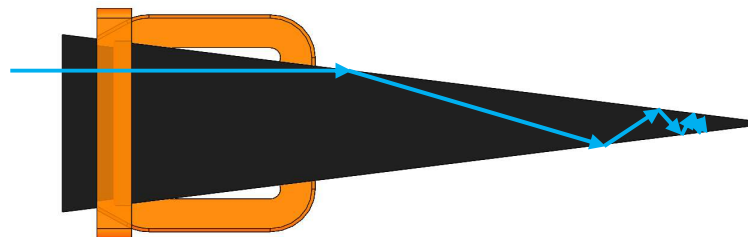


Figure 73 - Light reflecting deeper into the light trap

The effect of the light trap was found to be significant in improving the clarity and contrast of the images returned by the Schlieren optical setup. This is shown in Figure 74, where the two raw images are taken one after the other with the only change being the removal of the light trap.

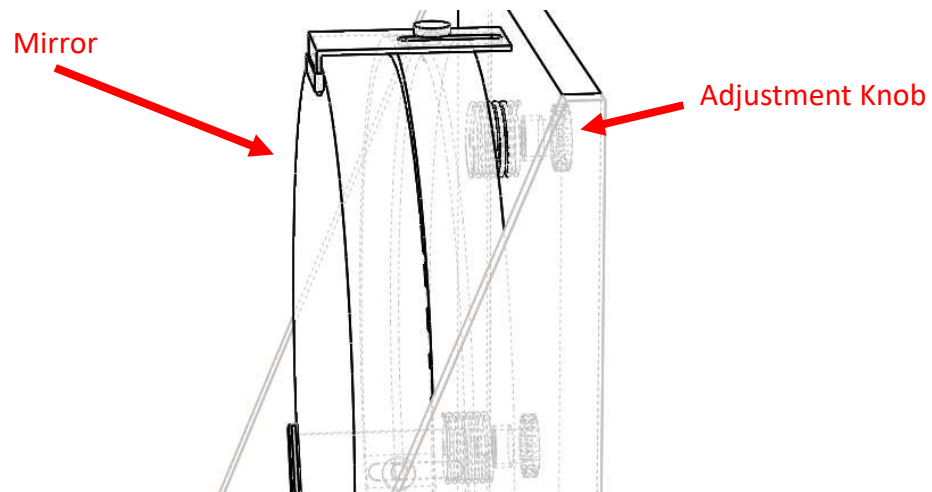


**Figure 74 - With light trap (left) without light trap (right)**

#### **4.4.8 Mirror Base**

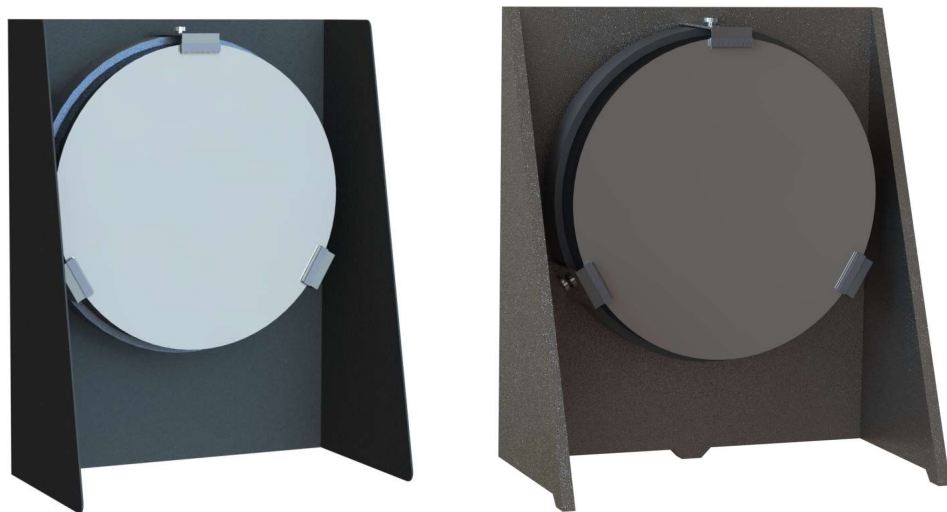
The mirrors supplied with AUT's Schlieren optical kit from Edmund Optics comes with steel bases made from 1 mm thick steel sheet folded at each side to make the legs. Unfortunately, this proved to be a particularly unstable way to hold the mirrors, as both the stands with AUT's kit were slightly warped so that when they are on a flat bench they oscillate with the slightest excitation.

To remedy the unstable mirror stand, a new one was made by AUT's Mechanical Workshop out of mild steel plate offcut. The centre piece was from a square of 8 mm plate and the sides are from 6 mm plate. A steel plate was chosen over 3D-printing because of its high mass and good vibration damping properties, as well as being thin enough to allow the use of the mirrors' existing adjustment system as shown in Figure 75.



**Figure 75 - Spring loaded adjustment knobs**

The corners were cut as per Figure 76, so that there were only 3 points of contact to stop any rocking.



**Figure 76 – Original mirror stand (left) Improved mirror stand with 3 contact points (right)**

#### **4.4.9 High Sensitivity Range imaging (HSR)**

One downside to using a knife edge cut-off for Schlieren optics is the limited range of sensitivity at any given knife edge setting, meaning that when a large amount of knife edge cut-off is used, detail is lost from the inhomogeneities that were visible when less cut-off was used. Settles recommends a cut-off of 50% for minimising over and underexposure of Schlieren imaging (Settles, 2001, p. 61).

At the time that Settles wrote his book on shadowgraph and Schlieren imaging, the concept of combining multiple images was relatively unheard of, with the technique of high dynamic range imaging only being patented in 1998 (Mann, 1998). Widespread use of automatic image stacking was not widely available until Adobe Systems added merge to HDR to photoshop cs2 in 2005 (Adobe Systems Incorporated, 2005).

Modern use of image stacking has escalated with the advancement of processing power available. Even phones today commonly stack many photos every time a single photo is taken for noise reduction and improvement of dynamic range (Levoy, 2014).

Inspired by modern high dynamic range imaging, the use of a similar method for combining multiple Schlieren images was developed, instead of achieving a high dynamic range. The modified approach allows the creation of high sensitivity range images via the combination of multiple Schlieren images with different knife edge settings.

To capture a range of images with different knife edge cut-off settings, the automated knife edge slide was used in combination with the MATLAB user interface.

The user interface shown in Figure 77 includes controls for establishing a connection with the Arduino controller, setting up the number of images to be taken, and the distance that the knife edge is to be moved between each image. This also allowed for two knife edges to be used so that the light can be cut off in two angles, giving a more complete view of the inhomogeneities.

The user interface also includes control for moving the rotating platform so that many high sensitivity range images can be taken from multiple angles, and a complete view of all the leaks and their location can be gathered from a single button click.



### HSR Test

Choose port, center the knife edge then hit start to test hdr

Arduino connection

Port   ▼

connect to Arduino

Refresh Ports

Knife start position (steps) 0

Camera setup

images 10

Delay(s) 1

steps per image 1

camera test

Turntable Setup

Steps 10

Total Angle Range 5

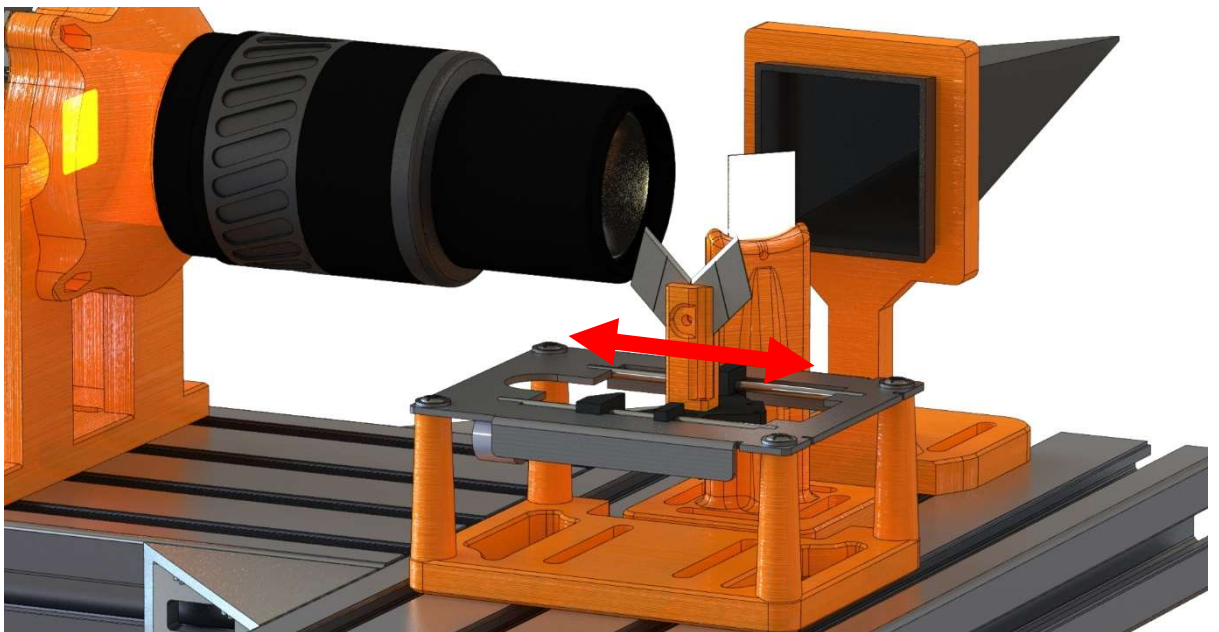
Turntable position (steps) 0

Turntable position (deg) 0

start

**Figure 77 - MATLAB GUI for High Sensitivity Range imaging**

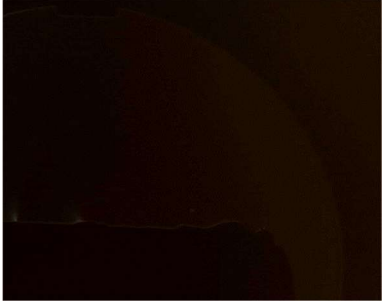
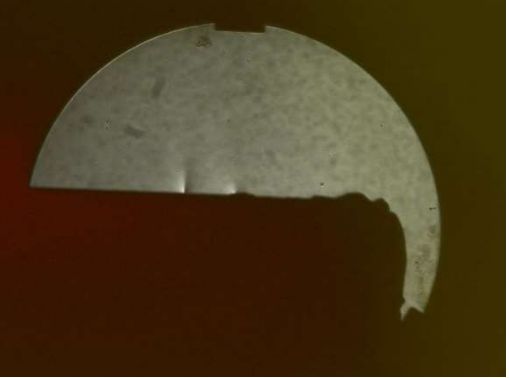

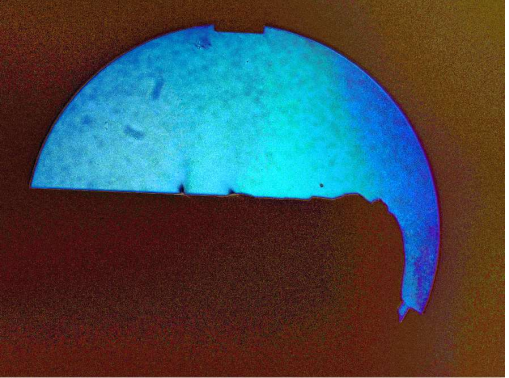

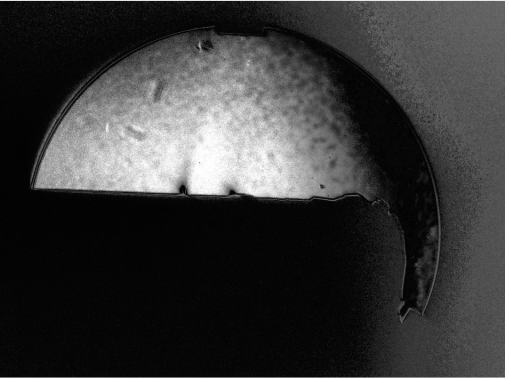

The red arrow in Figure 78 shows the movement of the knife edges. Only one knife edge is in cut-off with the returning beam of light at once so the slide must move from one blade in full cut-off to the second blade in full cut-off.



**Figure 78 - Movement of the two knife edges. Note a pinhole was normally used in front of the light source lens**

Table 2 shows the combination of four input images with different knife edge cut-offs combined, using both Adobe Photoshop and MATLAB. The resulting images on the right show much more detail of the leaks than uncombine input images.

**Table 2 – HSR Image combination**

|   |  |
|---|--|
|    |    |
| <p><b>High sensitivity 100% cut-off<br/>input image</b></p>                         | <p><b>Output image from combined images and adjusted<br/>using a tone curve to equalise the exposure histogram<br/>in Photoshop CC2017.</b></p>                |
|    |   |
| <p><b>Medium sensitivity 50% cut-off<br/>input image</b></p>                        | <p><b>Output image from the same images combined using<br/>standard deviation and adjusted using automatic<br/>histogram equalisation in MATLAB 2017a.</b></p> |
|  |    |
| <p><b>Medium sensitivity 50% cut-off<br/>input image</b></p>                        | <p><b>The same processing is used but the images are first<br/>converted to grayscale.</b></p>   |
|  |  |
| <p><b>Low sensitivity &lt; 10% cut-off</b></p>                                      |  |

#### 4.4.10 Overview of Improved Optical Assembly Operation

The described components throughout this chapter are shown combined in Figure 79. The light is emitted from the white LED of the light source. Improvements to this light source allow for prolonged run times due to the large heat pipe computer processor heatsink. The light then passes through a diffuser that helps to give even illumination onto the light source lens where it is focused before passing through the beam splitter. Most of the focused light then passes onto the test area for the first pass of the product being tested. Light that encounters leaking helium is refracted at a slightly different angle to the rest of the light.

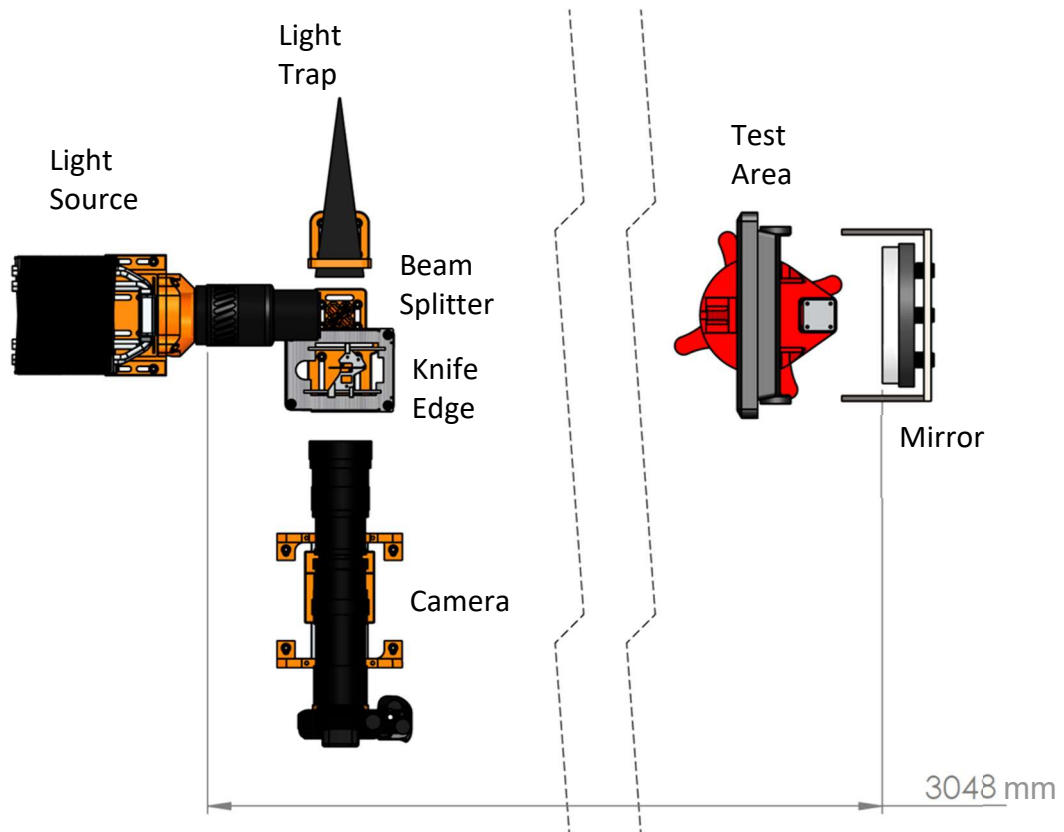


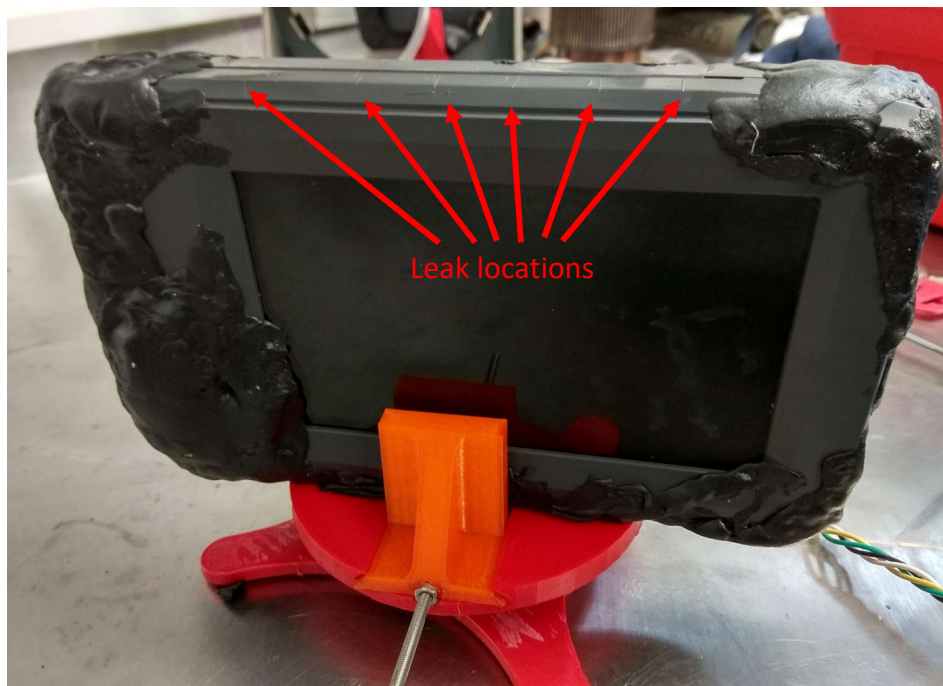
Figure 79 - Overview of Optical Components

Some of the light does not pass through the beam splitter from the light source and, instead, is captured by the light trap. When a light trap is not used, this light causes a significant amount of background illumination lowering the contrast of the images as seen in Figure 74. Light that passes through the test area without hitting the product being tested is then reflected by the mirror. The new stand that the mirror is housed in is much more stable than the one it came with and resists rocking, which would require realignment of the optical system. Light from the mirror is reflected towards the beam splitter and has another chance to encounter leaking helium.

The returning light is reflected by the beam splitter towards the knife edge cut-off. Improvements to the cut-off in Section 4.4.2 significantly increase the ease of cut-off adjustment. This allows images with much more detail in the leaks to be captured.

## 5 Testing of Schlieren optics to locate leaks on a Navico product

One of the enclosures received from Navico was used to construct a test leak. 6 small holes were made in the gasket that seals the enclosure with a knife at even increments along the top edge, these are shallow cuts into the gasket with the blade that are too small to see, therefore marks were made in the plastic case beside them as locating features (Figure 80). Vacuum testing was performed at Navico for each of the holes, at both the production and R&D vacuum levels, and the decay of vacuum over time was logged via a vacuum gauge.



**Figure 80 - Test product held in rotating base**

Navico's 2 tests are designed to replicate the forces that submersion into water would cause. Production testing is performed for a shorter duration using a lower vacuum, the R&D test is harder for a product to pass due to a higher vacuum combined with a longer testing period.

A MATLAB program was written to load all the data files from the vacuum testing gauge and plot them in order to compare the deterioration of vacuum over time to Navico's leak testing criteria. Leaks that failed the production criteria were visible both using a knife edge and colour filters for the cut-off. Leak 3 passed the production criteria, but it

failed the R&D criteria by a slim margin. This was visible only by using a knife edge cut-off (Figure 81).



Figure 81- Leak 3

Figure 82 shows the deterioration over time for each of the 6 leaks in the enclosure under R&D testing vacuum pressure. Each leak was tested three times to make sure the results from each leak was consistent. Leak 4 (yellow) and 5 (red) failed the production leak testing criteria (dashed line), while the other 4 leaks passed the production criteria.

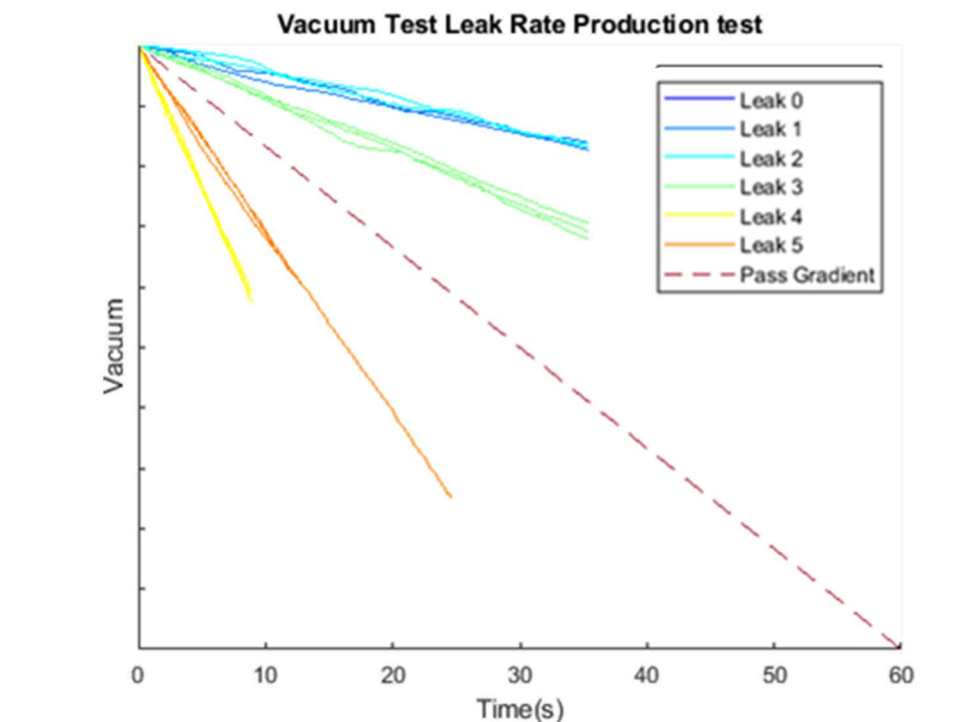
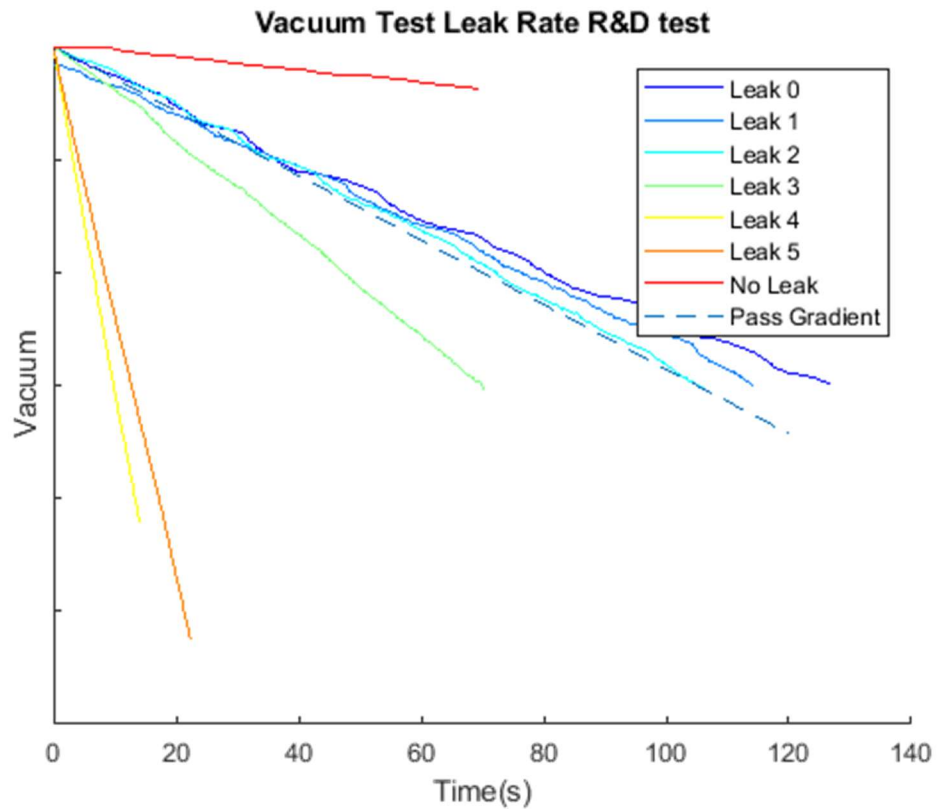


Figure 82 - Vacuum testing production criteria

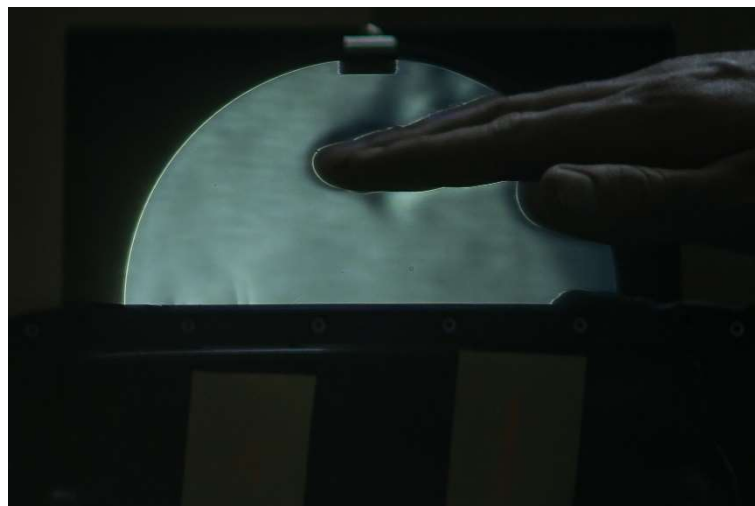
Figure 83 shows vacuum testing at the R&D testing vacuum. In this test, leak 3 failed alongside leak 4 and 5. Leak 2 was very close to the fail criteria. Because of the extended time taken for the R&D test, each leak was only tested once. Another thing to note for

the R&D vacuum test is that there is a noticeable drop in the vacuum with all the holes covered. This is not as apparent in the production test.



**Figure 83 - Vacuum testing at R&D criteria**

In Figure 84, all the leaks were left uncovered to show the differences in leak size between the leak. A hand was also used to give a comparison of the disturbance to the refractive index in the air due to body temperature as compared to the small amount of helium able to escape from the leaks.



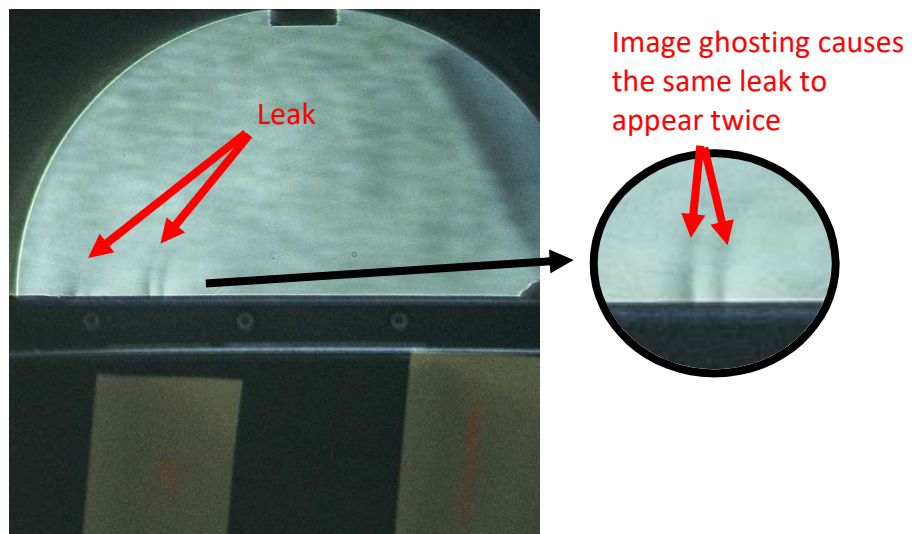


**Figure 84 - All leaks uncovered, beam splitter is not used and knife edge is at 45 degrees**

## 5.1 Improved Schlieren Optical Assembly

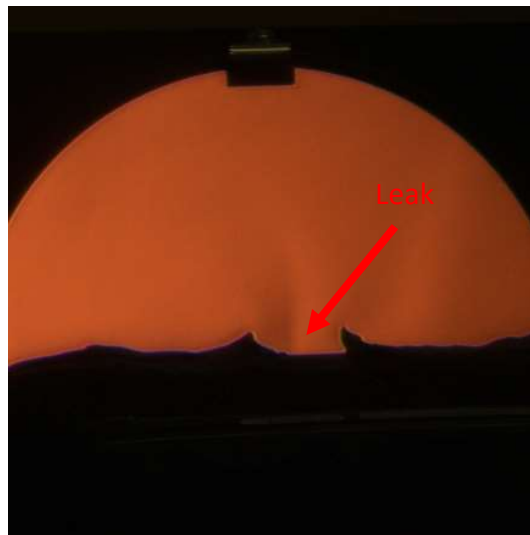
The images returned by the Schlieren optical setup have gone through changes at each stage of development of the Schlieren optical assembly described in Section 4. Using AUT's original Schlieren optical assembly, no leaks were visible when the sample enclosure was tested.

Initial improvements to AUT's existing optical assembly changed the layout from two mirror Z-type to single mirror Double Pass with a sharp knife edge and white light source (Section 4.3). These initial improvements allowed for the first images of the leaks to be returned. While changing to a double pass layout increased sensitivity to the stage that the leaks were visible, it had the effect of causing image ghosting. This can be seen in Figure 85, where there should only be 2 visible leaks, but the optical assembly returned 4.



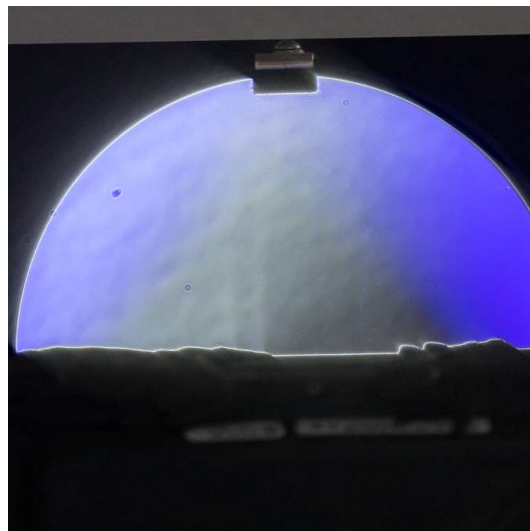
**Figure 85 - Double Pass with Soligor 135 mm (note each leak is seen twice due to the lack of a beam splitter)**

The addition of a white light source allowed the use of colour Schlieren imaging. This was effective for large disturbances, such as the flame seen in Figure 48, but proved to be ineffective when used with smaller disturbances. This was because there was not enough difference in the refraction of the light to give clearly different colours in the returned images, as is shown in Figure 86.



**Figure 86 - Colour Schlieren with small disturbances**

The next area of the optical assembly that was changed was the lens. 70-200 mm zoom lenses from Cannon and Sony were tested. Unfortunately, the lens coating on these caused uneven colour casts across the image; the better of the two lenses was the Sony 70-200 mm but this still had a blue colour cast shown in Figure 87.



**Figure 87- Double Pass with Sony 70-200 mm lens and beam Splitter**

With what was learned from the previous stages of the optical assembly development, a new optical assembly was designed based around using one of AUT's 6-inch mirrors. The changes made to the design were extensive and are outlined throughout Chapter 4. The main changes included a new 420-800 mm lens, beam splitter, light trap, mirror stand and an aluminium base that all the optical components, excluding the mirror, were mounted to.



### 5.1.1 Sensitivity to Leak 3

The test leak 3 in the Navico test product passed production testing standards set out by Navico but it failed R&D testing at the higher vacuum and longer test time. This leak shows that Schlieren optics can detect leaks that are very hard to locate by Navico's current water submersion testing, whereas leak 4 and leak 5 could be detected by water submersion testing as shown by Figure 88.



Figure 88 - Leak 3 (Left) Leak 4 & 5 (Right)

Leak 3 could be located with the improved Schlieren optical assembly when leak 4 and leak 5 were sealed, otherwise leak 4 & 5 overwhelm the test. In Figure 89, leak 3 can be seen when all other leaks are covered. It also shows that, when all leaks are uncovered, leak 3 is no longer detectable.



Figure 89 - Leak 3 detected (left) Leak 3 is no longer detectable with Leak 4 & 5 uncovered (right)

## 6 Image Processing

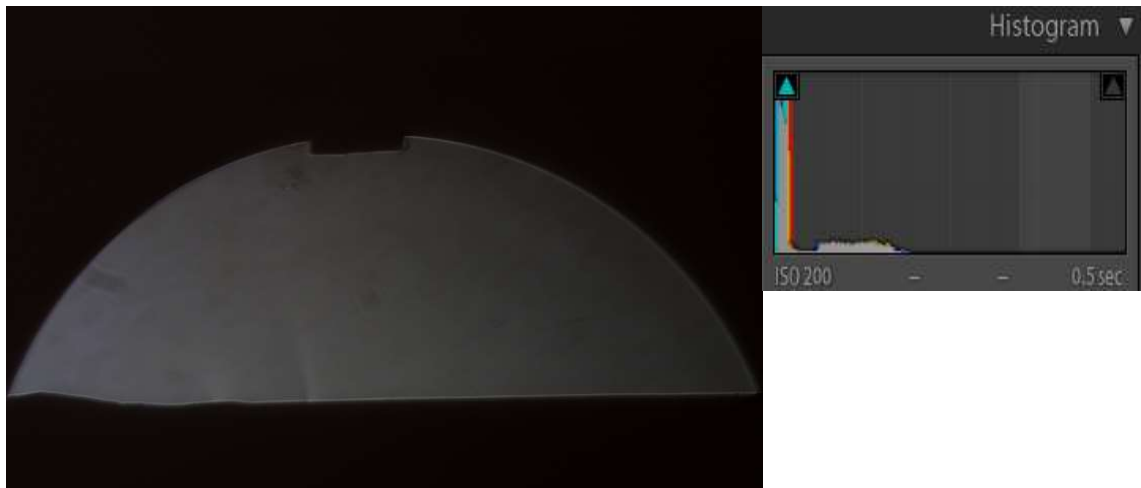
One area of Schlieren optics that is not commonly covered in the literature is what to do with the output from a Schlieren optical experiment. Settles makes some mention of digital image processing in his book but, at the time of writing, digital cameras were still very much a new technology without the photo editing software available now. When Settles' book was published, he was adding contrast by compressing the histogram of 0.5 megapixel 8 bit images with 256 levels of colour down to around 20 levels (Settles, 2001).

With a modern camera, such as the Sony a7 used in these experiments, the images produced are 24.3 megapixel 14 bit Sony Alpha Raw (ARW) 2.3 raw image format (SONY New Zealand, 2017). The amount of colour levels that can be stored in modern 14-bit image formats has increased from the 256 levels possible for 8 bit to 16384. This huge jump in raw colour data means that far more detail can be extracted from a single image.

### 6.1 Adobe Lightroom Creative Cloud

There are a range of different software packages available for image processing. One of the easiest to use is Adobe Lightroom. During this project, Lightroom Creative Cloud and Photoshop are used as an initial way of adding contrast and clarity to leaks so that they could be better seen.

There are two ways to do this in Adobe Lightroom: the contrast slider can be used for overall contrast adjustment; or clarity can be used to only add contrast to areas where Adobe Lightroom detects the edges of features.



**Figure 90 - low sensitivity image of a leak before Lightroom adjustment**

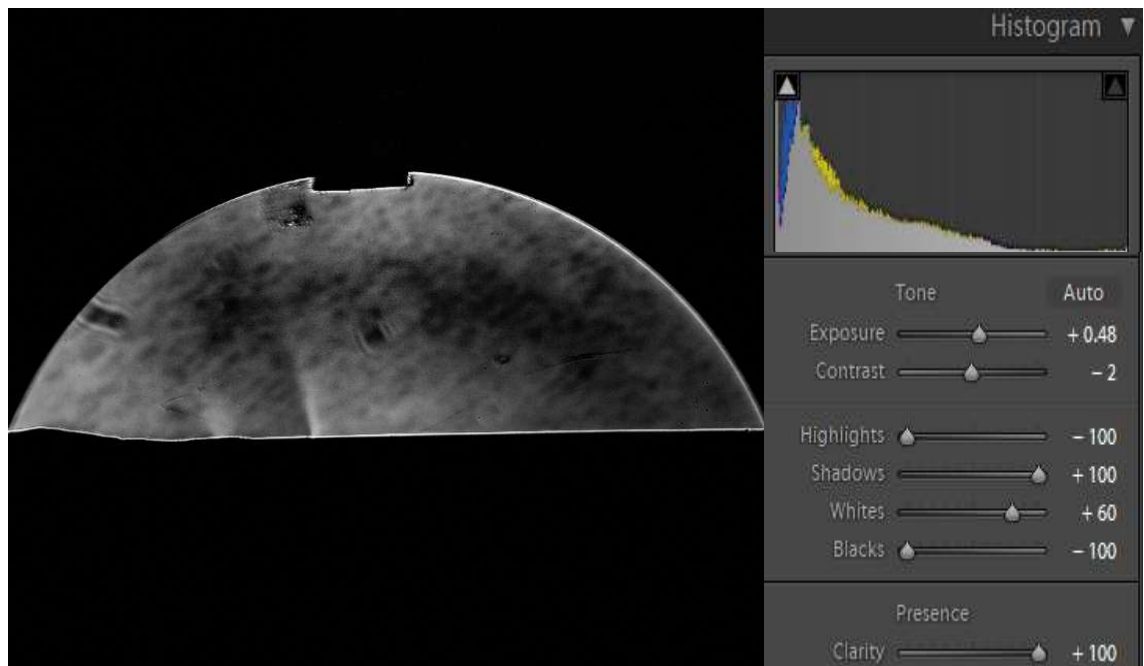
Figure 90 shows the image before any adjustment in Lightroom. Since the image was taken with a low amount of cut-off, the details of the leaks are very faint.

The first adjustment is to increase the overall exposure of the image, and then selective adjustment of the highlights, shadows, whites, and blacks is added to expand the histogram towards the right. Instead of using the contrast adjustment slider to add contrast to the entire image, clarity is used to add local contrast to features in the image such as leaks and edges of the mirror.

Figure 92 shows the effect of basic exposure and contrast adjustments on the image. Using clarity (local contrast) adjustment adds significant definition to the edges around the leaks, making them easy to see. The effect of this is that even Schlieren images with low sensitivity can be digitally enhanced to show more detail than images taken with high sensitivity (Figure 91).

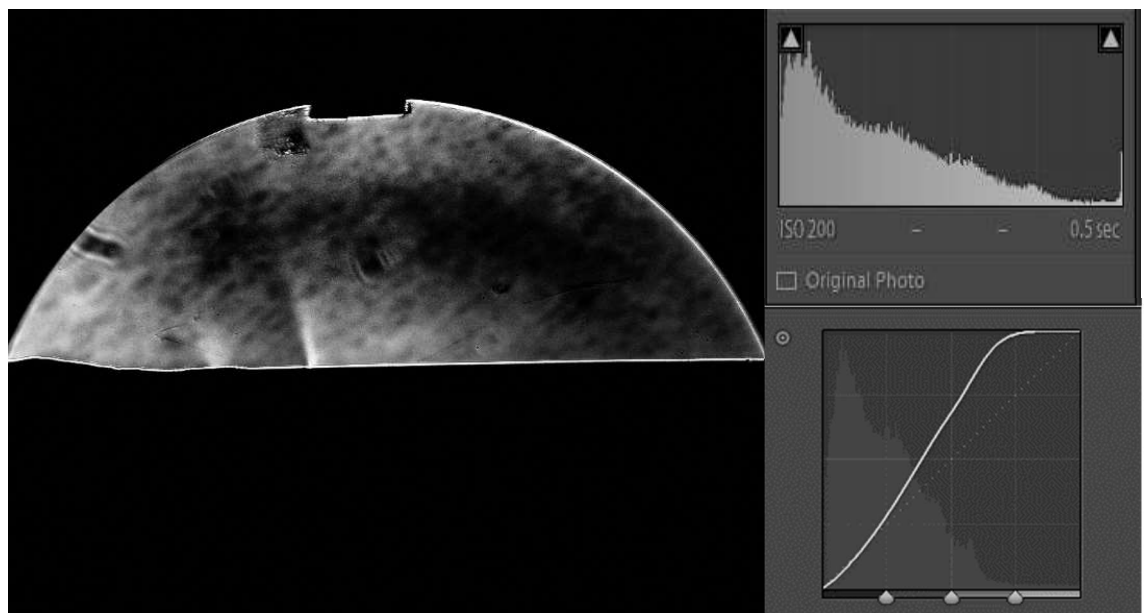


**Figure 91 - Near full cut off**



**Figure 92 - low sensitivity image of a leak after basic Lightroom adjustment**

Another way of adding contrast to images in Lightroom is by use of a tone curve. This allows for fine exposure adjustment at points along the histogram. In Figure 93, this technique is used to add further contrast to the image in Figure 92.



**Figure 93 - low sensitivity image of a leak after basic and tone curve Lightroom adjustment**

## 6.2 MATLAB

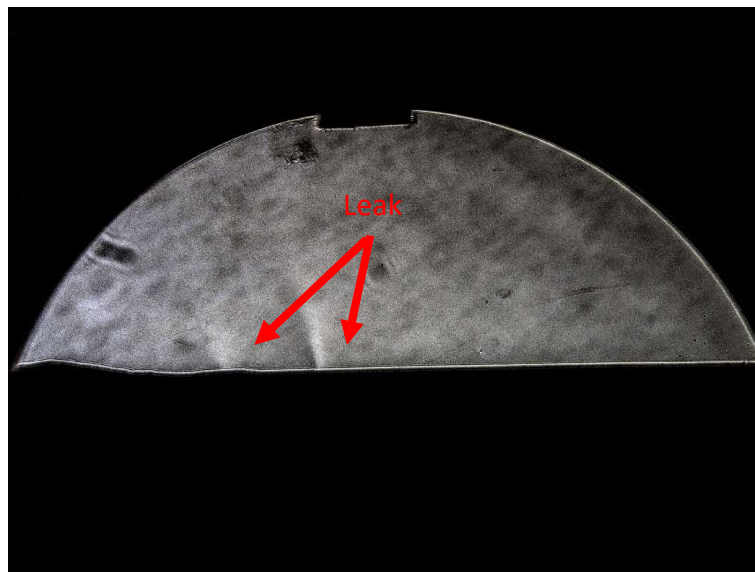
The Adobe software suite is designed for creative processing of images into artworks. Because of this, Lightroom has processes in the background beyond the user's control that constantly adjust to try make images more visually appealing. An example of this is automatic lens correction and noise reduction. While this can be reduced by disabling the detail, camera calibration and lens correction features still run in the background. A disadvantage of this background processing is that it can easily mistake fine details for image aberrations and therefore it removes them from the image.

The image processing toolbox in MATLAB is designed for more scientific use than the Adobe software suite. It does not have the background processing, and therefore allows much more control over the processing of images and allows fine details to be kept.

## 6.3 Local contrast


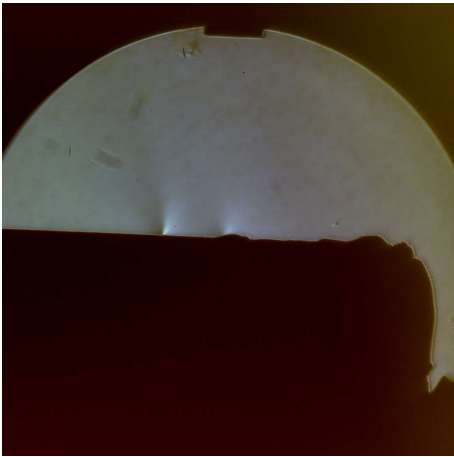
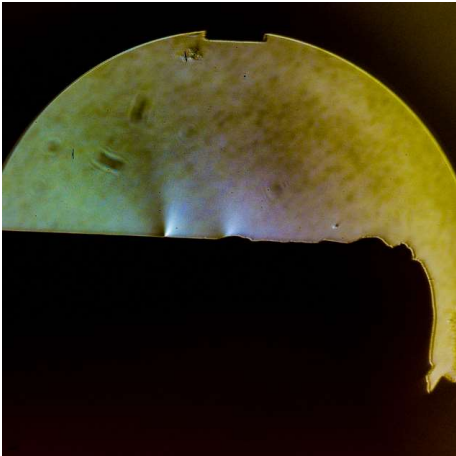
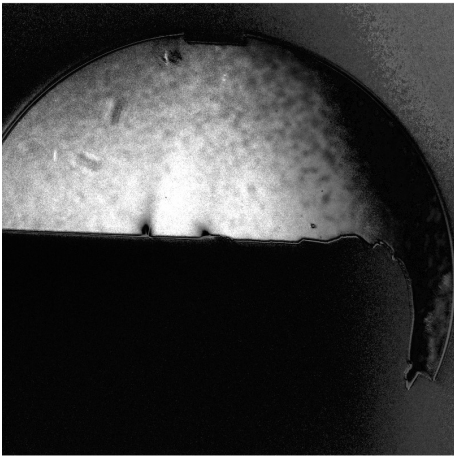
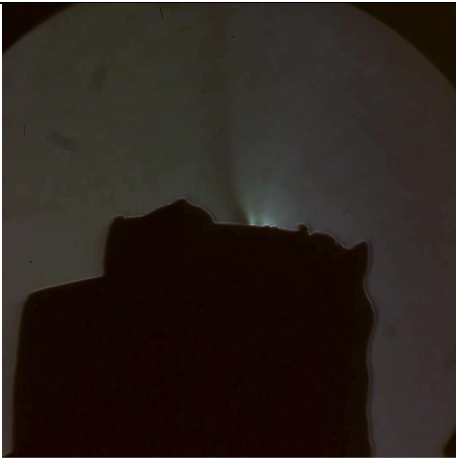
Figure 94 shows MATLAB local contrast adjustment. This image shows a lot finer detail of the leaks when compared Figure 93 at the cost of much higher image noise. The higher image noise of the MATLAB contrast adjustment is also apparent in Table 3.

To process the image in MATLAB, the raw image was saved in a 16-bit tiff format and then imported and processed using the code in appendix A.



**Figure 94 - MATLAB Contrast adjustment using `localcontrast()` with an edge threshold of 0.4 and an amount of 1**

**Table 3 - Images of leak 4 and 5 showing different processing techniques**

|  |  |
|--|--|
|  <p><b>Raw Single image from the Improved Schlieren Optical Assembly</b></p>  |  <p><b>Raw image with colour balanced and exposure increase (these adjustments are in camera settings)</b></p> |
|  <p><b>Colour balanced image with contrast adjustment in Adobe Lightroom</b></p>   |  <p><b>High sensitivity range Imaging from 4 images using MATLAB</b></p>                                      |
|  <p><b>Side view showing leak location using the Improved Schlieren Optical Assembly image with colour balanced and exposure increase</b></p> |  |

## 7 Computer Vision

The use of image processing allows details in the Schlieren images to be seen with more ease. Even so, an inexperienced user who is unfamiliar with what to look for may have a lot of difficulty in finding a leak. A more experienced user may also have trouble finding a leak when it is very small. The next logical step after image processing is using computer vision to predict areas where leaks occur.

Two groups of training images were made for the training of Region-Based Convolutional Networks during the project. The first consisted of 198 images of leaks that were taken during testing of the both colour and double pass Schlieren optics.

The second batch of training images consists of 840 images that were labelled later in the project when a higher number of images were available. These images were from continued testing of the Double Pass Schlieren optical assembly with the rotating product table and automated cut-off.

MATLAB offers three different Region-Based Convolutional Neural Network (RCNN) frameworks. The first is standard RCNN, which takes less time to train but offers poor detection speed and accuracy. The second framework is the Fast RCNN which offers greater accuracy, faster training speed and detection speed when compared to the older RCNN (Girshick, 2015). The third framework that MATLAB has implemented is the imaginatively named Faster RCNN, which offers greater accuracy and detection speed when compared to Fast RCNNObjectDetector. However, its training time is significantly longer due to a four-stage training process (Ren, He, Girshick, & Sun, 2015).

### 7.1.1 Region-Based Convolutional Networks

#### Training Region-Based Convolutional Networks

To use Region-Based Convolutional Networks for leak detection, the networks first must be trained on data that has already had regions of suspected leaks labelled. The MATLAB Image labeller can be used to label leaks for use with MATLAB. It can be simply opened by entering the command 'imageLabeler' into the MATLAB command window.

## 7.2 Semantic Segmentation Convolutional Networks

While region based networks can detect the region in which an object exists in an image, Semantic Segmentation takes this one step further by labelling objects on a single pixel level. This is advantageous because sometimes the regions RCNNs propose are quite large, and identifying a singular leak can be hard. An example of this is shown in Figure 95 where the region contains two very faint leaks instead of one.

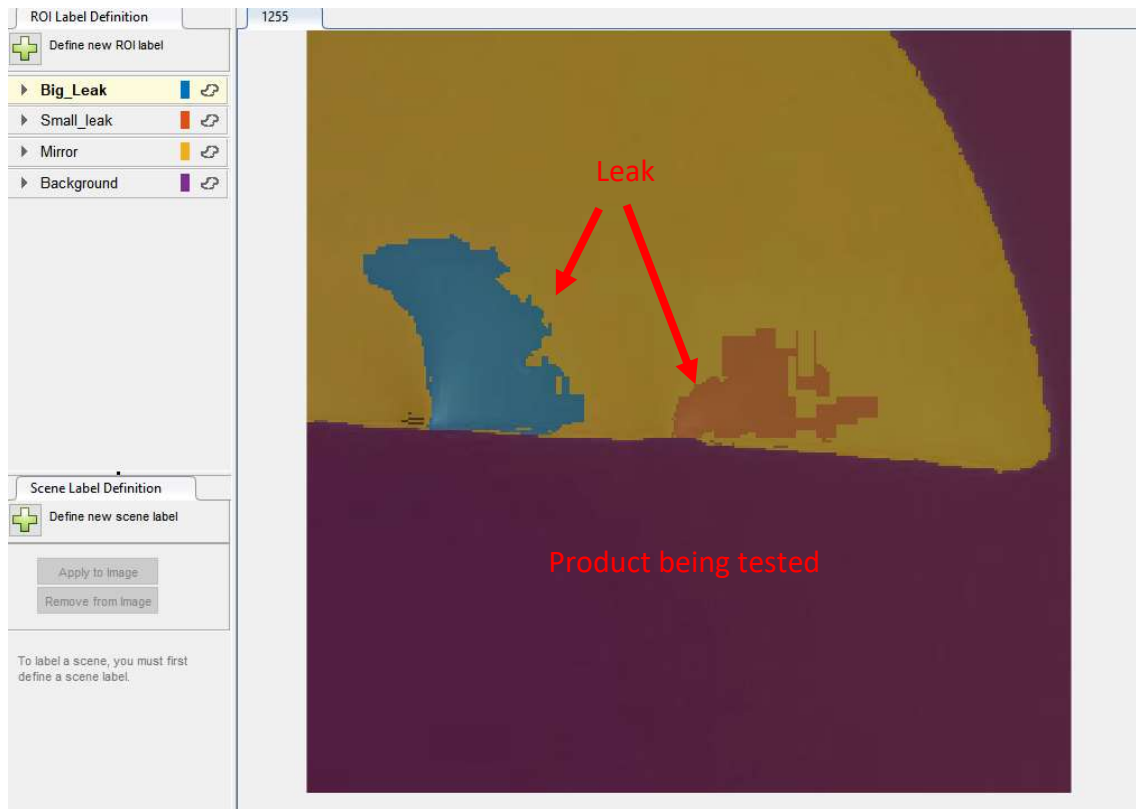


Figure 95 - Large Region Proposed by An RCNN that contains 2 leaks

### 7.2.1 Training Networks for Semantic Segmentation

Training convolutional neural networks for semantic segmentation takes a very similar approach to training networks for region detection. The same image labeller is used for labelling the training data. The same Stochastic Gradient Descent with Momentum algorithm is used and the same training options are available with the addition of the ability to use training progress plots as of MATLAB 2018a.





**Figure 96 - Pixel labelling training data for Semantic Segmentation**

Care must be taken when training larger images because video memory requirements are much higher than what is needed for training region based networks. Because of this, the training data was cropped and a smaller mini batch size was used.

Training of Semantic Segmentation networks was carried out on the MATLAB pre-release 2018a using an Nvidia GTX 1080ti GPU. Training data consisted of 262 images cropped to 300 by 300 pixels from the 840-image data set used for RCNN training. The best results were obtained using a mini batch size of 8, 0.9 momentum, learn rate of  $5 \times 10^{-3}$ , and training for 100 epochs. 300 by 300 pixels caused the GPU used (a GTX 1080ti with 11 Gigabytes (GB) of video memory) to run out of video memory with a mini batch of 8.

## 7.3 Performance of Computer Vision

### 7.3.1 Accuracy

The accuracy of neural networks is measured by comparing the intersection over union of the networks results to a labelled dataset. During training, the network is tested against the training data used in the mini batch to give mini batch accuracy at each iteration. At regular intervals, the accuracy of the network needs to be tested against other labelled data that is not used for training; this allows the number of epochs and learning rate to be adequately adjusted so that overfitting of the network to the training data does not occur.

#### Regional Convolutional Neural Networks

Precision is the ratio of true positives from the network divided by the total number of positives from the network. Recall is the number of true positives divided by the number of true positives and false negatives. To calculate precision and recall, first true positives must be defined. The default for this is an intersection over union result higher than 0.5; false negatives are when the network fails to detect a feature that was labelled in the test data.

For training of RCNN's MATLAB's 'trainFasterRCNNObjectDetector' function does not fully support the use of a separate training dataset for evaluation of the network accuracy during training. To get around this, the network training can be paused and the 'evaluateDetectionPrecision' function can be used instead. This function gives accuracy in terms of precision and recall instead of intersection over union.

Ideally, both high recall and high precision should be set such that the network detects with a low number of both false positives and false negatives. To measure this, a value known as Average Precision (AP) is used. This is essentially the average of precision multiplied by the change in recall.

Figure 97 and Figure 98 show training of the VGG19 network using the full size 840 image training dataset. Figure 97 shows the effect of different learn rates on the average precision of the VGG19 network; the fastest learn rate of  $5 \times 10^{-4}$  causes the average precision to drop off after 10 epochs due to over training, and using a learn rate of

$5 \times 10^{-5}$  causes the VGG19 network to keep improving average precision up until around 70 epochs, as can be seen in Figure 98 . However, training the VGG19 network on the 840 image data set took four days for 100 Epochs using an overclocked Nvidia 1080ti graphics processor.

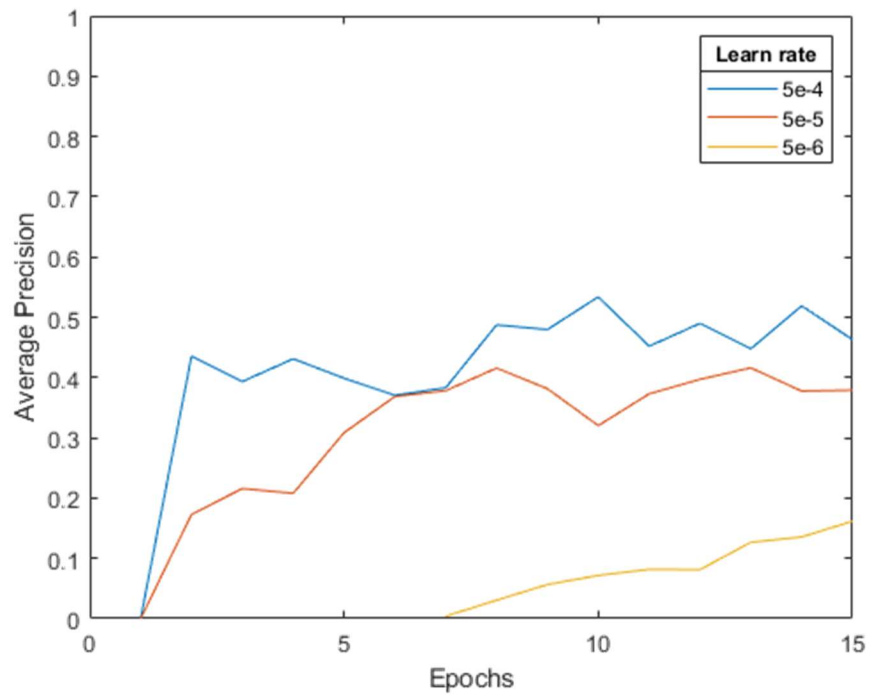


Figure 97 – Average Precision for VGG19 over 15 epochs with different learn rates

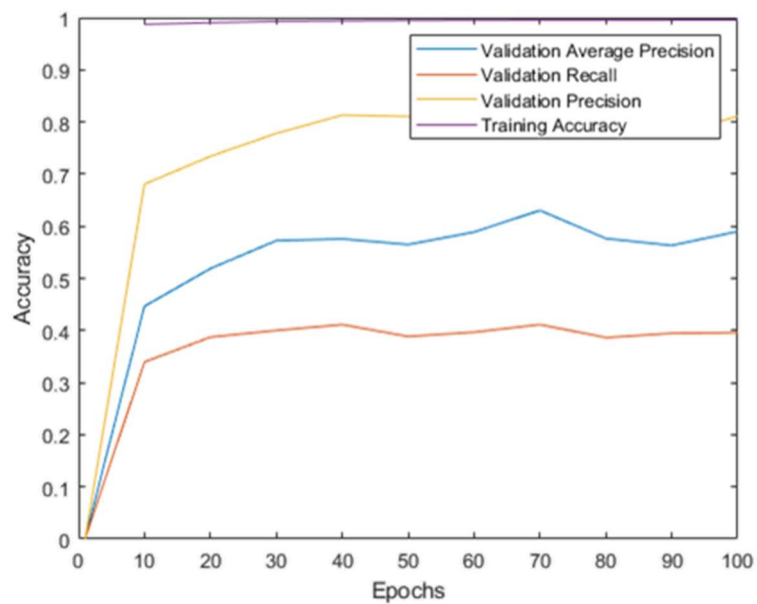


Figure 98 - Test and Training Accuracy for VGG19 over 100 epochs

Table 4 shows the best results in accuracy for the Alexnet, VGG16 and VGG19 networks. The networks were trained over 100 epochs with a learn rate of  $5 \times 10^{-5}$ ; four different training data sets were used, but the same 100 image validation data set was used in each test.

The results in Table 4 are taken from the network that had the highest average precision performance at 10 epoch validation test increments; during training, the network was saved at this point.

The four different training datasets were used due to limitations in software and GPU memory. At the beginning of testing networks, the only available graphics card was an Nvidia GTX 950m from a laptop with 4 GB of memory. This limited the size of the images that could be used in the training dataset without crashing MATLAB. Later in the project, an Nvidia GTX 1080ti was purchased with 11 GB of memory. With MATLAB 2017b, a cropped-down version of the dataset had to be used when training VGG16 and VGG19. Optimisations added in the MATLAB 2018a release allowed for the full size 840 image dataset to be used.

**Table 4 - Comparison of network accuracy**

| Network type | Epoch of training | Training images | Learn rate         | Cropped | Average Precision | Recall | Precision |
|--------------|-------------------|-----------------|--------------------|---------|-------------------|--------|-----------|
| Alexnet      | 100               | 198             | $5 \times 10^{-4}$ | Yes     | 0.0107            | 0.1038 | 0.0520    |
| Alexnet      | 100               | 198             | $5 \times 10^{-4}$ | No      | 0.2819            | 0.4127 | 0.2611    |
| Alexnet      | 100               | 840             | $5 \times 10^{-4}$ | Yes     | 0.2921            | 0.3673 | 0.4180    |
| Alexnet      | 100               | 840             | $5 \times 10^{-4}$ | No      | 0.5909            | 0.3976 | 0.8050    |
| VGG16        | 100               | 198             | $5 \times 10^{-4}$ | Yes     | 0.0304            | 0.0698 | 0.0159    |
| VGG16        | 100               | 198             | $5 \times 10^{-4}$ | No      | 0.3504            | 0.5764 | 0.4087    |
| VGG16        | 100               | 840             | $5 \times 10^{-4}$ | Yes     | 0.4251            | 0.4905 | 0.6493    |
| VGG16        | 100               | 840             | $5 \times 10^{-4}$ | No      | 0.6551            | 0.6319 | 0.6656    |
| VGG19        | 100               | 198             | $5 \times 10^{-4}$ | Yes     | 0.02731           | 0.0742 | 0.1940    |
| VGG19        | 100               | 198             | $5 \times 10^{-4}$ | No      | 0.4853            | 0.6513 | 0.4119    |
| VGG19        | 100               | 840             | $5 \times 10^{-4}$ | Yes     | 0.3486            | 0.4721 | 0.3207    |
| VGG19        | 100               | 840             | $5 \times 10^{-4}$ | No      | 0.6304            | 0.4114 | 0.8429    |

### Semantic Segmentation

Accuracy of Semantic Segmentation networks was difficult to measure. The network that performed the best at detecting both big and small leaks gave an intercept over overlap result of 0 for both big and small leaks as shown in Figure 99. With bigger training and validation datasets, this could possibly be improved, but the time it would take to collect and label all the data would be excessive for this project.

| Var1         | iou     |
|--------------|---------|
| 'Mirror'     | 0.57039 |
| 'Background' | 0.77537 |
| 'Big_leak'   | 0       |
| 'Small_leak' | 0       |

**Figure 99 - Results from the best performing network**

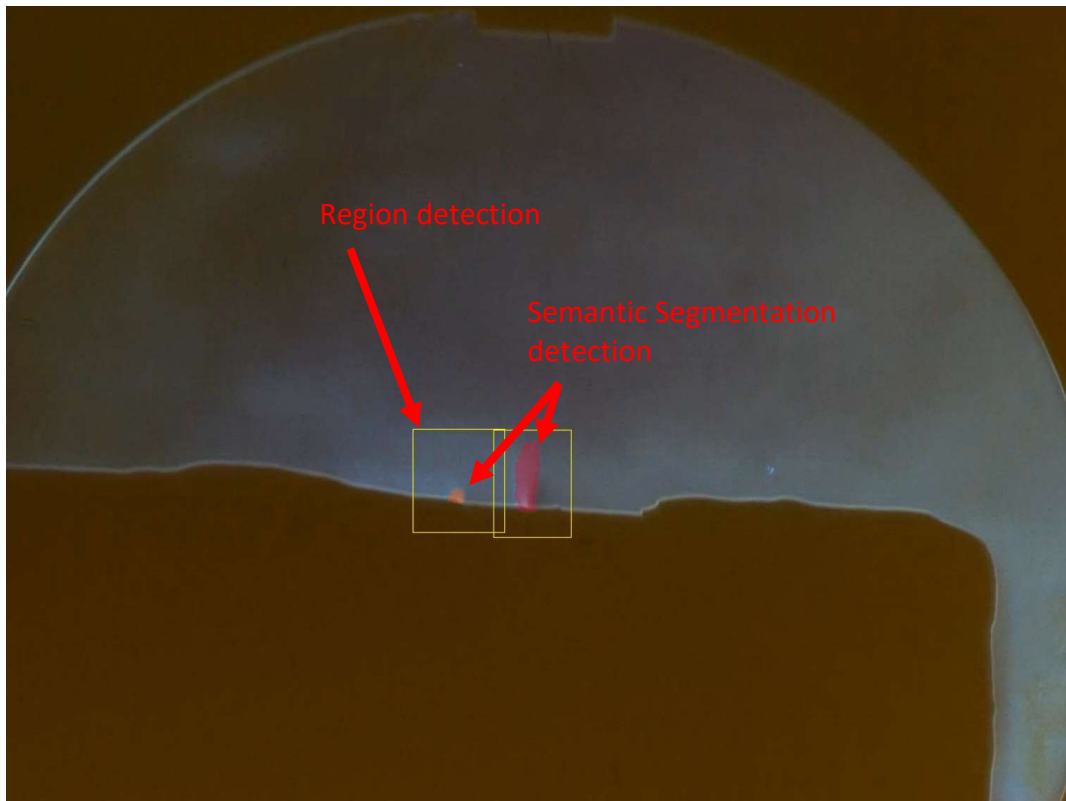
### 7.3.2 Speed

To establish if it is possible to use region based neural networks to detect leaks in real time, the speed at which a single network can detect leaks in video footage was measured on two graphics processing units at a range of video resolutions. Detection fps is the average frames processed per second over a 1491 frame video of leaks filmed on the Improved Schlieren Optical assembly using networks trained using faster R-CNN, a summary of the processing speed at each of these configurations can be seen in Table 5.

**Table 5 - Speed of detection in frames per second for Regional networks**

| Detection of leaks from input 25fps video |         |            |                        |                       |  |      |       |
|---|---------|------------|------------------------|-----------------------|--|------|-------|
| Graphics card                             | Network | Cuda cores | Core clock (Megahertz) | Video ram (Megabytes) | GPU Performance (in frames per second) |      |       |
|   |         |            |                        |                       | 1080p                                  | 720p | 320p  |
| GTX 1080ti                                | VGG19   | 3584       | 2088                   | 11264                 | 1.88                                   | 3.24 | 6.56  |
| GTX 1080ti                                | VGG16   | 3584       | 2088                   | 11264                 | 2.01                                   | 3.40 | 5.35  |
| GTX 1080ti                                | Alexnet | 3584       | 2088                   | 11264                 | 4.45                                   | 6.81 | 12.95 |
| GTX 950m                                  | VGG16   | 640        | 1124                   | 4096                  | 0.32                                   | 0.63 | 1.23  |
| GTX 950m                                  | Alexnet | 640        | 1124                   | 4096                  | 1.69                                   | 2.15 | 4.68  |

The detection speed for Semantic Segmentation networks was significantly slower than Regional networks, achieving 0.701 frames per second compared to 1.88 frames per second that Regional networks achieved at full HD when trained from the VGG19 pre-trained network. Combining both Regional and Semantic Segmentation networks together (Figure 100) showed promise with the Semantic Segmentation networks only searching areas within a 500 pixel rectangle of the Regional network detections, this achieved a frame rate of 1.6 fps.



**Figure 100 - Hybrid Regional + Semantic Segmentation**

## 8 Conclusion

At the commencement of this project, the goal was to find a visual method of detecting leaks in the enclosures of marine electronic devices that Navico produces. During review of literature, both Schlieren optics and interferometry presented themselves as being viable options for this by using an inert tracer gas with a different refractive index to the surrounding air.

Schlieren optics was chosen for testing because of its overall lower complexity, leading to a cost advantage, as well as its greater leniency to the need for accurate calibration and resistance to outside disturbances when compared to interferometry.

Testing of both Colour and Monochromatic Schlieren optics showed that while Colour Schlieren could show detail in large disturbances, such as the flame in Figure 48, it was unable to show as much fine detail when used to detect the locations of intentionally made leaks in a test product provided by Navico. By comparison, Monochromatic Schlieren Optics showed the ability to locate leaks that would meet Navico's production testing requirements and almost meet the requirements of R&D testing.

With Monochromatic Schlieren Optics showing the greatest potential, the optical assembly was further developed with a range of improvements to increase sensitivity and ease of use. The biggest of these improvements was mounting all the optical components except the mirror to a single aluminium base.

Significant improvements to the ease of use of Schlieren optics came from mounting the knife edge on a motorised linear slide repurposed from a DVD drive, and the use of Arduino. A stepper motor driver controlled by a MATLAB user interface allows for much finer adjustment of the cut-off without needing to touch the optical assembly and risking inducing vibration.

The stepper motor add-on board used allowed the use of a second stepper motor as well as the ability to control hobbyist Servos. The control of a second stepper motor was used to automate a rotary platform that moves the product being tested into different orientations. The servo control was used to fire the camera shutter by using an infrared trigger; this allowed completely hands-off operation of the optical assembly with many



images being automatically collected at different cut-off settings and product orientations within a range specified by the user.

The automation of the knife edge and camera allowed for a novel solution to one of the biggest disadvantages of Schlieren optics: for a specific knife edge setting or orientation only, some of the refractive disturbances in the test area will be visible. It was found that increasing cut-off reveals smaller disturbances while obscuring bigger ones, and changing cut-off angle can completely hide the part of a disturbance that causes refraction at that angle. Combining images from multiple cut-off settings solved this problem.

With two knife edges mounted perpendicular to each other on the motorised linear slide, images with various cut-off levels could be captured on each knife edge and then be combined into a single image that shows the complete range of disturbances. Combining the images was carried out in two ways: one method used Adobe Photoshop and the other used MATLAB to stack the images using standard deviation weighting in section 4.4.9.

With the image data from captured by the prototype optical assembly a small training dataset was labelled for training RCNN's, 840 images were used. Networks based on Alexnet, VGG16 and VGG19 were trained. The ability to train the VGG16 and VGG19 networks on full size 2000 pixel wide images was gained after purchasing a much more capable Nvidia GTX1080ti graphics card, and this led to significant increases in detection accuracy.

Semantic Segmentation networks were also experimented with. Due to the time-intensive nature of labelling every single image pixel, over a week was spent labelling a 200 image training dataset. Semantic networks offer a good alternative to RCNN's because they label individual pixels of leaks instead of just the region in which the leak occurs.

## 9 Future work

### 9.1 Upscaling the optical assembly for use with bigger products

There are two apparent ways to upscale the assembly for use with bigger products: the first approach is to use a bigger mirror that can encircle the entire outline of the product being tested. The second approach would be to use a smaller (and therefore cheaper) mirror to view part of the product and then move the product to scan the entire product for leaks. This process could be automated in a similar way to the rotating platform.

Stocked mirror sizes from Edmund Optics range up to 10 inches in diameter. These cost \$2025 USD Excluding Shipping (Edmund Optics, 2018). The lens used throughout this project is suitable for any mirror with an aperture less than  $f/16$  set to its maximum 800 mm focal length.

Larger mirrors that have longer focal lengths will be advantageous because they give higher sensitivity to leaks for a given cut-off. This was discussed in Section 2.1.2

### 9.2 Feasibility and cost

The primary cost of building the Improved Schlieren Optical setup is:

- Spherical mirror: \$575 USD for 6" diameter to \$2025 USD for 10" diameter.
- Camera: \$798 USD for the camera used, but this could be significantly less without much reduction in image quality by using a camera with a smaller sensor.
- Aluminium extrusion and other hardware for the base \$218 NZD including shipping
- Lens: \$104 USD
- 100 W LED NZD 8.50

The rest of the parts were recycled from old computers or 3D printed using inexpensive ABS filament.

## 10 Appendices

### Appendix A

#### MATLAB code to perform local contrast adjustment of an image

```
I = imread('DSC00013.tif'); % Import image

I=localcontrast(I,0.4,1); % Perform local contrast adjustment with edge threshold=0.4
and amount=1

imshow(I); % Show the image
```

#### MATLAB code to perform 3d ray tracing

```
clc
clear

ray_number=100;% number of rays
r2=0.01;% round cut-off radius
cutyshift=0.01; % cut-off shift (use a large radius and shift to one side to simulate knife edge)
cutxshift=0;

focal_length=6*20*25.4; % mirror focal length
mirror_radius=3*25.4;% mirror radius
n1=1; n2=1.0001; % refractive indexes of air(n1) and schliere(n2)
nx=nan(ray_number); ny=nan(ray_number); nz=nan(ray_number);
x=zeros(ray_number,ray_number,9);%light source x origin
y=zeros(ray_number,ray_number,9);%light source y origin
z=zeros(ray_number,ray_number,9);%light source z origin

Q1=zeros(ray_number,ray_number,3);Q2=zeros(ray_number,ray_number,3);

%calculate points for light coming from source
[z(:, :, 2), y(:, :, 2)]=meshgrid(linspace(-mirror_radius,mirror_radius,ray_number),linspace(-mirror_radius,mirror_radius,ray_number));
x(:, :, 2)=sqrt(-(y(:, :, 2).^2+z(:, :, 2).^2-focal_length.^2));

%cut out round outline
ang=0:0.1:2*pi;
xv=mirror_radius*cos(ang);
yv=mirror_radius*sin(ang);
in = inpolygon(z,y,xv,yv);
x(~in)= nan;
y(~in)= nan;
z(~in)= nan;

%calculate schliere surface points
[F, V, N]=getstl();
```

```

% plot mirror
surf((x(:,2)),(y(:,2)),(z(:,2)));

%find schliere angle of incidence and refraction angle

%% ray first hits object
dir=1;
n=(n1/n2);
Q1(:,1)=x(:,1); Q1(:,2)=y(:,1); Q1(:,3)=z(:,1);
Q2(:,1)=x(:,2); Q2(:,2)=y(:,2); Q2(:,3)=z(:,2);
%set points to find intercept
[x(:,3),y(:,3),z(:,3),nx,ny,nz]= surfaceintercept(F,N,Q1,Q2,V,ray_number,dir);%find
intercept
ix=(x(:,3)-x(:,1)); iy=(y(:,3)-y(:,1)); iz=(z(:,3)-z(:,1));% find vector of intercept
l=sqrt(ix.^2+iy.^2+iz.^2);
ix=ix./l; iy=iy./l; iz=iz./l; % find unit vector

%use Snell's law to find refraction

[tx(:,1),ty(:,1),tz(:,1)]=refraction(ix,iy,iz,nx,ny,nz,ray_number,n,x);

%% ray then exits object
dir=0;
n=(n2/n1);
Q1(:,1)=x(:,3); Q1(:,2)=y(:,3); Q1(:,3)=z(:,3);
Q2(:,1)=x(:,3)+tx(:,1); Q2(:,2)=y(:,3)+ty(:,1); Q2(:,3)=z(:,3)+tz(:,1);
%set points to find intercept
[x(:,4),y(:,4),z(:,4),nx,ny,nz]= surfaceintercept(F,N,Q1,Q2,V,ray_number,dir);%find
intercept
ix=(x(:,4)-x(:,3)); iy=(y(:,4)-y(:,3)); iz=(z(:,4)-z(:,3));
l=sqrt(ix.^2+iy.^2+iz.^2);
ix=ix./l; iy=iy./l; iz=iz./l; % find unit vector
nx=-nx;
%use Snell's law to find refraction
[tx(:,2),ty(:,2),tz(:,2)]=refraction(ix,iy,iz,nx,ny,nz,ray_number,n,x);

%% find where exiting light hits mirror
for i=1:ray_number
P0=[x(:,i),y(:,i),z(:,i)]'; P1=[x(:,4),y(:,4),z(:,4)]';
P2=[(x(:,4)+tx(:,2)),(y(:,4)+ty(:,2)),(z(:,4)+tz(:,2))]' ;
B = P2-P1;
C = P0-P1;
U = B./repmat(sqrt(dot(B,B)),[3 1]);
D = dot(U,C);
E = sqrt( D.^2 - dot(C,C) + focal_length.^2 );
F1 = [D+E; D-E];
[dummy, idx] = min(abs(F1));
G = F1(idx(1),:);
intersect = U.*repmat(G, [3 1]) + P1;
x(:,5)=intersect(1,:); y(:,5)=intersect(2,:); z(:,5)=intersect(3,:);
end
% %cut out round outline

in = inpolygon(z,y,xv,yv);
x(~in)= nan;
y(~in)= nan;
z(~in)= nan;
% % find vector of intercept

```

```

ix=(x(:,5)-x(:,4)); iy=(y(:,5)-y(:,4)); iz=(z(:,5)-z(:,4));
l=sqrt(ix.^2+iy.^2+iz.^2);
ix=ix./l; iy=iy./l; iz=iz./l;
nx=-ones(ray_number); ny=-y(:,5)/sqrt(focal_length.^2 - z(:,5).^2 - y(:,5).^2); nz=-
z(:,5)/sqrt(focal_length.^2 - y(:,5).^2 - z(:,5).^2);
l=sqrt(nx.^2+ny.^2+nz.^2);
nx=nx./l; ny=ny./l; nz=nz./l;

for i=1:ray_number
    for j=1:ray_number
        if ~isnan(x(i,j,1))
            Inc=[ix(i,j),iy(i,j),iz(i,j)];
            Nor=[nx(i,j),ny(i,j),nz(i,j)];
            te=(Inc+2.*dot(-Inc,Nor)*Nor);%reflection
            tx(i,j,3)=te(1);ty(i,j,3)=te(2);tz(i,j,3)=te(3);
        end
    end
end
%% reflected light

% %ray hits object
dir=0;
n=n1/n2;
Q1(:,1)=x(:,5); Q1(:,2)=y(:,5); Q1(:,3)=z(:,5);
Q2(:,1)=x(:,5)+tx(:,3); Q2(:,2)=y(:,5)+ty(:,3); Q2(:,3)=z(:,5)+tz(:,3);
%set points to find intercept
[x(:,6),y(:,6),z(:,6),nx,ny,nz]= surfaceintercept(F,N,Q1,Q2,V,ray_number,dir);%find
intercept
ix=(x(:,6)-x(:,5)); iy=(y(:,6)-y(:,5)); iz=(z(:,6)-z(:,5));% find vector of intercept
l=sqrt(ix.^2+iy.^2+iz.^2);
ix=ix./l; iy=iy./l; iz=iz./l; % find unit vector

% use Snell's law to find refraction 3
[tx(:,4),ty(:,4),tz(:,4)]=refraction(ix,iy,iz,nx,ny,nz,ray_number,n,x);

%ray then exits object

dir=1;
n=n2/n1;
Q1(:,1)=x(:,6); Q1(:,2)=y(:,6); Q1(:,3)=z(:,6);
Q2(:,1)=x(:,6)+tx(:,4); Q2(:,2)=y(:,6)+ty(:,4); Q2(:,3)=z(:,6)+tz(:,4);
%set points to find intercept
[x(:,7),y(:,7),z(:,7),nx,ny,nz]= surfaceintercept(F,N,Q1,Q2,V,ray_number,dir);%find
intercept
ix=(x(:,7)-x(:,6)); iy=(y(:,7)-y(:,6)); iz=(z(:,7)-z(:,6));
l=sqrt(ix.^2+iy.^2+iz.^2);
ix=ix./l; iy=iy./l; iz=iz./l; % find unit vector
nx=-nx;
%use Snell's law to find refraction
[tx(:,5),ty(:,5),tz(:,5)]=refraction(ix,iy,iz,nx,ny,nz,ray_number,n,x);

% find where returning rays hit cut-off

for i=1:ray_number
    for j=1:ray_number
        if ~isnan(x(i,j,1))
            P0=[0,0,0];
            I0=[x(i,j,7),y(i,j,7),z(i,j,7)];

```

```

l=[tx(i,j,5),ty(i,j,5),tz(i,j,5)];

d=(dot((P0-l0),[1,0,0]))/dot(l,[1,0,0]);
intersect=(d.*l)+l0;
x(i,j,8)=intersect(1);y(i,j,8)=intersect(2);z(i,j,8)=intersect(3);
end
end
end

% find what rays pass cut-off
% cut out round outline

for i=1:ray_number
for j=1:ray_number
if ~isnan(x(i,j,1))
P0=[-focal_length,0,0];
l0=[x(i,j,7),y(i,j,7),z(i,j,7)];
l=[tx(i,j,5),ty(i,j,5),tz(i,j,5)];

d=(dot((P0-l0),[1,0,0]))/dot(l,[1,0,0]);
intersect=(d.*l)+l0;
x(i,j,9)=intersect(1);y(i,j,9)=intersect(2);z(i,j,9)=intersect(3);
end
end
end

Y=-y(:,2);Z=-z(:,2);
for i=1:ray_number
for j=1:ray_number
if isnan(x(i,j,9))
if isnan(x(i,j,3))% rays that don't hit Schlieren object
y(i,j,9)=Y(i,j);z(i,j,9)=Z(i,j);
end
end
end
end
end
% if the ray hits cut-off then ignore it
X=x(:,8);Y=y(:,8);Z=z(:,8);
ang=0:0.1:2*pi;
xv=r2*cos(ang)+cutxshift; yv=r2*sin(ang)+cutyshift;
in = inpolygon(Y,Z,xv,yv);
X(~in)= nan; Y(~in)= nan; Z(~in)= nan;
%also cut off anything outside mirror
ang=0:0.1:2*pi;
xv=mirror_radius*cos(ang);
yv=mirror_radius*sin(ang);
in = inpolygon(z,y,xv,yv);
x(~in)= nan;
y(~in)= nan;
z(~in)= nan;

for i=1:ray_number
for j=1:ray_number
if ~isnan(x(i,j,3))% only look at rays that hit object
if isnan(X(i,j))% if the ray hits cut-off
y(i,j,9)=nan;z(i,j,9)=nan;
end
end
end

```

```

end
end
end

figure(2);% plot the rays on the viewing screen
set(gcf,'units','points','position',[0,0,1000,1000])
plot(y(:,9),-z(:,9),'.','MarkerSize',2,'Color',[1,0,0]);
axis equal

figure(1)
surf((x(:,2)),(y(:,2)),(z(:,2)));
hold on
quiver3(x(:,1),y(:,1),z(:,1),(x(:,3)-x(:,1)),(y(:,3)-y(:,1)),(z(:,3)-z(:,1)),'+','AutoScale','off');
quiver3(x(:,7),y(:,7),z(:,7),(x(:,8)-x(:,7)),(y(:,8)-y(:,7)),(z(:,8)-z(:,7)),'+','AutoScale','off');
quiver3(x(:,8),y(:,8),z(:,8),(x(:,9)-x(:,8)),(y(:,9)-y(:,8)),(z(:,9)-z(:,8)),'+','AutoScale','off');

function [F, V, N] = getstl()% function to retrieve STL file
f = fopen('star.stl', 'r'); % change stl file here

n=1;
v=1;
scale=2;
xshift=2800;
yshift=-50;
zshift=-50;
faces=1;
while (1)
    new_line = fgetl(f);
    %if string contains normal
    k=strfind(new_line,'normal');
    if ~isempty(k);
        [x y z] = strread(new_line, '%*s %*s %f %f %f');% get normals
        N(n,:)=x,y,z;
        n=n+1;
    end
    k=strfind(new_line,'vertex');% get vertex
    if ~isempty(k);
        j=1;
        while j<=3
            [x y z] = strread(new_line, '%*s %f %f %f');
            new_line = fgetl(f);
            V(v,:)=x,y,z;
            v=v+1;
            j=j+1;
        end
        F(faces,:) = [ v-3 v-2 v-1];
        faces=faces+1;
    end
    if (feof(f) == 1)
        break
    end

end
V=V.*scale;
V(:,1)=V(:,1)+xshift;
V(:,2)=V(:,2)+yshift;

```

```

    V(:,3)=V(:,3)+zshift;
fclose(f);
hold on
patch('Faces',F,'Vertices',V,'FaceColor','red','facealpha',.1)% plot stl file
axis equal

end
function [X,Y,Z,NX,NY,NZ] = surfaceintersect(F,N,Q1,Q2,V,raynum,dir,X)
% F is stl faces, V is stl verticys, N is stl normal Q1 and Q2 are ray
% start and end points raynum is number of rays, dir is direction the ray
% is heading (to sort what side the ray hits)

i=1;
j=1;
k=1;
n = 0;
hold on
axis equal
X=nan(raynum);Y=nan(raynum);Z=nan(raynum);
NX=nan(raynum);NY=nan(raynum);NZ=nan(raynum);
h = waitbar(0,'Finding surface intercepts');
for k=1:length(F)
p2p1=V(F(k,2,:))-V(F(k,1,:));
p3p2=V(F(k,3,:))-V(F(k,2,:));
p1p3=V(F(k,1,:))-V(F(k,3,:));
P1 = V(F(k,1,:)); P2 = V(F(k,2,:)); P3 = V(F(k,3,:)); % The triangle
for j=1:raynum
for i=1:raynum

    if ~isnan(Q1(i,j,1))%cuts down unneeded calculations
        P0 = [Q1(i,j,1) Q1(i,j,2) Q1(i,j,3)] + ((([P1-[Q1(i,j,1) Q1(i,j,2)
Q1(i,j,3)]])'*N(k,:)'))/((([Q2(i,j,1) Q2(i,j,2) Q2(i,j,3)]-[Q1(i,j,1) Q1(i,j,2)
Q1(i,j,3)]])'*N(k,:)))*([Q2(i,j,1) Q2(i,j,2) Q2(i,j,3)]-[Q1(i,j,1) Q1(i,j,2) Q1(i,j,3)]); % Get
intersection
        if ~isnan(P0)%cuts down unneeded calculations
            if ((cross(p1p3,(P0-P3))'*N(k,:))>=0 && ...% Is P0 is inside triangle?
                ((cross(p2p1,(P0-P1))'*N(k,:))>=0 && ...
                    ((cross(p3p2,(P0-P2))'*N(k,:))>=0
                n = n+1;
                if dir==1
                    if isnan(X(i,j))|| X(i,j)>=P0(1)%traveling into schlerin object
                        X(i,j)=P0(1); Y(i,j)=P0(2); Z(i,j)=P0(3);
                        NX(i,j)=N(k,1); NY(i,j)=N(k,2); NZ(i,j)=N(k,3);
                    end
                else
                    if isnan(X(i,j))|| X(i,j)<=P0(1)%traveling out of schlerin object
                        X(i,j)=P0(1); Y(i,j)=P0(2); Z(i,j)=P0(3);
                        NX(i,j)=N(k,1); NY(i,j)=N(k,2); NZ(i,j)=N(k,3);
                    end
                end

            end
        end
    end

end
end
end
if (round(k/1)==k/1)
waitbar(k/length(F),h);

```



```

end

end
close(h)
end
function [tx,ty,tz]=refraction(ix,iy,iz,nx,ny,nz,raynum,n,x)
tx=nan(raynum);ty=nan(raynum);tz=nan(raynum);
for i=1:raynum
    for j=1:raynum
        if ~isnan(x(i,j,3))
            Inc=[ix(i,j),iy(i,j),iz(i,j)];
            Nor=[nx(i,j),ny(i,j),nz(i,j)];
            if(((n.^2)*(1-(-dot(Nor,Inc).*-dot(Nor,Inc))))<=1
te=(n).*Inc+((((n).*-dot(Nor,Inc))-sqrt(1-((n).^2*(1-(-dot(Nor,Inc).*-dot(Nor,Inc)))))).*Nor);
            else
te=[nan,nan,nan]; %ignore internal reflection
            end
        end
    end
    tx(i,j)=te(1);ty(i,j)=te(2);tz(i,j)=te(3);
end
end
end
end
end

```

## MATLAB code to detect leak regions from video using a Regional neural network

```

clear
gpuDevice(1)% clear gpu memory
[RcnnFileName,RcnnPathName] = uigetfile('.mat','Select the RNCC');% prompt for selection of
network from file
rcnn=importdata(fullfile(RcnnPathName,RcnnFileName));% import network
[vidFileName,vidPathName] = uigetfile('.mp4','Select the input video');% prompt for input video
file
frameNumber = 0;
vr = VideoReader(fullfile(vidPathName,vidFileName));
vp = vision.VideoPlayer;
numdetects=10;
tic% start timer

while hasFrame(vr)
    frameNumber = frameNumber + 1;
    vFrame = readFrame(vr);
    %Detect Leak ROI
    [bbox, score, label] = detect(rcnn, vFrame);%detect roi
    [scores,idx] = sort(score,'descend');%sort the scores of the detects highest to lowest
    i=1;
    ii=1;
    while ii<=numdetects&&i<=length(idx)
        if ~isnan(idx)%checks to make sure there was a detect
            if length(idx)>=ii
                bboxes = bbox(idx(ii), :);
                annotation =sprintf('%s: (%f)', label(idx(ii)), scores(idx(ii)));%create detect annotation
                ii=ii+1;
            end
        end
        i=i+1;
    end
end

```

```

vFrame = insertObjectAnnotation(vFrame,'Rectangle',bboxes,annotation,'FontSize',40);%draw
detect annotation on frame
end

step(vp, vFrame); % step to next frame

end
time=toc;% stop timer
fps=frameNumber/time; % calculate frames per second

```

## MATLAB user interface for HDS

```

classdef knifeedge < matlab.apps.AppBase
    % Properties that correspond to app components
    properties (Access = public)
        UIFigure                                matlab.ui.Figure
        KnifestartpostionstepsSpinnerLabel      matlab.ui.control.Label
        KnifestartpostionstepsSpinner           matlab.ui.control.Spinner
        ChooseportcentertheknifeedgethemhitstarttotesthdrLabel
        matlab.ui.control.Label
        HSRTestLabel                            matlab.ui.control.Label
        ArduinoconnectionPanel                  matlab.ui.container.Panel
        PortLabel                               matlab.ui.control.Label
        PortList                               matlab.ui.control.DropDown
        connecttoArduinoButton                  matlab.ui.control.Button
        RefreshPortsButton                      matlab.ui.control.Button
        CamerasetupPanel                        matlab.ui.container.Panel
        imagesSpinnerLabel                      matlab.ui.control.Label
        imagesSpinner                           matlab.ui.control.Spinner
        cameratestButton                        matlab.ui.control.Button
        DelaysSpinnerLabel                      matlab.ui.control.Label
        DelaysSpinner                           matlab.ui.control.Spinner
        stepsperimageLabel                      matlab.ui.control.Label
        stepsperimageSpinner                    matlab.ui.control.Spinner
        TurntableSetupPanel                     matlab.ui.container.Panel
        StepsSpinnerLabel                       matlab.ui.control.Label
        StepsSpinner                            matlab.ui.control.Spinner
        TotalAngleRangeSpinnerLabel              matlab.ui.control.Label
        TotalAngleRangeSpinner                  matlab.ui.control.Spinner
        TurntablepostionstepsSpinnerLabel       matlab.ui.control.Label
        TurntablepostionstepsSpinner             matlab.ui.control.Spinner
        TurntablepostiondegEditFieldLabel       matlab.ui.control.Label
        TurntablepostiondegEditField             matlab.ui.control.NumericEditField
        startButton                             matlab.ui.control.Button
    end
    properties (Access = public)
        klocation=0;
        tlocation=0;
        a=0;
        shield;
        turntableangle=0;
        turntableanglesteps=0;
        turntablemove=0;
        sm;
        sm2;
    end
end

```

```

        s;
        ksteps2go;
        tsteps2go;
        photosnum=1 % number of photos taken
        tutablestep=1
        Knifestartpostion;
    end

    methods (Access = public)

        function startup(app)
            p = instrhwinfo('serial');
            app.PortList.Items = p.AvailableSerialPorts;
        end

    end
    methods (Access = private)
        % Button pushed function: startButton
        function hdr(app, event)

app.KnifestartpostionstepsSpinner.Value-
((app.imagesSpinner.Value*app.stepsperimageSpinner.Value)/2);

app.KnifestartpostionstepsSpinner.Value=app.Knifestartpostion;
    %Start taking photos
    app.photosnum=1;
    while app.tutablemove<=app.StepsSpinner.Value
        app.photosnum=1;

app.KnifestartpostionstepsSpinner.Value=app.Knifestartpostion;
    while app.photosnum<=app.imagesSpinner.Value
        knifesteps(app,event)
        shutter(app,event)
        pause(app.DelaysSpinner.Value)

app.KnifestartpostionstepsSpinner.Value=app.KnifestartpostionstepsSpinner
.Value+app.stepsperimageSpinner.Value;
        app.photosnum=app.photosnum+1;
    end
    %move turntable

app.turntableangle=app.TotalAngleRangeSpinner.Value/app.StepsSpinner.Valu
e;
        app.turntableanglesteps=ceil(app.turntableangle*(7/1.8));

app.TurntablepostionstepsSpinner.Value=app.TurntablepostionstepsSpinner.V
alue+app.turntableanglesteps;

app.TurntablepostiondegEditField.Value=app.TurntablepostionstepsSpinner.V
alue/(7/1.8);
        turntablesteps(app, event)
        app.tutablemove=app.tutablemove+1;
    end
end
    % Value changed function: KnifestartpostionstepsSpinner

```

```

function knifesteps(app, event)
    app.ksteps2go=(app.KnifestartpostionstepsSpinner.Value-
app.klocation);
    while app.ksteps2go~=0
        if app.ksteps2go>0
            move(app.sm, 1);
            app.klocation=app.klocation+1;
        end
        if app.ksteps2go<0
            move(app.sm, -1);
            app.klocation=app.klocation-1;
        end
        app.ksteps2go=(app.KnifestartpostionstepsSpinner.Value-
app.klocation);
    end

end
% Button pushed function: RefreshPortsButton
function portcheck(app, event)
    p = instrhwinfo('serial');
    app.PortList.Items = p.AvailableSerialPorts;
end
% Button pushed function: cameratestButton
function shutter(app, event)
    writePosition(app.s, .5);
    writePosition(app.s, 0);
    pause(app.DelaysSpinner.Value)
    writePosition(app.s, .5);
end
% Button pushed function: connecttoArduinoButton
function start(app, event)
    if app.a==0
        app.a=arduino(app.PortList.Value, 'Mega2560', 'Libraries',
'Adafruit\MotorShieldV2');
        app.tlocation=0;
        app.klocation=0;
        app.shield=addon(app.a, 'Adafruit\MotorShieldV2'); % Description
        app.sm=stepper(app.shield,2,20,'stepType','Microstep'); %
Description
        app.sm2=stepper(app.shield,1,20,'stepType','Microstep'); %
Description
        %         app.s = servo(app.shield, 1);
        app.s = servo(app.shield,1, 'MinPulseDuration', 900*10^-6,
'MaxPulseDuration', 1000*10^-6)
        app.sm.RPM = 100;
        app.sm2.RPM = 300;
        shutter(app,event)
    end
end
% Value changed function: TurntablepostionstepsSpinner
function turntablesteps(app, event)

app.tsteps2go=(app.TurntablepostionstepsSpinner.Value-app.tlocation);
    while app.tsteps2go~=0
        if app.tsteps2go>0

```

```

        move(app.sm2, 1);
        app.tlocation=app.tlocation+1;
    end
    if app.tsteps2go<0
        move(app.sm2, -1);
        app.tlocation=app.tlocation-1;
    end

app.tsteps2go=(app.TurntablepostionstepsSpinner.Value-app.tlocation);

app.TurntablepostiondegEditField.Value=app.TurntablepostionstepsSpinner.V
alue/(7/1.8);

end

%
end
end
% App initialization and construction
methods (Access = private)
    % Create UIFigure and components
    function createComponents(app)
        % Create UIFigure
        app.UIFigure = uifigure;
        app.UIFigure.Position = [100 100 348 660];
        app.UIFigure.Name = 'UI Figure';
        % Create KnifestartpostionstepsSpinnerLabel
        app.KnifestartpostionstepsSpinnerLabel =
uilabel(app.UIFigure);
        app.KnifestartpostionstepsSpinnerLabel.HorizontalAlignment =
'right';
        app.KnifestartpostionstepsSpinnerLabel.VerticalAlignment =
'top';
        app.KnifestartpostionstepsSpinnerLabel.Position = [46 422 142
15];
        app.KnifestartpostionstepsSpinnerLabel.Text = 'Knife start
postion (steps)';
        % Create KnifestartpostionstepsSpinner
        app.KnifestartpostionstepsSpinner = uispinner(app.UIFigure);
        app.KnifestartpostionstepsSpinner.Limits = [-50 50];
        app.KnifestartpostionstepsSpinner.ValueChangedFcn =
createCallbackFcn(app, @knifesteps, true);
        app.KnifestartpostionstepsSpinner.Position = [200 418 100
22];
        % Create
ChooseportcentertheknifeedgethemhitstartttotesthdrLabel
        app.ChooseportcentertheknifeedgethemhitstartttotesthdrLabel =
uilabel(app.UIFigure);

app.ChooseportcentertheknifeedgethemhitstartttotesthdrLabel.VerticalAlignm
ent = 'top';

app.ChooseportcentertheknifeedgethemhitstartttotesthdrLabel.Position = [20
577 328 15];

```

```

app.ChooseportcentertheknifeedgethemhitstarttotesthdrLabel.Text = 'Choose
port, center the knife edge them hit start to test hdr ';
    % Create HSRTTestLabel
    app.HSRTTestLabel = uilabel(app.UIFigure);
    app.HSRTTestLabel.VerticalAlignment = 'top';
    app.HSRTTestLabel.FontSize = 20;
    app.HSRTTestLabel.Position = [127 610 90 26];
    app.HSRTTestLabel.Text = 'HSR Test';
    % Create ArduinoconnectionPanel
    app.ArduinoconnectionPanel = uipanel(app.UIFigure);
    app.ArduinoconnectionPanel.Title = 'Arduino connection';
    app.ArduinoconnectionPanel.Position = [43 456 260 100];
    % Create PortLabel
    app.PortLabel = uilabel(app.ArduinoconnectionPanel);
    app.PortLabel.HorizontalAlignment = 'right';
    app.PortLabel.VerticalAlignment = 'top';
    app.PortLabel.Position = [16 33 27 15];
    app.PortLabel.Text = 'Port';
    % Create PortList
    app.PortList = uidropdown(app.ArduinoconnectionPanel);
    app.PortList.Items = (Peale & Summers, 1996);
    app.PortList.Position = [58 29 65 22];
    app.PortList.Value = (Peale & Summers, 1996);
    % Create connecttoArduinoButton
    app.connecttoArduinoButton =
uibutton(app.ArduinoconnectionPanel, 'push');
    app.connecttoArduinoButton.ButtonPushedFcn =
createCallbackFcn(app, @start, true);
    app.connecttoArduinoButton.Position = [132.5 50 117 22];
    app.connecttoArduinoButton.Text = 'connect to Arduino';
    % Create RefreshPortsButton
    app.RefreshPortsButton = uibutton(app.ArduinoconnectionPanel,
'push');
    app.RefreshPortsButton.ButtonPushedFcn =
createCallbackFcn(app, @portcheck, true);
    app.RefreshPortsButton.Position = [133 12 117 22];
    app.RefreshPortsButton.Text = 'Refresh Ports';
    % Create CamerasetupPanel
    app.CamerasetupPanel = uipanel(app.UIFigure);
    app.CamerasetupPanel.Title = 'Camera setup';
    app.CamerasetupPanel.Position = [40 269 266 133];
    % Create imagesSpinnerLabel
    app.imagesSpinnerLabel = uilabel(app.CamerasetupPanel);
    app.imagesSpinnerLabel.HorizontalAlignment = 'right';
    app.imagesSpinnerLabel.VerticalAlignment = 'top';
    app.imagesSpinnerLabel.Position = [17 84 48 15];
    app.imagesSpinnerLabel.Text = 'images ';
    % Create imagesSpinner
    app.imagesSpinner = uispinner(app.CamerasetupPanel);
    app.imagesSpinner.Limits = [0 100];
    app.imagesSpinner.Position = [71 80 44 22];
    app.imagesSpinner.Value = 10;
    % Create cameratestButton

```

```

        app.cameratestButton = uibutton(app.CamerasetupPanel,
'push');
        app.cameratestButton.ButtonPushedFcn = createCallbackFcn(app,
@shutter, true);
        app.cameratestButton.Position = [82 15 117 22];
        app.cameratestButton.Text = 'camera test';
        % Create DelaysSpinnerLabel
        app.DelaysSpinnerLabel = uilabel(app.CamerasetupPanel);
        app.DelaysSpinnerLabel.HorizontalAlignment = 'right';
        app.DelaysSpinnerLabel.VerticalAlignment = 'top';
        app.DelaysSpinnerLabel.Position = [142 84 51 15];
        app.DelaysSpinnerLabel.Text = 'Delay(s)';
        % Create DelaysSpinner
        app.DelaysSpinner = uispinner(app.CamerasetupPanel);
        app.DelaysSpinner.Limits = [0.01 30];
        app.DelaysSpinner.Position = [198 80 61 22];
        app.DelaysSpinner.Value = 1;
        % Create stepsperimageLabel
        app.stepsperimageLabel = uilabel(app.CamerasetupPanel);
        app.stepsperimageLabel.HorizontalAlignment = 'right';
        app.stepsperimageLabel.VerticalAlignment = 'top';
        app.stepsperimageLabel.Position = [57 55 92 15];
        app.stepsperimageLabel.Text = 'steps per image';
        % Create stepsperimageSpinner
        app.stepsperimageSpinner = uispinner(app.CamerasetupPanel);
        app.stepsperimageSpinner.Limits = [1 10];
        app.stepsperimageSpinner.Position = [155 51 44 22];
        app.stepsperimageSpinner.Value = 1;
        % Create TurntableSetupPanel
        app.TurntableSetupPanel = uipanel(app.UIFigure);
        app.TurntableSetupPanel.Title = 'Turntable Setup';
        app.TurntableSetupPanel.Position = [40 82 266 169];
        % Create StepsSpinnerLabel
        app.StepsSpinnerLabel = uilabel(app.TurntableSetupPanel);
        app.StepsSpinnerLabel.HorizontalAlignment = 'right';
        app.StepsSpinnerLabel.VerticalAlignment = 'top';
        app.StepsSpinnerLabel.Position = [87 120 36 15];
        app.StepsSpinnerLabel.Text = 'Steps';
        % Create StepsSpinner
        app.StepsSpinner = uispinner(app.TurntableSetupPanel);
        app.StepsSpinner.Limits = [0 100];
        app.StepsSpinner.Position = [129 116 44 22];
        app.StepsSpinner.Value = 10;
        % Create TotalAngleRangeSpinnerLabel
        app.TotalAngleRangeSpinnerLabel =
uilabel(app.TurntableSetupPanel);
        app.TotalAngleRangeSpinnerLabel.HorizontalAlignment =
'right';
        app.TotalAngleRangeSpinnerLabel.VerticalAlignment = 'top';
        app.TotalAngleRangeSpinnerLabel.Position = [47 88 106 15];
        app.TotalAngleRangeSpinnerLabel.Text = 'Total Angle Range';
        % Create TotalAngleRangeSpinner
        app.TotalAngleRangeSpinner =
uispinner(app.TurntableSetupPanel);
        app.TotalAngleRangeSpinner.Limits = [5 180];

```

```

        app.TotalAngleRangeSpinner.Position = [158 84 61 22];
        app.TotalAngleRangeSpinner.Value = 5;
        % Create TurntablepostionstepsSpinnerLabel
        app.TurntablepostionstepsSpinnerLabel =
uilabel(app.TurntableSetupPanel);
        app.TurntablepostionstepsSpinnerLabel.HorizontalAlignment =
'right';
        app.TurntablepostionstepsSpinnerLabel.VerticalAlignment =
'top';
        app.TurntablepostionstepsSpinnerLabel.Position = [3 59 140
15];
        app.TurntablepostionstepsSpinnerLabel.Text = 'Turntable
postion (steps)';
        % Create TurntablepostionstepsSpinner
        app.TurntablepostionstepsSpinner =
uispinner(app.TurntableSetupPanel);
        app.TurntablepostionstepsSpinner.Limits = [-5000 5000];
        app.TurntablepostionstepsSpinner.ValueChangedFcn =
createCallbackFcn(app, @turntablesteps, true);
        app.TurntablepostionstepsSpinner.Position = [155 55 100 22];
        % Create TurntablepostiondegEditFieldLabel
        app.TurntablepostiondegEditFieldLabel =
uilabel(app.TurntableSetupPanel);
        app.TurntablepostiondegEditFieldLabel.HorizontalAlignment =
'right';
        app.TurntablepostiondegEditFieldLabel.VerticalAlignment =
'top';
        app.TurntablepostiondegEditFieldLabel.Position = [8 21 132
15];
        app.TurntablepostiondegEditFieldLabel.Text = 'Turntable
postion (deg)';
        % Create TurntablepostiondegEditField
        app.TurntablepostiondegEditField =
uieditfield(app.TurntableSetupPanel, 'numeric');
        app.TurntablepostiondegEditField.Editable = 'off';
        app.TurntablepostiondegEditField.Position = [155 17 100 22];
        % Create startButton
        app.startButton = uibutton(app.UIFigure, 'push');
        app.startButton.ButtonPushedFcn = createCallbackFcn(app,
@hdr, true);
        app.startButton.Position = [192 43 117 22];
        app.startButton.Text = 'start';
    end
end
methods (Access = public)
    % Construct app
    function app = knifeedge
        % Create and configure components
        createComponents(app)
        % Register the app with App Designer
        registerApp(app, app.UIFigure)
        if nargin == 0
            clear app
        end
    end
end

```



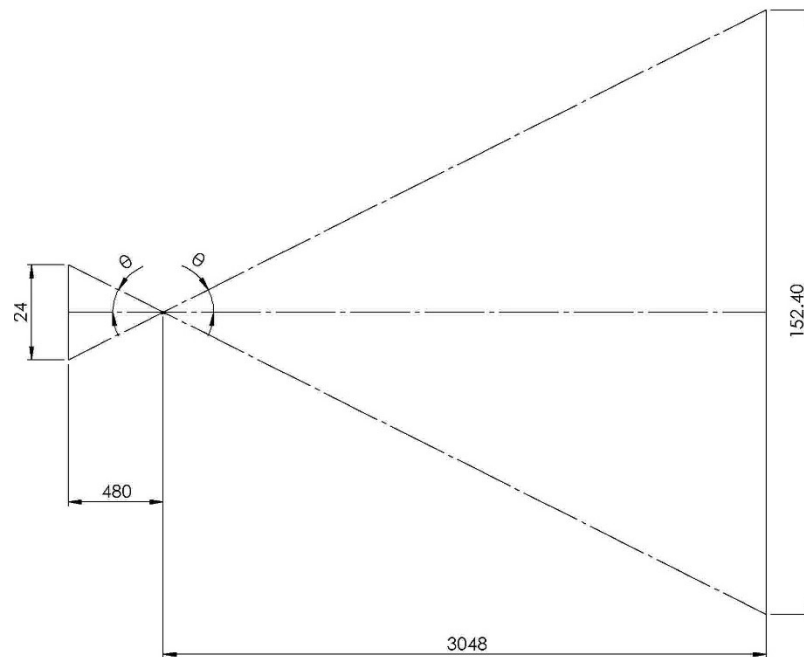
```
% Code that executes before app deletion
function delete(app)
    % Delete UIFigure when app is deleted
    delete(app.UIFigure)
end
end
end
```

## Appendix B

### Lens focal length

$$\tan^{-1} \frac{152.49}{3048} = \tan^{-1} \frac{24}{x} = 2.86 \text{ degrees}$$

$$x = 24 \times \frac{3048}{152.4} = 480 \text{ mm}$$

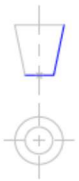
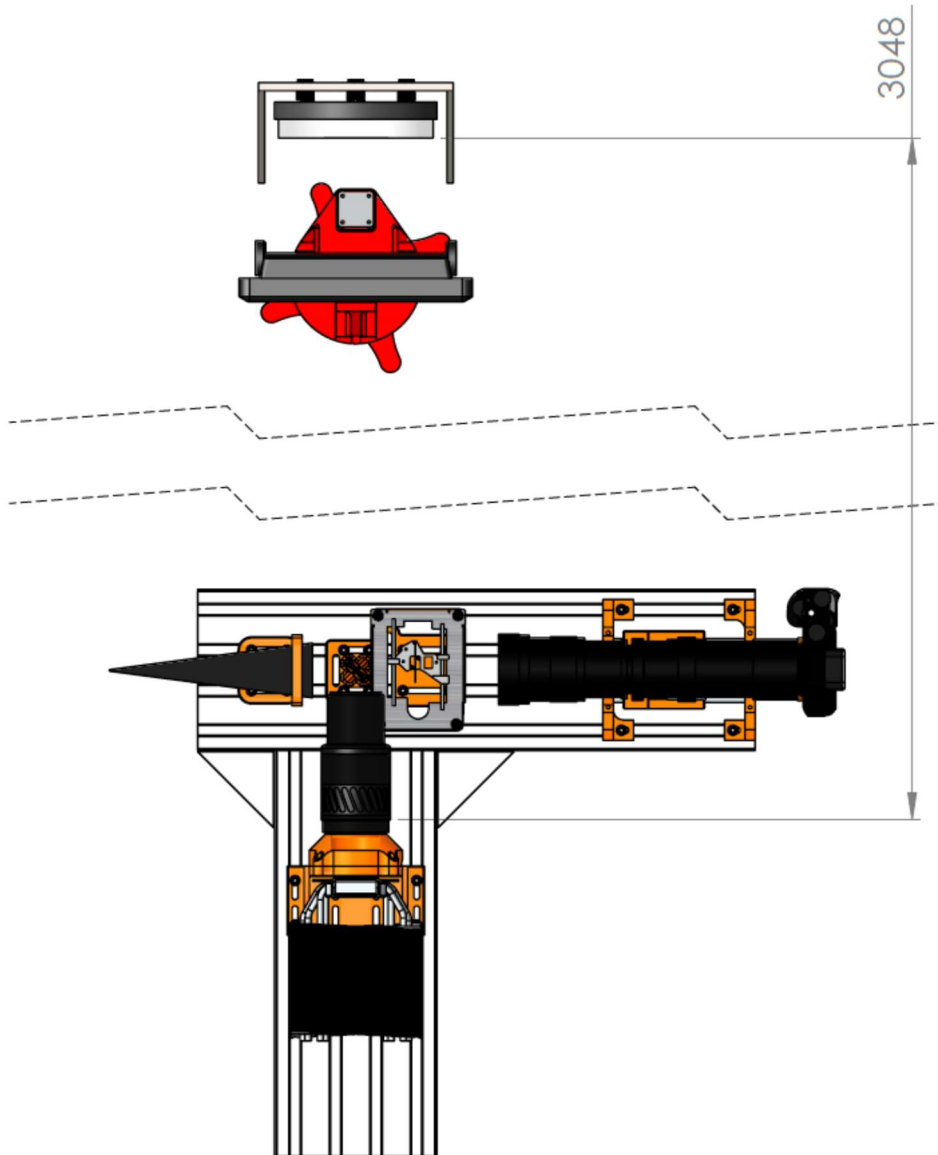


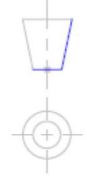
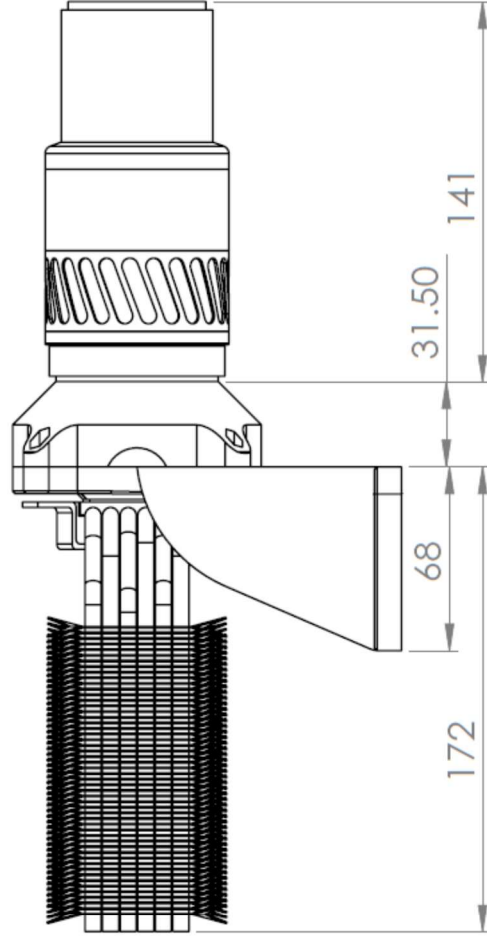
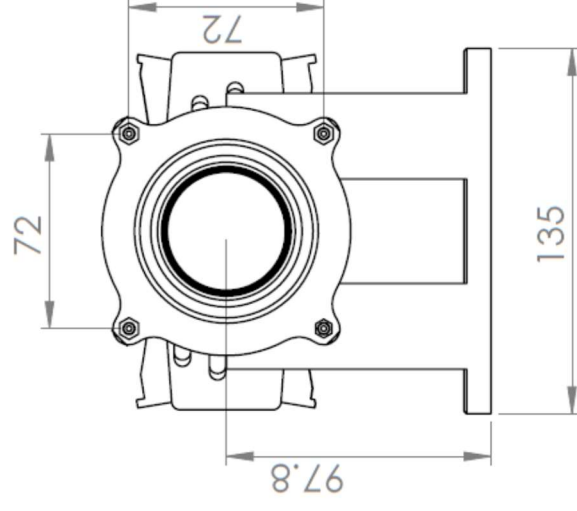
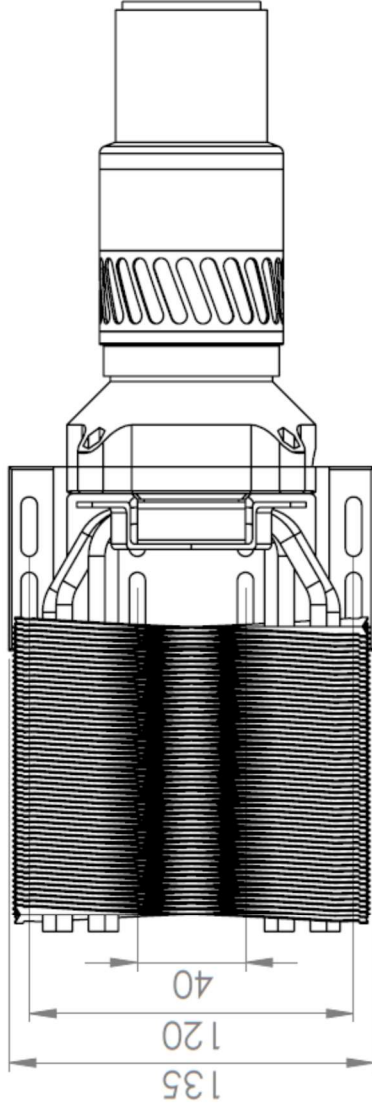
### Crop sensor full frame equivalent focal length

$$0.71 \times 1.6 \times 200 = 227 \text{ mm}$$

## Appendix C

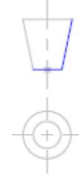
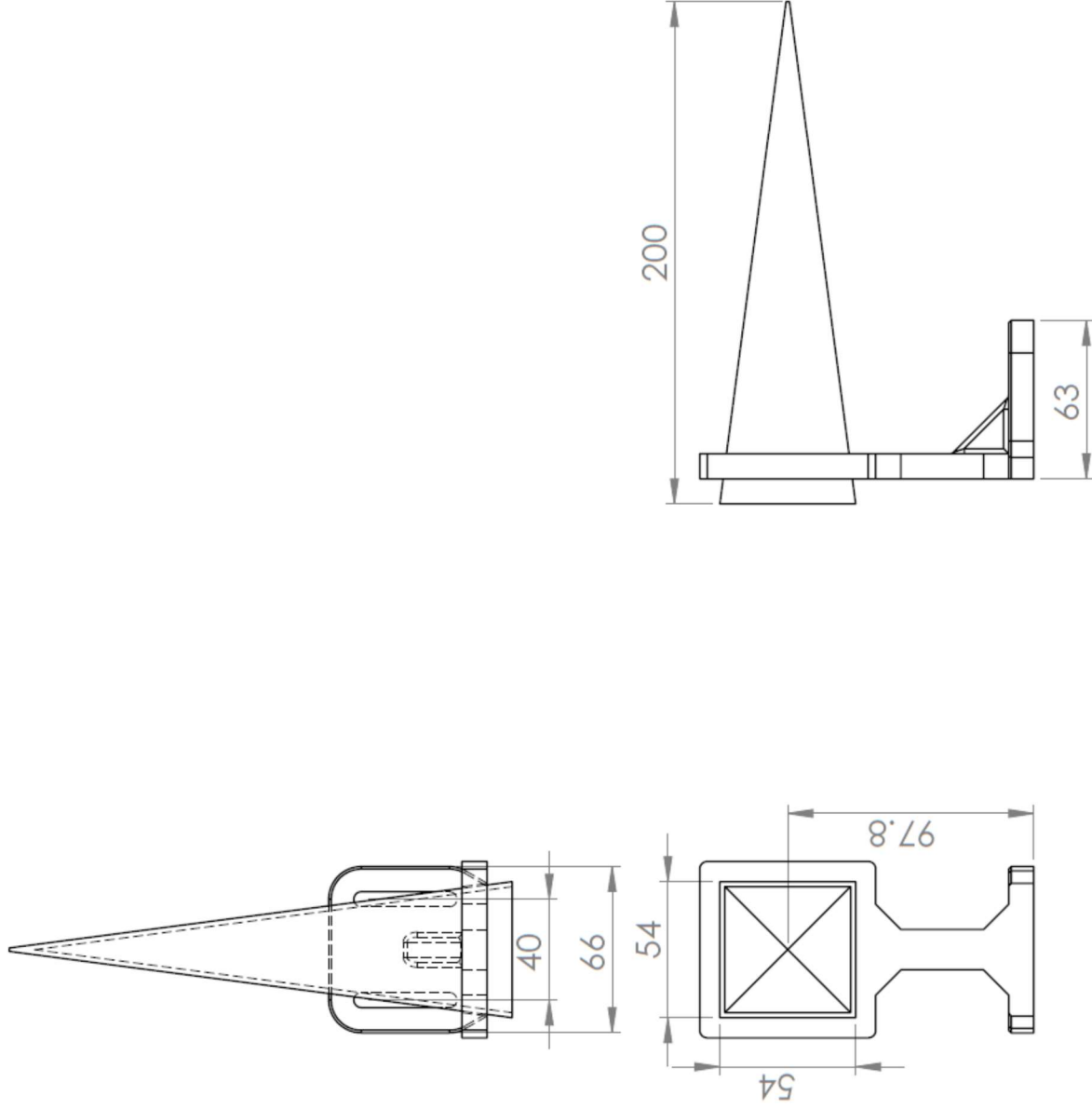
### Optical assembly drawings

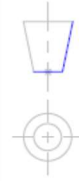
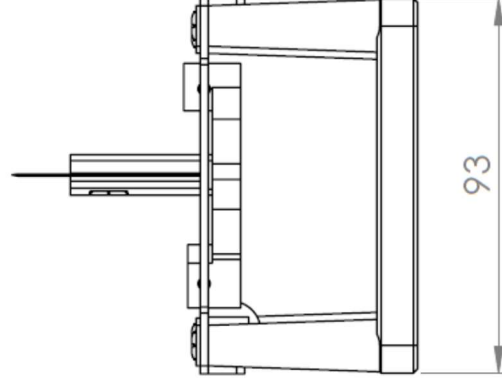
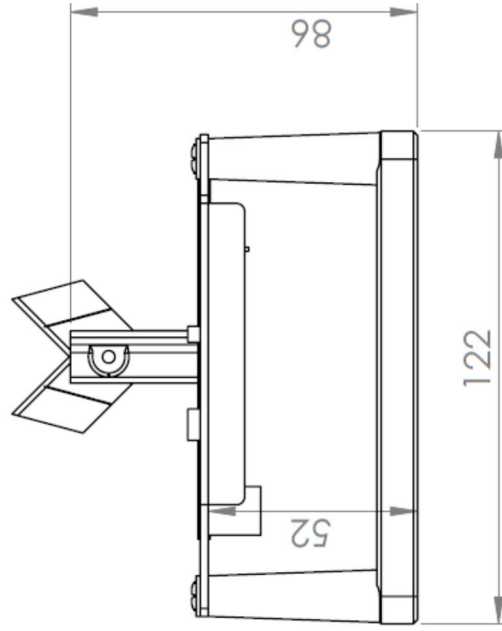
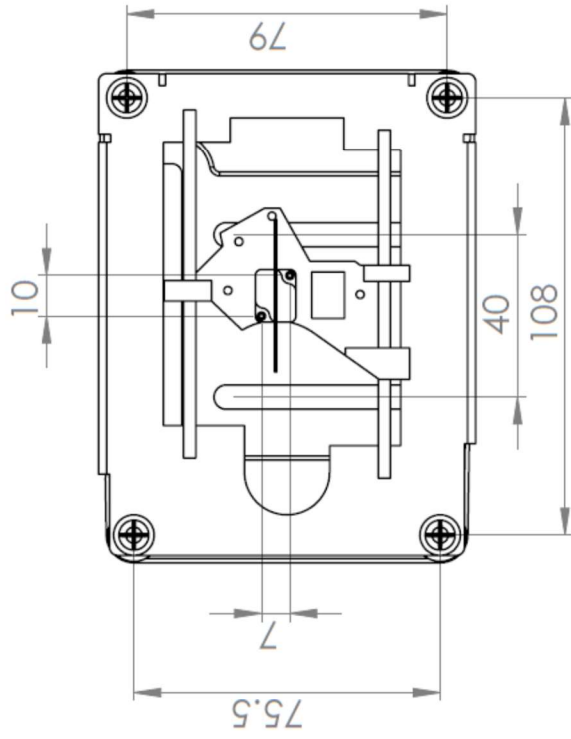




Drawn: Tony Mackenzie  
 Title: Light Source Assembly  
 Date: 8/5/2018

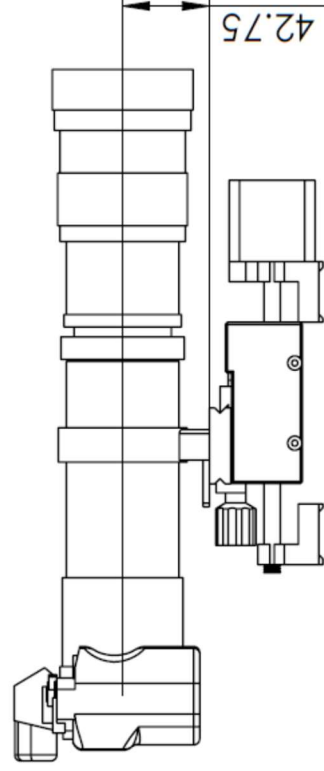
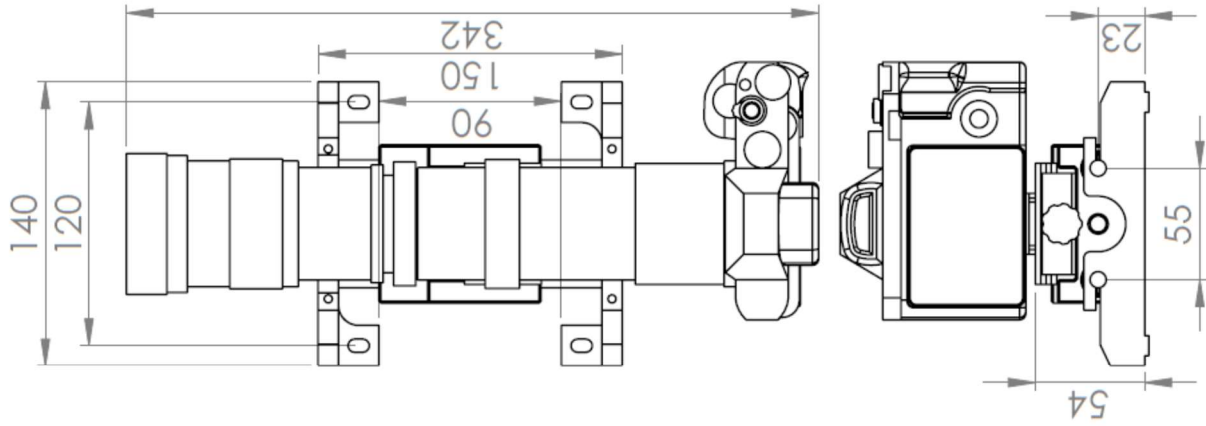
SCALE 1:3

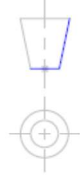
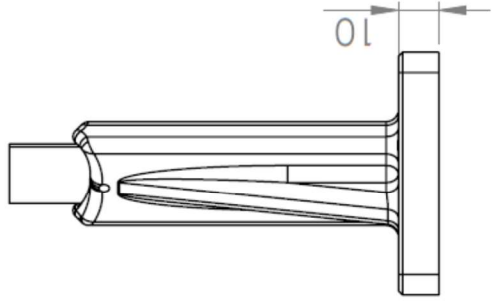
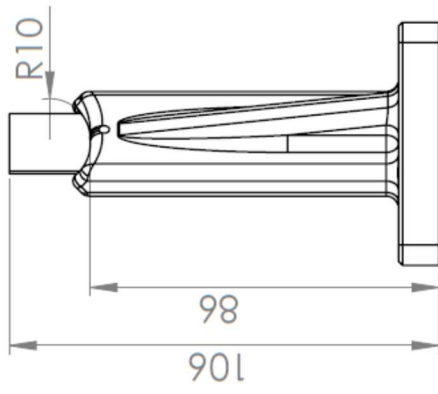
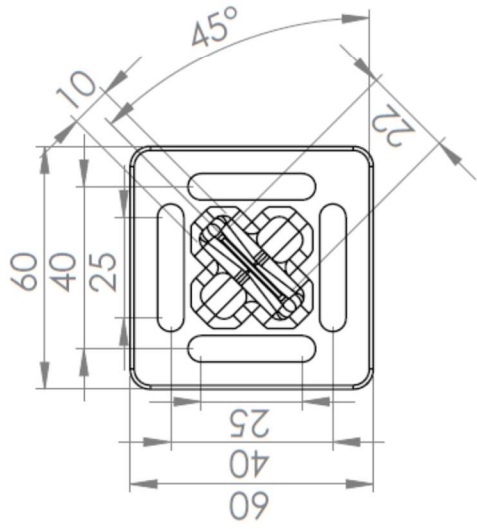




Drawn: Tony Mackenzie  
Title: Knife Edge Assembly  
Date: 17/5/2018

SCALE 1:2

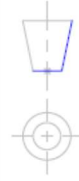
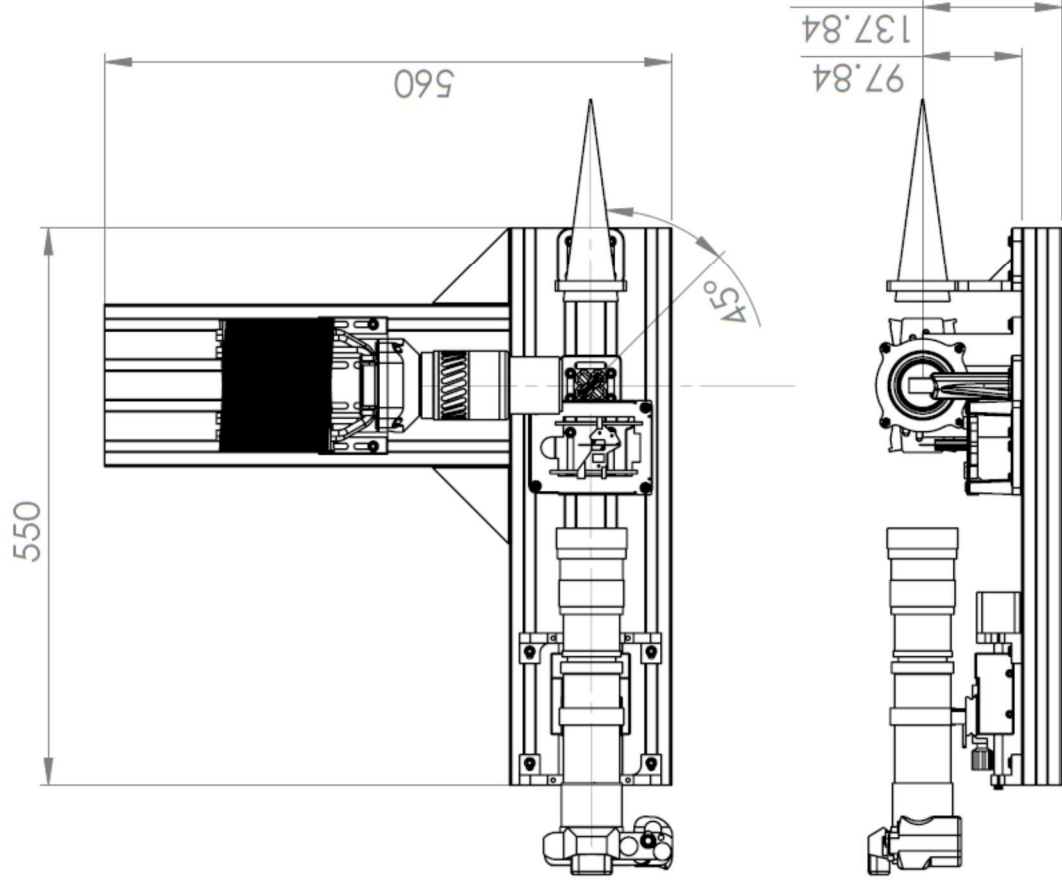




Drawn: Tony Mackenzie  
Title: Beam Splitter  
Date: 8/5/2018

SCALE 1:2





Drawn: Tony Mackenzie  
 Title: Optical Assembly  
 Date: 8/5/2018

SCALE 1:8

## Appendix D

### Images



Full frame uncropped image from Sony 70-200mm



Image of leak 4 using the Canon 70-200 in APSC mode for a FF equivalent focal length of 227mm

## 11 References

- Adobe Systems Incorporated. (2005). What's New in Adobe Photoshop CS2. Retrieved from <https://www.adobe.com/aboutadobe/pressroom/pressmaterials/creativesuite2/pdfs/ps/PSCS2-WN.pdf>
- Avinash Nehemiah, A. J. (2017). *Deep Learning for Automated Driving with MATLAB*. Retrieved 17/1/2018, from <https://devblogs.nvidia.com/parallelforall/deep-learning-automated-driving-matlab/>
- B & H Foto & Electronics Corp. (2017). *Sony Alpha a7R II Mirrorless Digital Camera*. Retrieved from [https://www.bhphotovideo.com/c/product/1159878-REG/sony\\_a7r\\_mark\\_ii\\_digital.html](https://www.bhphotovideo.com/c/product/1159878-REG/sony_a7r_mark_ii_digital.html)
- Bachalo, W. D., & Houser, M. J. (1985). Optical interferometry in fluid dynamics research. *Optical Engineering*, 24(3), 455-450.
- Beeson, S., & Mayer, J. W. (2007). *Patterns of Light*: Springer Science & Business Media.
- Ben-Dor, G., Igra, O., & Elperin, T. (2001). *Handbook of Shock Waves*: Academic Press.
- Block Engineering. (2017). *FTIR and Michelson Interferometer Technology Overview*. Retrieved 4/4/2017, 2017, from <http://blockeng.com/technology/ftirtechnology.html>
- Chen, C. S., & Bird III, J. D. (1971). Alignment technique for the Mach-Zehnder interferometer using a laser. *Journal of Physics E: Scientific Instruments*, 157-158.
- Chevalerias, R., Latron, Y., & Veret, C. (1957). Methods of Interferometry Applied to the Visualization of Flows in Wind Tunnels. *Journal of the Optical Society of America*, Vol. 47, 703-706.
- Ciupa, R., & Rogalski, A. (1997). Performance limitations of photon and thermal infrared detectors. *OPTOELECTRONICS REVIEW*, 257-266.
- D. Holland, S., Roberts, R., Chimenti, D. E., & Strei, M. (2005). *Two-sensor ultrasonic spacecraft leak detection using structure-borne noise* (Vol. 6). <https://doi.org/10.1121/1.1855351>
- E Peale, R., & L Summers, P. (1996). *Zebra schlieren optics for leak detection* (Vol. 35). <https://doi.org/10.1364/AO.35.004518>
- Edmund Optics. (2017a). *36" Length, Dovetail Optical Rail* Retrieved 2017, from <https://www.edmundoptics.com/optomechanics/translation-stages-slides/manual-stages-slides/36quot-length-dovetail-optical-rail/>
- Edmund Optics. (2017b). *500mm x 500mm, Breadboard* Retrieved 2017, from <https://www.edmundoptics.com/optomechanics/optical-tables-breadboards/bench-plates/500mm-x-500mm-breadboard/#specs>
- Edmund Optics. (2018). *10" Dia, 100" FL Enhanced Alum., Spherical Mirror*. Retrieved from <https://www.edmundoptics.com/optics/optical-mirrors/focusing-concave-mirrors/10quot-dia-100quot-fl-enhanced-alum.-spherical-mirror/>
- Fei-Fei, L. D., J. Dong, W. Socher, R. Li, L.-J. Li, K. . (2009). *ImageNet: A Large-Scale Hierarchical Image Database*. presented at the meeting of the 009 IEEE Conference on Computer Vision and Pattern Recognition, Miami, FL.
- FLIR Systems Inc. (2015). GSA Price List. Retrieved from [https://www.gsaadvantage.gov/ref\\_text/GS03F5051C/00OHR8.37ALTA\\_GS-03F-5051C\\_GSAPRICELISTMODPS0186.PDF](https://www.gsaadvantage.gov/ref_text/GS03F5051C/00OHR8.37ALTA_GS-03F-5051C_GSAPRICELISTMODPS0186.PDF)
- FLIR®. (2017). Gas Detection : The Professional Guide. *FLIR Gas Detection Systems*. Retrieved from <http://www.flir.com/ogi/display/?id=67179>
- Girshick, R. B. (2015). Fast R-CNN. *CoRR*, abs/1504.08083.
- Glorot, X., Bordes, A., & Bengio, Y. (2011). *Deep Sparse Rectifier Neural Networks* (Vol. 15)
- Gordon, I. E., Rothman, L. S., Hill, C., Kochanov, R. V., Tan, Y., Bernath, P. F., . . . Zak, E. J. (2017). *The HITRAN2016 Molecular Spectroscopic Database*. Retrieved from <http://www.osti.gov/scitech/servlets/purl/1368409>
- Hariharan, P. (2007). *Basics of INTERFEROMETRY*: Elsevier Inc.

- Hooke, R. (1665). *Micrographia*. Retrieved from <http://roslistonastronomy.uk/wp-content/uploads/2017/01/Project-Gutenberg-Robert-Hooke-Micrographia-accessed-240117.pdf>
- HU, Y. Y. H. (2017, 30/01/18). Loss Functions In Deep Learning [Summary of some loss functions that are used in training a neural network.]. Retrieved from <http://yeephycho.github.io/2017/09/16/Loss-Functions-In-Deep-Learning/>
- Industrial Monitoring and Control Pty Ltd. (2017, 20/4/2017). *Fixed Gas Cameras*. Retrieved from [https://www.imc-store.com.au/category\\_s/1962.htm](https://www.imc-store.com.au/category_s/1962.htm)
- Krehl, p., & Engemann, s. (1995). August Toepler- the first who visualized shock waves. *Shock Waves* 5, 1-18.
- Krehl, P. O. K. (2009). *History of Shock Waves, Explosions and Impact*: Springer-Verlag Berlin Heidelberg.
- Krizhevsky, A., Sutskever, I., & E. Hinton, G. (2012). *ImageNet Classification with Deep Convolutional Neural Networks* (Vol. 25). <https://doi.org/10.1145/3065386>
- Lecun, Y., & Bengio, Y. (1995). *Convolutional Networks for Images, Speech, and Time-Series*
- Levoy, M. (2014, 27/8/14). HDR+: Low Light and High Dynamic Range photography in the Google Camera App. Retrieved from <https://research.googleblog.com/2014/10/hdr-low-light-and-high-dynamic-range.html>
- Lindsay, S. M., Anderson, M. W., & Sandercock, J. R. (1981). Construction and alignment of a high performance multipass vernier tandem Fabry Perot interferometer. *Review of Scientific Instruments* 52.
- Luminus Devices Inc. (2016). CBT-120. Retrieved from [http://www.luminus.com/products/Luminus\\_CBT120\\_Datasheet.pdf](http://www.luminus.com/products/Luminus_CBT120_Datasheet.pdf)
- Mann, S. (1998). Method and apparatus for producing digital images having extended dynamic ranges: Google Patents.
- MathWorks (2017). *Object Detection Using Deep Learning*. Retrieved 15/1/2018, 2017, from <https://au.mathworks.com/help/vision/examples/object-detection-using-deep-learning.html#d119e1036>
- Mathworks. (2018a). *Pretrained Convolutional Neural Networks*. Retrieved 21/02/18, 2018, from [https://au.mathworks.com/help/nnet/ug/pretrained-convolutional-neural-networks.html?searchHighlight=pretrained&s\\_tid=doc\\_srchtile](https://au.mathworks.com/help/nnet/ug/pretrained-convolutional-neural-networks.html?searchHighlight=pretrained&s_tid=doc_srchtile)
- Mathworks. (2018b). *Specify Layers of Convolutional Neural Network*. Retrieved 13/02/18, 2018, from [https://au.mathworks.com/help/nnet/ug/layers-of-a-convolutional-neural-network.html?searchHighlight=stride%20network&s\\_tid=doc\\_srchtile#mw\\_a8ef6ff0-eeab-4af3-9b2a-092908284ee8](https://au.mathworks.com/help/nnet/ug/layers-of-a-convolutional-neural-network.html?searchHighlight=stride%20network&s_tid=doc_srchtile#mw_a8ef6ff0-eeab-4af3-9b2a-092908284ee8)
- MathWorks. (2018c). *trainingOptions*. Retrieved 30/1/2018, 2018, from <https://au.mathworks.com/help/nnet/ref/trainingoptions.html#bu812m0>
- Moon, C., C. Brown, W., Mellen, S., & Lovelace, D. (2008). *Ultrasound Techniques for Leak Detection in Vehicle and Pressure Vessel Production Lines* (Vol. 3)
- Naval Air Warfare Center Weapons Division. (2013). *Electronic Warfare and Radar Systems Engineering Handbook*. Retrieved from <http://www.navair.navy.mil/nawcwg/ewssa/downloads/NAWCWD%20TP%208347.pdf>
- Newport. (2017a). *9732 Low-cost Optical Rails*. Retrieved 2017, from <https://www.newport.com/p/9732>
- Newport. (2017b). *Solid Aluminum Optical Breadboard, 600 x 600 mm, 25 mm M6 Grid*. Retrieved 2017, from <https://www.newport.com/p/M-SA2-22>
- Opgal. (2017). *Gas Leak Detection Cameras*. Retrieved 19/4/2017, 2017, from <https://www.opgal.com/gas-leak-detection-cameras/>

- Oren, D. C., Durrett, R. P., & Ferguson, C. R. (1988). Bullseye color schlieren flow visualization. *Experiments in Fluids*, 357-364.
- Peale, R. E., & Summers, P. L. (1996). Zebra schlieren optics for leak detection. *Applied Optics*, 35(22), 4518-4521. <https://doi.org/10.1364/AO.35.004518>
- Ren, S., He, K., Girshick, R. B., & Sun, J. (2015). Faster R-CNN: Towards Real-Time Object Detection with Region Proposal Networks. *CoRR*, abs/1506.01497.
- Rheinberg, J. H. (1896). On an Addition to the Methods of Microscopical Research, by a new way of Optically producing Colour-Contrast between an Object and its Background, or between Definite Parts of the Object itself. *Journal of the Royal Microscopical Society*, 373-388.
- Rogalski, A. (2002). Infrared detectors: an overview. *Infrared Physics & Technology*, 43(3-5), 1350-4495.
- Schardin, H. (1942). SCHLIEREN METHODS AND THEIR APPLICATIONS (N. T. R. Library, Trans.). In (Vol. N70-25586, pp. 303-439)
- Schlag, I. (2016). *IMPORTANT ILSVRC ACHIEVEMENTS FROM 2012-2015*. Retrieved 15/1/2018, from <http://ischlag.github.io/2016/04/05/important-ILSVRC-achievements/>
- Settles, G. S. (2001). *Schlieren and Shadowgraph Techniques - Visualizing Phenomena in Transparent Media*. New York: Springer-Verlag Berlin Heidelberg.
- Shawn, R., & Christiaan, G. (2017). Real-Time, In Situ Intelligent Video Analytics: Harnessing The Power of GPUs for Deep Learning Applications. *DSIAC Journal*, Volume 4(1), 35-42.
- Simonyan, K., & Zisserman, A. (2014). *Very Deep Convolutional Networks for Large-Scale Image Recognition*
- Smartt, R. N., & Steel, W. H. (1975). Theory and application of point-diffraction interferometers. *Japanese Journal of Applied Physics*, 14, 351.
- SONY New Zealand. (2017). *ilce 7body kit specifications*. Retrieved 4/12/17, 2017, from <http://www.sony.co.nz/electronics/interchangeable-lens-cameras/ilce-7-body-kit/specifications>
- Srivastava, A., Muralidhar, K., & Panigrahi, P. K. (2004). Comparison of interferometry, schlieren and shadowgraph for visualizing convection around a KDP crystal. *Journal of Crystal Growth*(267), 348-361.
- Ting, C.-C., & Chen, C.-C. (2013). Detection of gas leakage using microcolor schlieren technique. *Measurement* 46, 2467-2472.
- World Health Organization. (2003). Health aspects of air pollution with particulate matter, ozone and nitrogen dioxide: report on a WHO working group, Bonn, Germany 13-15 January 2003.
- World Health Organization. (2018). *UV radiation*. Retrieved from <http://www.who.int/uv/fag/whatisuv/en/index2.html>
- Zhang, J. (1996). Designing a cost-effective and reliable pipeline leak-detection system. *Pipes and Pipelines International*.